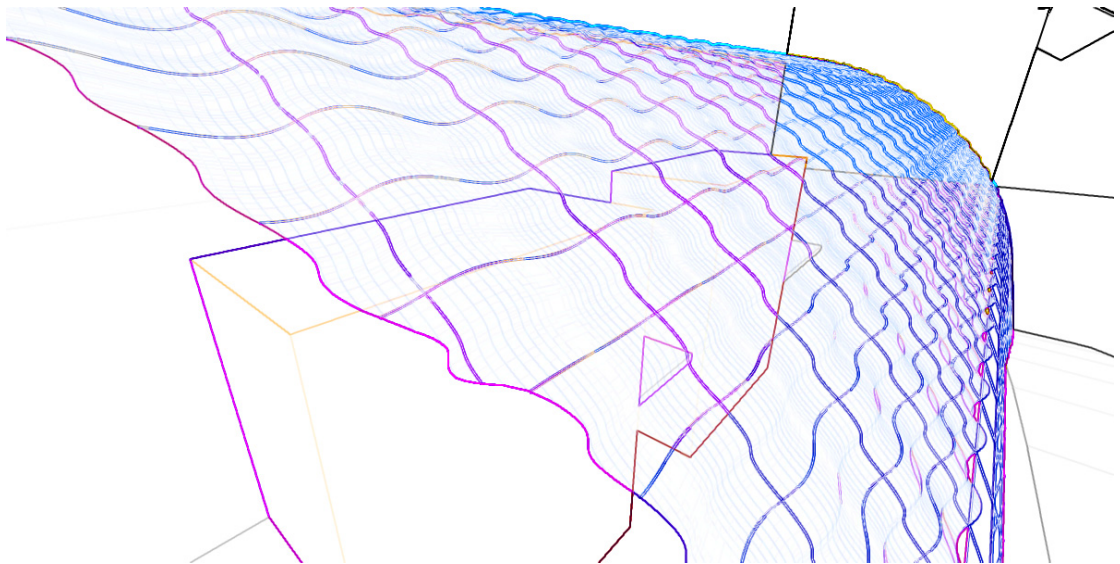


**Curved Photovoltaic Surface Optimization for BIPV:
An Evolutionary Approach
Based on Solar Radiation Simulation**

Sheng Cheng



This dissertation is submitted in partial fulfillment
of the requirements for the degree of
Master of Science in Adaptive Architecture and Computation
from the University of London

Bartlett School of Graduate Studies
University College London

September 2009

I, Sheng Cheng, confirm that the work presented in this thesis is my own. Where information has been derived from other sources, I confirm that this has been indicated in the thesis.

Abstract

The paper attempts to address the problem of the optimization of curved photovoltaic surfaces that may become the alternatives of the traditional flat PV surfaces in BIPV. The proposed method combines three parts: an evolutionary algorithm (Genetic Algorithm) for optimization, an adaptive simulation tool based on Hay's anisotropic radiation model, and a comparison module for analysis. The cladding problem of curved PV modules is geometrically solved that may serve as the starting point for practical links with architectural and PV engineering considerations. A systematical approach is established for the comparisons between the curved and flat surfaces according to various surface angle-settings (tilt angle and azimuth angle) and solar condition setups (latitude and radiation mode), involving specific 3D and 2D radiation plots and related data recording system. Through a series of experiments, the paper presents the characteristics of curved surfaces in terms of the solar energy gain, such as the stabilization characteristic and the mean total annual solar radiation, etc. The capacities of the algorithm are confirmed and several findings are discussed and concluded so as to be used as references for BIPV projects and other practical photovoltaic appliances.

Keywords: curved photovoltaic surface; BIPV; Genetic Algorithm; Hay's anisotropic radiation model; cladding; tilt angle; azimuth angle; latitude; radiation mode; 3D and 2D radiation plots;

Acknowledgment

I would like to thank my supervisors and course directors:

Alasdair Turner, for his valuable advice, inspirational discussion and programming support

Ava Fatah, for her guidance in critical-thinking cultivation

Sean Hanna, for his contribution of broad computational knowledge

*Also many thanks to **Ankon Mitra**, my friend, for his help and encouragement*

*Finally I am grateful to my fiancée, **Yan Zeng**, for her endless care and consistent support all through.*

Table of Contents

| | |
|---|-----------|
| Abstract..... | 2 |
| Acknowledgements..... | 2 |
| Table of Contents..... | 3 |
| List of Illustrations..... | 5 |
| | |
| 1. Introduction..... | 7 |
| 1.1 Building-integrated photovoltaics (BIPV)..... | 7 |
| 1.2 Influence on BIPV system efficiency by angle-setting..... | 8 |
| 1.3 Thesis definitions, aims and structure..... | 10 |
| | |
| 2. Review of related work..... | 13 |
| 2.1 Research of optimal angle-setting for BIPV system..... | 13 |
| 2.2 Availability of curved PV surfaces..... | 14 |
| 2.3 Genetic Algorithm (GA) for optimization..... | 16 |
| | |
| 3. Method..... | 18 |
| 3.1 Overview of strategy and algorithm..... | 18 |
| 3.2 Anisotropic model for computing solar radiation incidence on inclined surfaces..... | 18 |
| 3.3 Computing solar radiation incidence on curved PV surfaces and cladding problem..... | 20 |
| 3.4 Optimization of curved PV surfaces by Genetic Algorithm..... | 22 |
| 3.5 Preliminary testing and specifying parameters..... | 24 |
| | |
| 4. Testing and Results..... | 27 |
| 4.1 Evolutionary analysis on a single optimization process..... | 27 |
| 4.2 Analysis on results of different latitudes..... | 31 |
| 4.3 Analysis on results of different angle-settings..... | 34 |
| 4.4 Analysis on importance of stabilization coefficient... .. | 40 |
| | |
| 5. Demonstrations for Practical Application..... | 42 |
| 5.1 Review of ECN-building (NL) and new target..... | 42 |
| 5.2 Optimization of curved PV lamellas for façade shading system..... | 44 |
| 5.3 Optimization of curved PV glass panels for roof shading system... .. | 56 |
| | |
| 6. Discussion..... | 50 |
| 6.1 Overview of findings..... | 50 |

| | |
|--|-----|
| 6.2 Critical assessment..... | 51 |
| 6.3 Further investigations..... | 51 |
| | |
| 7. Conclusions..... | 52 |
| | |
| Appendix I..... | 53 |
| I.1 Solar radiation models..... | 53 |
| I.2 Solar radiation geometry..... | 53 |
| I.3 Hay’s anisotropic model..... | 54 |
| I.4 3D and 2D radiation plots..... | 55 |
| I.5 Solar radiation in different latitudes..... | 56 |
| | |
| Appendix II..... | 58 |
| Illustrations of results of different latitudes | |
| | |
| Appendix III..... | 59 |
| Illustrations of results of different angle-settings | |
| | |
| Appendix IV..... | 93 |
| Code snippets | |
| | |
| References..... | 102 |

List of Illustrations

| | |
|--|----|
| <i>Figure 1.1.1</i> Locations of a building where photovoltaic elements can be integrated into..... | 7 |
| <i>Figure 1.1.2</i> Hierarchical PV Configurations..... | 8 |
| <i>Figure 1.1.3</i> PV elements of different technologies..... | 8 |
| <i>Figure 1.2.1</i> Eden project, Phase IV..... | 9 |
| <i>Figure 1.2.2</i> Berlin Central Station – Lehrter Bahnhof..... | 9 |
| <i>Figure 1.2.3</i> Demonstration of buildings without uniform optimal angle-settings..... | 9 |
| <i>Figure 1.3.1</i> Demonstration of the other aspect for Aim One: Movable PV sunshade systems..... | 11 |
| <i>Figure 1.3.2</i> Demonstration for Aim Two: BIPV projects with suboptimal angle-settings..... | 11 |
| <i>Figure 1.3.3</i> Demonstration for Aim Three: BIPV in house areas..... | 12 |
| <i>Figure 2.1.1</i> 2D power output plots of PV arrays according to various angle-settings..... | 13 |
| <i>Figure 2.1.2</i> Top-view-like 2D plots of PV arrays according to various angle-settings..... | 14 |
| <i>Figure 2.2.1</i> Curved acrylic PV module made of crystalline silicon cells, produced by Gloria Solar Company... | 14 |
| <i>Figure 2.2.2</i> Flexible thin-film solar panel and demonstrations of practical appliances..... | 15 |
| <i>Figure 2.2.3</i> Concentrating solar power systems, produced by SolFocus..... | 15 |
| <i>Figure 2.3.1</i> Demonstration of microstructure optimization by GA..... | 17 |
| <i>Figure 2.3.2</i> Demonstration of optimization an arbitrary curved surface by GA..... | 17 |
| <i>Figure 3.2.1</i> Demonstration of 3D solar radiation plot..... | 19 |
| <i>Figure 3.2.2</i> Demonstration of 2D solar radiation plot..... | 20 |
| <i>Figure 3.3.1</i> Demonstration of Bezier curves..... | 20 |
| <i>Figure 3.3.2</i> Demonstration of surface generated by Bezier curves..... | 21 |
| <i>Figure 3.3.3</i> Demonstration of relationship between normal vectors of an individual piece and position P_i | 21 |
| <i>Figure 3.3.4</i> Demonstration of cladding problem for curved PV surfaces..... | 21 |
| <i>Figure 3.3.5</i> Periodic pattern of sine and cosine waves..... | 22 |
| <i>Figure 3.3.7</i> Demonstration of cladding the curved PV surfaces in a 3×3 array..... | 22 |
| <i>Figure 3.3.6</i> 2D array of control points follows periodic patterns in both u and v directions..... | 22 |
| <i>Figure 3.4.1</i> A Bezier curve with two genes: movable distance & peak amplitude (\dot{L} is the wavelength)..... | 23 |
| <i>Figure 3.4.2</i> Initial population (80 individuals)..... | 23 |
| <i>Figure 3.4.3</i> Comparison of solar radiation between curved surfaces and flat surface..... | 23 |
| <i>Figure 3.5.1</i> Comparisons of appearances and 3D radiation plots of the final optimal curved PV surfaces..... | 25 |
| <i>Figure 3.5.2</i> Comparison of 2D radiation plots between the optimal curved PV surfaces and all the others..... | 25 |
| <i>Figure 3.5.3</i> Comparison of maximal, minimal and mean total annual radiations..... | 26 |
| <i>Figure 3.5.4</i> Comparisons of the four objectives of the final optimal curved surfaces between three-time run... | 26 |
| <i>Figure 4.1.1</i> Angle-setting and solar condition setup..... | 27 |
| <i>Figure 4.1.2</i> Overall view to the population at four evolutionary phases (80 individuals) | 28 |
| <i>Figure 4.1.3</i> Combined diagram of 2D radiation plots of all curved surfaces in four evolutionary phases..... | 29 |
| <i>Figure 4.1.4</i> Combined diagram of 3D radiation plots of the optimal curved surface and the flat surface..... | 30 |
| <i>Figure 4.1.5</i> Appearance of the optimal curved surface in a 3×3 PV array..... | 30 |
| <i>Figure 4.2.1</i> 3D solar radiation plots of five latitudes..... | 31 |
| <i>Figure 4.2.2</i> Evolutionary phases shown by combined 2D solar radiation plots of five latitudes..... | 32 |
| <i>Figure 4.2.3</i> Results of the final optimal curved surfaces generated for five latitudes..... | 33 |
| <i>Figure 4.3.1</i> Method for the divisions of angle-settings..... | 34 |

| | |
|--|----|
| <i>Figure 4.3.2</i> 3D radiation plot of the flat surface for the full range of angle-settings..... | 34 |
| <i>Figure 4.3.3</i> Final optimal curved surfaces for divisionary scales - F and H | 35 |
| <i>Figure 4.3.4</i> Final optimal curved surfaces for the set of divisionary scale - Hβ | 35 |
| <i>Figure 4.3.5</i> Final optimal curved surfaces for the set of divisionary scale - Hγ | 36 |
| <i>Figure 4.3.6</i> Final optimal curved surfaces for the set of divisionary scale - Hδ | 36 |
| <i>Figure 4.3.7</i> Final optimal curved surfaces for the set of divisionary scale - Hθ | 37 |
| <i>Figure 4.3.8</i> Table of stabilization ratio (Objective 2) of flat surface and curved surface, and their difference.... | 38 |
| <i>Figure 4.3.9</i> Table of ratio of mean total annual radiation of curved surface and that of flat surface..... | 38 |
| <i>Figure 4.3.10</i> Table of different standards used for estimation according to Rstab-curve and Rmean | 39 |
| <i>Figure 4.4.1</i> Comparison of Stabilization Ratio between flat surface and final optimal surface..... | 40 |
| <i>Figure 4.4.2</i> Table of selected results in terms of Rstab-flat \geq 50% and Dstab \geq 20%..... | 41 |
| <i>Figure 4.4.3</i> Table of selected results in terms of Rstab-flat $<$ 50% and Dstab \geq 20%..... | 41 |
| <i>Figure 5.1.1</i> General Laboratory of the Netherlands Energy Research Foundation ECN..... | 42 |
| <i>Figure 5.1.2</i> PV-integrated façade shading system for ECN-building No.31..... | 42 |
| <i>Figure 5.1.3</i> PV-integrated roof shading system for ECN-building No.42..... | 42 |
| <i>Figure 5.1.4</i> Data of monthly bright sunshine duration of Petten..... | 43 |
| <i>Figure 5.1.5</i> 3D radiation plot of full range of angle-settings in Petten..... | 43 |
| <i>Figure 5.2.1</i> 3D and 2D radiation plots of flat surface..... | 44 |
| <i>Figure 5.2.2</i> Combined diagrams of 2D radiation plots..... | 44 |
| <i>Figure 5.2.3</i> Combined diagrams of 2D radiation plots of other three parallel experiments..... | 45 |
| <i>Figure 5.2.4</i> Appearance and 3D radiation plot of final optimal curved surface..... | 45 |
| <i>Figure 5.2.5</i> Façade shading system configured by curved PV lamellas..... | 46 |
| <i>Figure 5.2.6</i> Hypothesis of micro curved PV module/cell..... | 46 |
| <i>Figure 5.3.1</i> Geometry of PV roof shading system of building No.42..... | 47 |
| <i>Figure 5.3.2</i> Combined diagrams of 2D radiation plots..... | 47 |
| <i>Figure 5.3.3</i> Appearance and 3D radiation plot of final optimal curved surface..... | 47 |
| <i>Figure 5.3.4</i> Close views of the roof integrated curved PV panels of the building No.42..... | 48 |
| <i>Figure 5.3.5</i> Perspectives of the ECN-building integrated curved PV shading systems..... | 49 |
| <i>Figure 5.3.6</i> Indoor view of the roof integrated curved PV of the building No.42..... | 49 |

Appendix I

| | |
|---|----|
| <i>Figure I.2.1</i> Solar radiation geometry for an inclined surface..... | 53 |
| <i>Figure I.4.1</i> 3D radiation plot by Hay's anisotropic model..... | 55 |
| <i>Figure I.4.2</i> 2D radiation plot by Hay's anisotropic model..... | 55 |
| <i>Figure I.5.1</i> 3D and 2D solar radiation plots of five latitudes..... | 56 |
| <i>Figure I.5.2</i> Comparison of 2D solar radiation plots of five latitudes..... | 57 |

1. Introduction

The problem being addressed in the study is related to the optimization of curved surfaces by Genetic Algorithm for the use of solar photovoltaic (PV) elements that can be integrated into buildings. The study, on the one hand, aims to explore the characteristics of curved PV surfaces in term of the solar energy gain, and on the other hand, through comparing them with flat PV surfaces, aims to provide references for designs of BIPV projects that in what situations curved PV surfaces could be adopted as the alternative of traditional flat ones.

1.1 Building-integrated photovoltaics (BIPV)

Architects with vision have come to understand it is no longer the goal of good design to simply create a building that is aesthetically pleasing—buildings of the future must be environmentally responsive as well (*Task 16 "Photovoltaics in Buildings"*, 1996). The technology of photovoltaics provides such a promising future for architecture. Photovoltaics (PV) modules can generate electricity from the renewable resource of sunlight without any environmental harm. BIPV (building-integrated photovoltaics) refers to the true integration of the photovoltaic elements into a building, normally when it is being built, and here the elements perform a second function as a part of the building itself (Naps Systems Oy., *Photovoltaics in Buildings - a brief introduction*, 2001). As demonstrated in Figure 1.1.1, the locations where photovoltaic elements can be incorporated into a new building usually involve three different aspects as below:

- Façade (e.g. wall, window or glazed curtain wall with certain transparency)
- Roof (e.g. slope roof, flat roof, or curved pavilion roof)
- Other functional architectural components (e.g. sunshades, glazed atria, PV skylights)

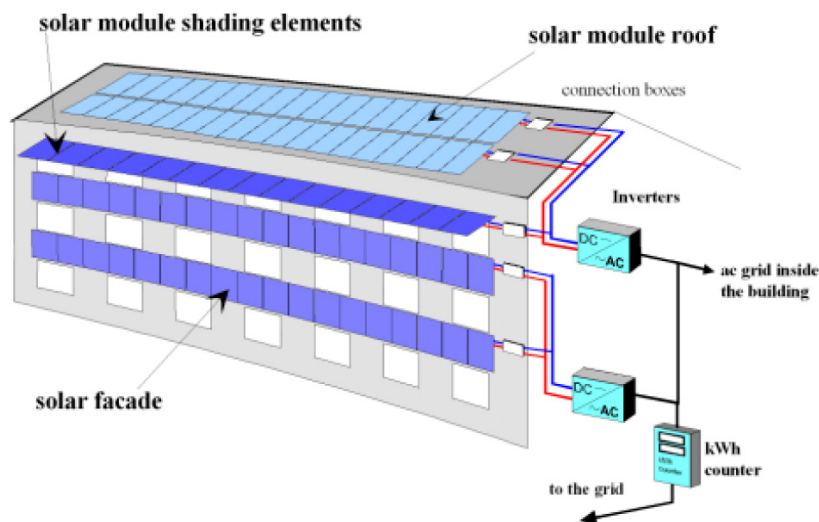


Figure 1.1.1 Locations of a building where photovoltaic elements can be integrated into

Source: Naps Systems Oy., *Photovoltaics in Buildings - a brief introduction*, 2001

The standard element of a BIPV system is the PV module. Individual solar cells are interconnected and encapsulated on various materials to form a module. Modules are strung together in an

electrical series with cables and wires to form a PV array (Figure 1.1.2). Direct or diffuse light (usually sunlight) shining on the solar cells induces the photovoltaic effect, generating unregulated DC electric power. This DC power can be used, stored in a battery system, or fed into an inverter that transforms and synchronizes the power into AC electricity. The electricity can be used in the building or exported to a utility company through a grid interconnection (Patrina Eiffert and Gregory J. Kiss, 2000).

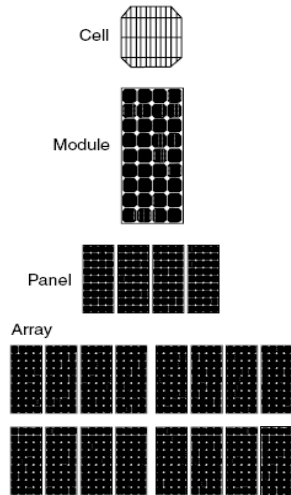


Figure 1.1.2 Hierarchical PV Configurations
 Source: Patrina Eiffert and Gregory J. Kiss, Building-Integrated Photovoltaic Designs for Commercial and Institutional Structures: A Sourcebook for Architects and Engineers, 2000



Figure 1.1.3 PV elements of different technologies
 Top: monocrystalline silicon cell and module
 Middle: polycrystalline silicon cell and module
 Bottom: thin-film amorphous silicon cell and module
 Source: http://www.bipv.ch/materiale_fotovoltaiico_e.aspl

Currently, silicon is still the major photovoltaic material. There are three basic areas of silicon technologies: monocrystalline silicon, polycrystalline silicon, and thin-film amorphous silicon. PV elements made of these three types are all being used in BIPV appliances, with their appearances differing in shape, size and colour (Figure 1.1.3). For the use of BIPV, thin-film silicon technology presents several advantages. Thin-film materials are less expensive and the material can be deposited by means of procedures which lend themselves well to continuous, large-scale production processes. Amorphous silicon modules, which cells are long narrow stripes, are less affected by shading than crystalline silicon modules. Furthermore, unlike crystalline silicon modules that the efficiency will reduce greatly if overheated, amorphous modules are less susceptible to the temperature. Although thin-film cells still have lower conversion efficiency rate (5~12%) comparing with crystalline silicon cells (15~20%), they will eventually dominate (Paul Maycock, *Building with Photovoltaics*, 1995).

1.2 Influence on BIPV system efficiency by angle-setting

The incidence of solar radiation that reaches a PV surface determines the potential electrical output of a BIPV system. In order to maximize solar access and power output, the angle-setting for the BIPV system should be optimized involving both orientation (azimuth angle) and tilt angle for PV arrays. Angle-setting will have great influence on the efficiency of a PV array and in turn on the efficiency of a whole BIPV system. When modules are connected in series, it is desirable to

have each module's maximum power production occur at the same current. Similarly, when modules are connected in parallel, it is desirable to have each module's maximum power production occur at the same voltage (Roger Messenger and Jerry Ventre, 2000). Thus, when mounting and connecting modules, it is essential to have arrays or sub-arrays with a uniform angle-setting in order to operate PV modules near their maximum power points for achieving good efficiency of the BIPV system.

Traditionally, whether or not the building could have a uniform optimal angle-setting is a determinative factor for the appliance of BIPV system. However, with the increasing popularity of BIPV, there has seen a paradox that most of the buildings cannot provide desired characteristics that the BIPV system requires. In reality, integration of PV modules into a building surface may influence the size of the modules used, the size of the array, its inclination and its direction. The figures below demonstrate some selected BIPV projects in which the PV arrays have not a uniform optimal angle-setting in terms of either tilt angle or azimuth angle, or the both.

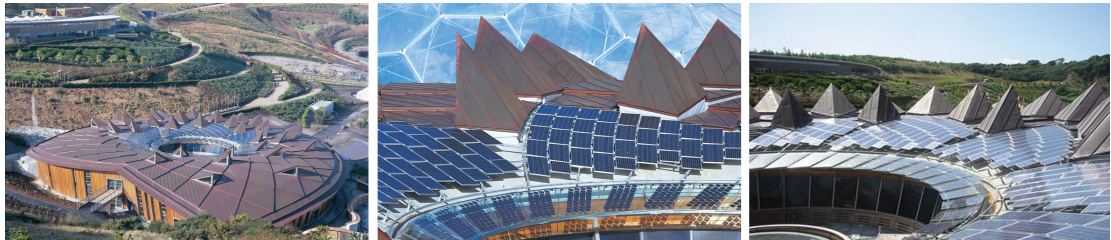


Figure 1.2.1 Eden project, Phase IV (Note: nonuniform azimuth angle for different sets of PV arrays)

Source: http://www.burohappold.com/BH/PRJ_BLD_eden_project_phase_iv.aspx



Figure 1.2.2 Berlin Central Station – Lehrter Bahnhof

(Note: neither tilt angle nor azimuth angle is uniform for PV arrays)

Source: <http://gmp-architekten.de/index.php?id=4&L=1>



Figure 1.2.3 Demonstration of buildings without uniform optimal angle-settings

Left: building in Italy (Note: nonuniform azimuth angle for PV arrays in the facade)

Source: <http://www.pvsunrise.eu/BuildingIPV.htm>

Middle: the Devonshire Building (Note: nonuniform tilt angle for PV arrays in the roof)

Source: <http://www.max4object.com/wp/?p=810>

Right: Qingdao Railway Station (Note: nonuniform tilt angle for PV arrays in the pavilion roof)

Source: <http://solar.nengyuan.net/2008/0723/1706.html>

Although such problems can be technically solved by making a careful layout for PV arrays and using necessary electronic devices like Maximum Power Point Trackers (MPPT), pleasing results are still difficult to achieve. This is also an aesthetic issue. The conflictions between architectural aesthetics and high-tech PV appliances have seen resulted in two kinds of consequences. On the one hand, architects may make a compromise so that the original design features are easily lost. On the other hand, while aesthetic considerations dominate PV installations, the purpose of achieving high efficient performance of the BIPV system is otherwise impaired. Therefore, a challenge for solving these conflictions tends to present for both architects and PV engineers.

1.3 Thesis definitions, aims and structure

Photovoltaics and architecture are a challenge for a new generation of buildings. Installations fulfilling a number of technical approaches do not automatically represent aesthetical solutions (*Task 16 "Photovoltaics in Buildings"*, 1996). One of sticking points of the challenge is the problem that the required optimal angle-setting for a BIPV system doesn't match a building or its components. Many endeavors have already been done by R&D communities, PV engineers as well as architects in order to develop high-quality integration concepts that can make better use of PV elements. However, the morphology of PV elements attracts fewer concerns. On the one hand, the flat nature of PV modules cannot help to get buildings out of the trouble where there lacks availability of either the optimal or a uniform angle-setting for a BIPV system. On the other hand, the appearance of flat PV surfaces also exposes their disadvantages for potential usages by architects, such as optional singleness and aesthetics-lacking.

As the opposite, whether PV surfaces with non-flat characteristic could become an alternative of flat PV surfaces has not been well explored yet. In this context, an audacious hypothesis is made: if a single PV module with certain acceptable curvatures (where acceptable means no critical impact on the efficiency of the module itself), the curved surface might be used as the means to ease the problems caused by nonuniform or suboptimal angle-settings for BIPV systems. This approach may also help to release criticisms on the aesthetic problem of BIPV and enhance the richness of PV products, providing architects a wide range of opportunities for the designs of BIPV projects.

With the above purpose, the key of the hypothesis will lie in the investigation on characteristics of curved surfaces in terms of the solar energy gain. In order to gain a comprehensive cognition on curved PV surfaces, a global computing model is established which is capable for calculations in terms of any selected locations as well as angle-settings. By means of an evolutionary approach—Genetic Algorithm, curved surfaces are able to be optimized according to predesigned objectives which involve the relative data of flat surfaces. Therefore, the generated curved PV surface by the algorithm can be compared with the flat PV surface under the same given condition, and the characteristics of the curved surface can be achieved. In this respect, the study is primarily aimed to examine the appropriateness of the proposed method by documenting and critically assessing its results and thus attempt to provide references for the designs of BIPV projects. Besides, three relative aims with practical concerns can also be derived from the above proposed method.

Aim One

The proposed method can be used to optimize curved PV surfaces for the BIPV projects which cannot provide the uniform angle-setting for mounting PV elements. Many examples of this aspect have already been shown in the last chapter. Herein, the other different aspect with the similar problem will be introduced. As demonstrated by Figure 1.3.1, the movable sunshade systems made of PV modules have a problem of the change in the tilt angle for shading and opening, but the adjustment of the tilt angle is difficult to correspond to the optimal angle for maximizing solar radiation gain. Suitable curved PV surfaces might be otherwise generated by the algorithm for this type of BIPV appliances (an example with more details will be discussed in Chapter 5).



Figure 1.3.1 Demonstration of the other aspect for Aim One: Movable PV sunshade systems

Left: Colt Shadovoltaic System

Source: <http://www.archiexpo.com/prod/colt/photovoltaic-glass-solar-shading-52229-127570.html>

Middle: Kawneer's 1600 PowerShade

Source: http://www.solarglazingmag.com/?attachment_id=302

Right: Movable solar shading device, made of transparent modules (Photo: Denis Lenardic)

Source: <http://www.pvresources.com/en/transparent.php>

Aim Two

A BIPV project may be restricted by other conditions so as not to offer the optimal angle-setting for the desired power output. The examples for this type can be seen in Figure 1.3.2. In these situations, the algorithm can be used to generate the curved PV element with the higher performance than the flat PV element. But a balance also need be made between environmental factors, surrounding constraints as well as aesthetic considerations.



Figure 1.3.2 Demonstration for Aim Two: BIPV projects with suboptimal angle-settings

Left: BMW museum solar roof, Munich, Germany (note: the optimal tilt angle in the location is around 45°)

Source: <http://www.ecoconsciouspioneers.com/page/2/>

Middle: Suntech Headquarter solar façade, Wuxi, China (note: the optimal tilt angle in the location is around 27°)

Source: <http://www.suntech-power.com/productsen/BIPV/BIPVcasestudies/LIGHTTHRU/casestudies/suntech.htm>

Right: Kyocera Headquarter solar façade, Kyoto, Japan (note: the optimal tilt angle in the location is around 36°)

Source: <http://global.kyocera.com/>

Aim Three

Another more ambitious concept that may be far from feasible for the time being is still worthy mentioning. It is well known that the most promising future of BIPV indeed rely on the wider appliances in numerous houses all over the world. Since the explosion of the latest worldwide economic crisis, BIPV for housing has been attracted increasingly more attention from the governments of both industrial and developing countries. In despite of a lot market issues yet requiring to be solved, the way of integrating PV into houses also needs be further explored, especially by architects. Figure 1.3.3 shows the current way of mounting PV elements on the house roof, in which design features still lack sufficient aesthetic considerations. Moreover, a very common phenomenon can also be easily noticed that the planning design of a housing area often involves nonuniform tilt angle for slope roofs and nonuniform orientation for houses, and these angle-settings are hardly optimum. But by means of the proposed method, all of the disadvantages could be used as the input data for the optimization of a specific curved PV tile that may be more suitable for the housing area than the traditional flat PV element in terms of the solar gain, and more importantly, aesthetic solutions may be also obtained at the same time.



Figure 1.3.3 Demonstration for Aim Three: BIPV in house areas

Source of left: <http://www.dotrose.com/misc/computer/solar-pc/>

Source of middle: <http://www.iproperty.com.my/property/township.aspx?tid=41>

Source of right: Naps Systems Oy., Photovoltaics in Buildings - a brief introduction, 2001

Given the thesis and the aims for the study, several related work and relevant state-of-the-art of BIPV will be mentioned in Chapter 2. The methodologies involving different aspects for the study will be explained in Chapter 3. As followed in Chapter 4, a series of systematical testing will be described and the results produced will be analyzed. At the end of the chapter, some findings and tentative statements will be given for the use of the next chapter as well as other later possible practical concerns. In Chapter 5, the specific experiments are made for a real BIPV project involving both two aspects of Aim One so as to gain a practical experience of the proposed method. The overall assessment of the study will be given in Chapter 6 and followed by outlining some possible directions for its further development. The final chapter will present the conclusions in terms of the overall review to the study.

2. Review of Related Work

2.1 Research of optimal angle-setting for BIPV system

Tilt angle and azimuth angle are the most important factors that determine the power output of a BIPV system. Many researchers from various perspectives have contributed their work into this area. As a fundamental tool for the research, a computing model is always pre-requisite for the calculation of solar radiation. Among different solar radiation models, the anisotropic radiation models have been most widely used, such as Hay's anisotropic model. Based on the radiation model and necessary input data of the site, the optimal tilt and azimuth angles for a certain location can be found and the effects of other different angle-settings may also be explored.

The performance of PV arrays at different tilt angles and orientations for Guangzhou city (latitude 27°N) was investigated by Chen Wei et al. According to their report (Chen, Shen and Liu, 2009), the monthly average power output of the PV arrays at different angle-settings has a nearly same trend in the spectrum with the monthly average solar radiation incidence on them. This finding approved that the amount of solar radiation on a PV array is the major factor that determines its system efficiency. From the graphs of 2D power output plots of PV arrays (Figure 2.1.1), it was also concluded that the optimum value of yearly power output can be obtained from PV array facing south with a tilt angle of 19°. Yang et al investigated the optimal tilt angle and azimuth angle for a wider range of locations in China by means of a specifically developed mathematical equation based on the anisotropic model (Yang, Mao and Chen, 2001). The result showed that the optimal tilt angle for maximum yearly solar radiation is usually smaller than the local latitude, except the areas where the beam radiation occupies a great proportion of the total solar radiation.

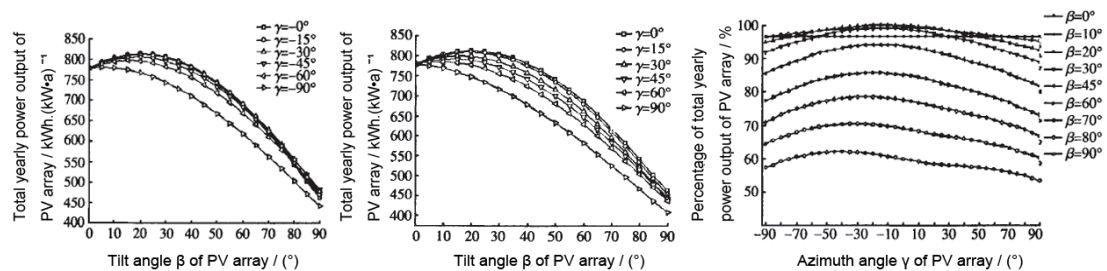


Figure 2.1.1 2D power output plots of PV arrays according to various angle-settings

Left: Effect of tilt angle & orientation on total yearly power output of PV array (east south facing)

Middle: Effect of tilt angle and orientation on total yearly power output of PV array (west south facing)

Right: Percentage of total yearly power output of PV array at different tilt angles and orientations

Source: Chen Wei, Shen Hui and Liu Yong, Performance Evaluation of PV Arrays at Different Tilt Angles and Orientations in BIPV, 2009

Danny H.W. Li and Tony N. T. Lam (2007) introduced a numerical approach to calculate the solar radiation on inclined surface by integrating the measured sky radiance distributions—the recorded data of 10-minute horizontal radiation and sky radiance for the whole year (2004) in Hong Kong. Besides the more accurate optimal angle-setting for Hong Kong could be achieved, this approach, from a different perspective, also provided a new way for analysis, in which top-view-like 2D

plots were developed for comparisons between the beam radiation, the sky-diffuse radiation and the energy output of PV arrays (Figure 2.1.2).

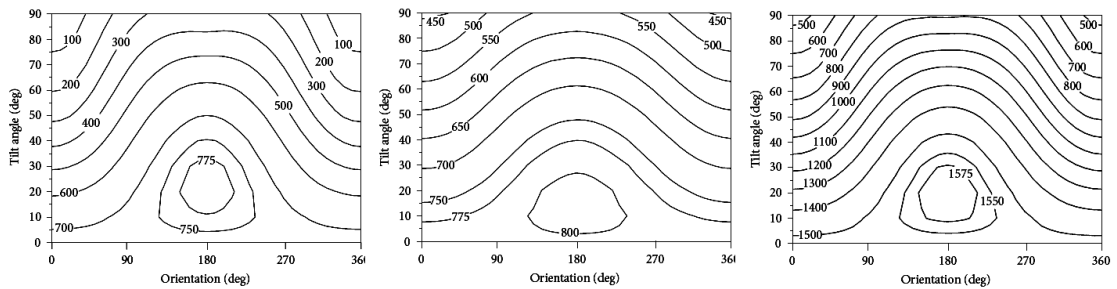


Figure 2.1.2 Top-view-like 2D plots of PV arrays according to various angle-settings

Left: Annual beam solar radiation (kWh/m²) for various tilt angles and orientations

Middle: Annual sky-diffuse and reflected solar radiation (kWh/m²) for various tilt angles and orientations

Right: Annual total solar yield (kWh/m²) for various tilt angles and orientations

Source: Danny H.W. Li and Tony N. T. Lam, Determining the Optimum Tilt Angle and Orientation for Solar Energy Collection Based on Measured Solar Radiance Data, 2007

Using 2D plots for analysis of solar energy gain is quite common for the researches of this kind. But this approach is not convenient for multi-variable analysis in the study of this paper, so a comprehensive approach involving adaptive 3D and 2D solar radiation plots is developed for comparisons of the results produced by the experiments (details will be explained in Chapter 3).

2.2 Availability of curved PV surfaces

As the study is related to the optimization of curved surfaces for BIPV, it is essential to gain knowledge about the state-of-the-art involving curved surfaces being developed for PV elements. In appliances of photovoltaics where flat elements are dominant, curved PV elements are still uncommon. Some of the researches are just started since very recently. Nevertheless, thanks to the development of related PV appliance fields like auto industry, a few PV products with curved features begin to show up. Herein, three types of curved PV elements will be presented.

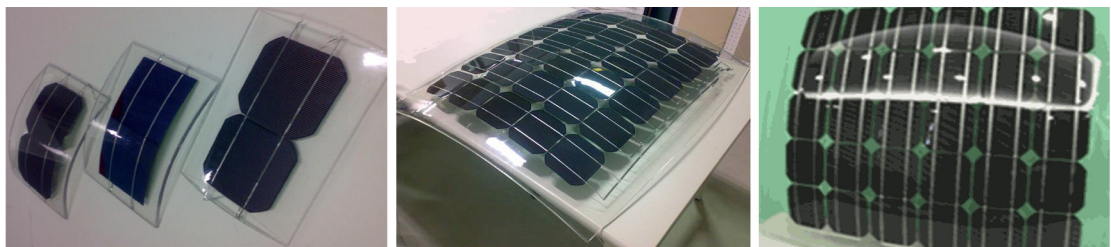


Figure 2.2.1 Curved acrylic PV module made of crystalline silicon cells, produced by Gloria Solar Company

Source: http://www.alibaba.com/product-free/101628519/Acrylic_PV_module/showimage.html

<http://www.greentechmedia.com/articles/read/for-solar-car-roof-its-all-about-curves/>

The first type can be demonstrated by an acrylic PV panel (Figure 2.2.1), which is made of crystalline silicon solar cells on plastic rather than glass. This curved PV panel is developed for the purpose of integration over a compact electric car's roof. According to the producer Sam Wu, making a panel that can curve and hug the entire rooftop is tricky. But he also noted that

parabolic-shaped panels could also find uses in integrating solar panels into buildings which is their primary focus, “Everybody claims they can do building-integrated PV, but theirs are flat, not curved”, Wu said (*For Solar Cars, It’s All About Curves*, 2009).

Comparing with the above type, the second type of curved PV surfaces should have a much broader perspective. As mentioned in Chapter 1.1, thin-film amorphous silicon technology has a lot of advantages over other silicon technologies, and the most obvious one might be that a-Si PV surfaces are allowed to be desirably bended. Usually, PV elements of this type are called flexible solar panels (Figure 2.2.2). Researchers at PNNL will create these flexible panels by adapting a film encapsulation process currently used to coat flat panel displays that use organic light-emitting diodes, or OLEDs. According to Mark Gross, a senior scientist at PNNL, that the flexible solar panels could be placed on rooftops like shingles and could replace today's boxy solar panels that are made with rigid glass or silicon and mounted on thick metal frames. Some small scale appliances have already been launched. Prospective future may rely on many latest large BIPV projects, like the new Terminal 2 of Heathrow, designed by Foster and Partners.



Figure 2.2.2 Flexible thin-film solar panel and demonstrations of practical appliances

Left: Flexible solar panel (photo courtesy of Vitex Systems, Inc.); Source: <http://www.pnl.gov/topstory.asp?id=376>

Middle: Bus stop lit by solar power; Source: <http://www.azobuild.com/news.asp?newsID=6692>

Right: Foster + Partners' design for Heathrow Terminal 2;

Source: http://www.worldarchitecturenews.com/index.php?fuseaction=wanappln.projectview&upload_id=12133

The third type is based on a different principle. Concentrating photovoltaic systems from SolFocus use lenses or mirrors to focus sunlight onto high-efficiency solar cells (Figure 2.2.3). The full design calls for a multilayered solar panel with the transparent electronic tracker, a plastic “internal reflection” concentrator, and a high-efficiency solar cell. The CEO of company, Colin Williams, claimed that because the tracker and concentrator are transparent, an artistic pattern could be put onto the panel, making it possible to use it on a building façade (Martin LaMonica, *With transparent HP tech, pretty solar buildings*, 2008).



Figure 2.2.3 Concentrating solar power systems, produced by SolFocus

Source: http://news.cnet.com/8300-11128_3-54-3.html?keyword=solar+power

2.3 Genetic Algorithm (GA) for optimization

Genetic Algorithms (GA) usually refers to adaptive computing algorithm inspired by the evolutionary and genetic ideas of natural selection for the use of optimization or search problems. The basic concept is to simulate the evolution process of an abstract population—a number of randomly generated individuals—in order to evolve toward better generations by means of procedures like inheritance, selection, crossover, mutation and evaluation. In GA, each individual usually has both Genotype and Phenotype. Genotype is used to store all the gene information of an individual, while Phenotype is used for evaluating and sorting within the population according to its fitness, as well as displaying characteristics of the individual in visual. A typical process of GA can be described as below:

In each generation, the fitness of every individual in the population is evaluated, multiple individuals are stochastically selected from the current population (based on their fitness), and modified (recombined and possibly randomly mutated) to form a new population. The new population is then used in the next iteration of the algorithm. Commonly, the algorithm terminates when either a maximum number of generations has been produced, or a satisfactory fitness level has been reached for the population. If the algorithm has terminated due to a maximum number of generations, a satisfactory solution may or may not have been reached.

(Source: http://en.wikipedia.org/wiki/Genetic_algorithm)

The GA developed for this study is related to using solar gain as the input data for the optimization of curved PV surfaces, which combines the morphology evolution of curved surfaces and the simulation of the external force of solar energy (details will be discussed in Chapter 3). The approach shares a similar principle with another experiment for microstructure optimization developed by Siavash Haroun Mahdavi and Sean Hanna (2003).

Their approach involved a GA for evolving the topology of the structure and a separate, deterministic process for calculating details of the shape based on structure engineering principles. The aims were to generate a repeatable structure which minimized weight and maximized strength, while considering the specific properties of the material in which it is built. The factors taken into consideration when determining the fitness of each individual in the population are as follows:

- The number of angles below 30° (weight: A = 2.0)
- The overall weight of the individual (weight: W = 0.4)
- The maximum deflection within the system (weight: D = 3.0)
- Whether the iterative node placement had found a solution that settled down (weight: C = 2.0)

These four variables were then put into the following equation for each test under a different stress condition (T):

$$T = \frac{1}{(1 + A \times \text{lowAngles} + W \times \text{weight} + D \times \text{maxDeflection} + C \times \text{count})}$$

The results showed that the number and size of structural members was seen to decrease over the course of the run while maintaining a stable and viable structure within the constraints provided.

Figure 2.3.1 demonstrates the primary information of GA used, involving respectively the cube frame for the structure, the abstract representation of the topology of the evolved structure unit, and the stereolithographic model composed of the repeated optimal unit.

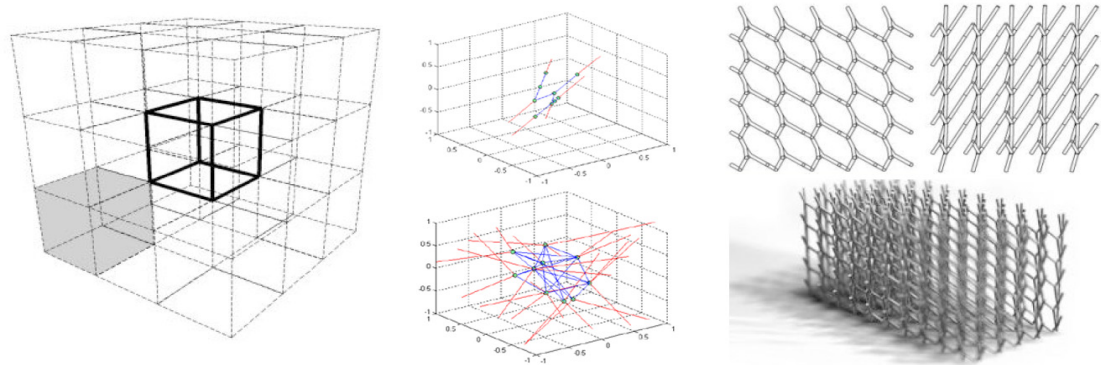


Figure 2.3.1 Demonstration of microstructure optimization by GA

Left: An array of 26 outer cubes surrounding the central cube

Middle: A unit cube of the best individual (middle top) and an average individual (middle bottom) evolved

Right: The top and side views of the final structure evolved and a 10 x 5 x 5 example of the evolved structure

Source: Siavash Haroun Mahdavi and Sean Hanna, An evolutionary approach to microstructure optimization of stereolithographic models, 2003

Another experiment done by the author was to optimize an arbitrary architectural surface in terms of the distribution of the solar gain. The strategy of surface optimization was using GA to generate three new faces above the original frame of each piece of the surface in order to change the average solar energy per unit, and thus meliorate the solar energy distribution in the whole surface. This strategy could keep the morphological form or structure of the original surface by giving a same offset value to each piece, but at the same time lead to increasing the complexity of the surface because of adding more faces and structural elements. According to different requirements, proper states might be found and compared during the programme running by manually controlling the offset value. Figure 2.3.2 shows three selected stages in the optimization by GA, in which the distribution of the solar gain is represented by numerically controlled HSB color mode. Visually, the color distribution is becoming more mixed than the initial state, which indicates that the solar energy gain of the new optimized surface is becoming evener than the original one.

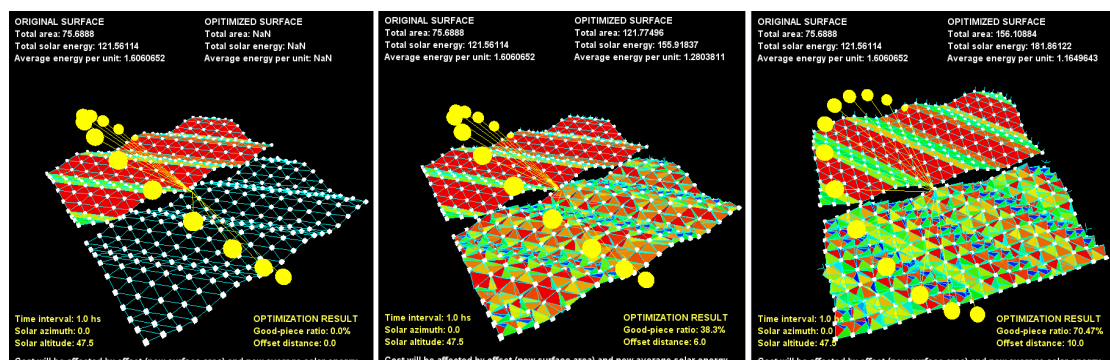


Figure 2.3.2 Demonstration of optimization an arbitrary curved surface by GA

Left: Original curved surface represented by topological frame and its original distribution of solar gain

Middle: State being optimized with Offset value = 6.0 and Good-piece ratio = 38.3%

Right: State being optimized with Offset value = 10.0 and Good-piece ratio = 70.47%

3. Method

3.1 Overview of strategy and algorithm

The optimization of curved PV surfaces is aimed at looking for the alternative of flat PV surfaces in the situations in which flat surfaces might not have satisfying performances in terms of the usage of solar energy. The strategy for the algorithm used includes Hay's anisotropic model for simulating solar radiation, curved surface programming for the problems of calculation and cladding, and Genetic Algorithm for optimization. In virtue of Hay's model, the algorithm is equipped with a global capacity providing opportunities for a wide range of comparison environments according to various angle-settings and solar condition setups.

A specific analysis system was also established involving using 3D and 2D solar radiation plots to evaluate all generated curved PV surfaces and make comparisons with the flat surface during the optimization process. In the Genetic Algorithm, the fitness for individuals is defined carefully. There are four objectives used for the evaluation of individual's fitness, taking into account different aspects in searching for better-fit individuals for the evolution of the population. Through preliminary testing, the four objectives were appropriately weighted and values of relative parameters were affirmed too, which could thus be used for the formal experiments in Chapter 4.

3.2 Anisotropic model for computing solar radiation incidence on inclined surfaces

Hay's anisotropic model (Hay, 1979) is chosen as a simulation tool of solar radiation—the environmental data for the optimization process. In Hay's model, total radiation incident on an inclined surface has three components: direct (or beam) radiation, sky-diffuse radiation (e.g. reflected from clouds, and scattered radiation) and ground-reflected radiation, which can be expressed as:

$$H_T = H_B' + H_D' + H_R' \quad \text{Formula (1)}$$

Where:

H_T total solar radiation on an inclined surface, MJ • (m² • day)⁻¹

H_B' direct solar radiation on an inclined surface, MJ • (m² • day)⁻¹

H_D' diffuse solar radiation on an inclined surface, MJ • (m² • day)⁻¹

H_R' ground-reflected radiation on an inclined surface, MJ • (m² • day)⁻¹

More formulas and details of calculations can be found in Appendix I.3 and also may refer to Hay's paper *Calculation of monthly mean solar radiation for horizontal and inclined surfaces*, 1979. While Hay's anisotropic model was established, all input data required for the calculation of radiation actually come from two aspects: the data of the inclined surface (including surface azimuth angle γ and surface tilt angle β), and the geographical data of the location (including latitude L and bright sunshine duration n). Thus, H_T can be expressed as a function of L , n , β and γ : $H_T = f(L, n, \beta, \gamma)$. Bright Sunshine Duration (n , hr) is a set of daily data recorded by local

observatories, serving as an important parameter taking into account the cloud cover effect. The fractional possible bright sunshine (n/N) is used in Hay's model (N is theoretical day length, hr, which is calculated in terms of the latitude L and the solar declination δ). As the data of bright sunshine duration are various from site to site, from year to year, and observational networks are yet inadequate, an ideal condition (clear-sky mode, n/N equals to 1.0) is adopted at first for the global testing of the algorithm in Chapter 3 and Chapter 4. Cloud-cover mode (n/N is less than 1.0) will be used for a real BIPV example in Chapter 5.

As mentioned in Charter 2 that most of the solar radiation diagrams are demonstrated in the format of 2D plots in terms of angle-settings (e.g. Chen W. et al, 2009), which may not be able to serve as an intuitive tool for the comparison between different locations as well as that between GA-generated curved PV surfaces and flat surfaces. Hence, an adaptive 3D solar radiation plot is conceived which can demonstrate various results more easily. In the Cartesian coordination system (Figure 3.2.1), the red axis (X), the green axis (Y) and the blue axis (Z) represent respectively: surface azimuth angle γ (range from -90° to 90° , facing east is negative), surface tilt angle β (range from 0° to 90°), and total annual solar radiation incidence E_{year} ($\text{MJ} \cdot (\text{m}^2 \cdot \text{year})^{-1}$). Note that the reason to choose total annual solar radiation rather than daily or monthly solar radiation is in fact the practical considerations—providing relevant yearly data for the designs of BIPV projects (e.g. load of PV system is usually in $kWh/year$).

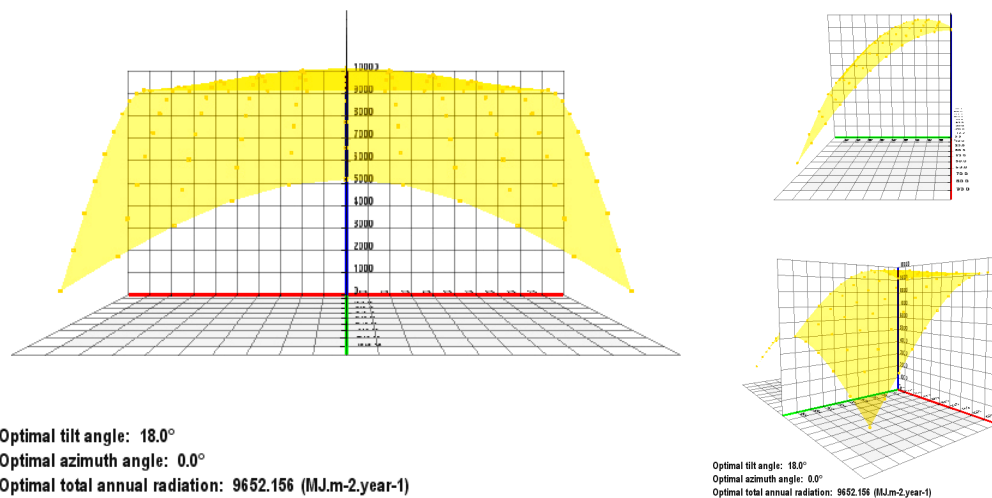


Figure 3.2.1 Demonstration of 3D solar radiation plot

Left: front view; right top: side view; right bottom: perspective

(Angle-setting: $\beta = 0^\circ \sim 90^\circ$, $\gamma = -90^\circ \sim 90^\circ$; solar condition setup: $L = 23^\circ N$, clear-sky mode. Note: L equals to Guangzhou's latitude, the optimal tilt angle is 18° that can be compared with Chen's 19° in cloud-cover mode)

Total 121 nodes (11 by 11 nodes) are used to display the 3D plot, which is suitable for ordinary experiments. The optimal position with the maximal total annual radiation is represented by the highest node of the 3D plot. The X , Y and Z components of the highest node are just the set of optimal values: γ , β and E_{year} (information can be found at the bottom of Figure 3.2.1). If spread these 121 nodes one by one into another type of 2D dimension, this new 2D plot is also suggestive for the use of analysis (Figure 3.2.2). The sequence of the nodes refers to the original 2D array of β and γ (nodes $[\beta_i]$ $[\gamma_i]$) in the Processing code. The spectrum formed by 2D plot nodes can offer

important information for comparisons, such as the general trend, local features and the stabilization characteristic within the given range of angle-settings. Moreover, the horizontal yellow line in the middle is marking the mean total annual solar radiation, which is one of the key factors to evaluate the quality of a generated curved PV surface.

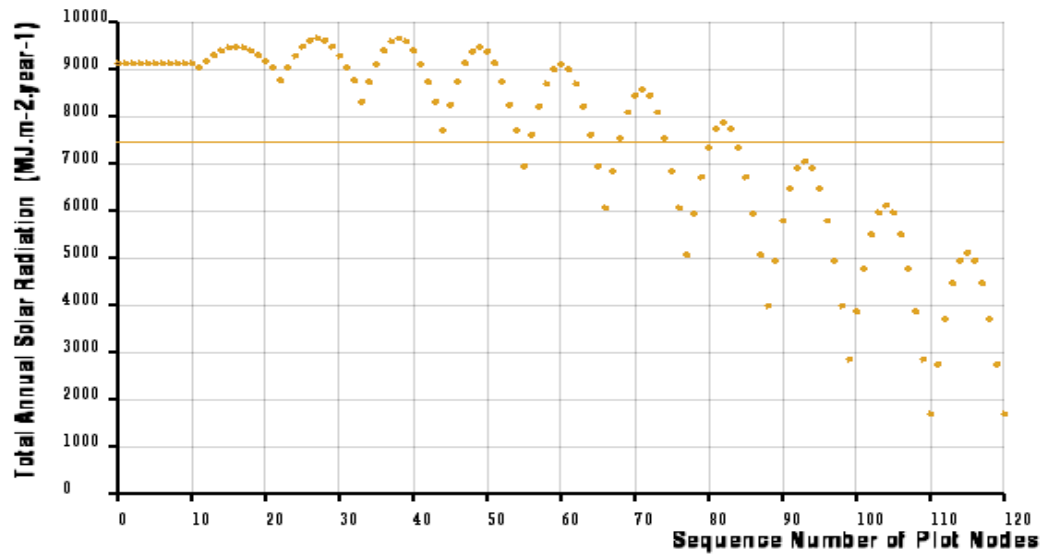


Figure 3.2.2 Demonstration of 2D solar radiation plot

(Angle-setting: $\beta = 0^\circ \sim 90^\circ$, $\gamma = -90^\circ \sim 90^\circ$; solar condition setup: $L = 23^\circ N$, clear-sky mode. Note: the horizontal yellow line shows that the mean total annual radiation is around $7500 \text{ MJ} \cdot (\text{m}^2 \cdot \text{year})^{-1}$)

3.3 Computing solar radiation incidence on curved PV surfaces and cladding problem

The measurement of solar radiation on curved surfaces is derived from the method for inclined flat surfaces mentioned in last chapter. The topology of a curved surface is usually represented as a spread of nodes connecting to each other in certain smooth patterns, such as Bezier curves. A single Bezier curve can be defined parametrically by a set of control points (Figure 3.3.1). Two Bezier curves in a crossing relationship (represented by a 2D array of control points) can be used to generate two sets of surface nodes for each direction (usually called u direction and v direction), forming the topology of a curved surface. This curved surface can be easily rendered by means of a number of small triangular faces formed by every three adjacent surface nodes (Figure 3.3.2).

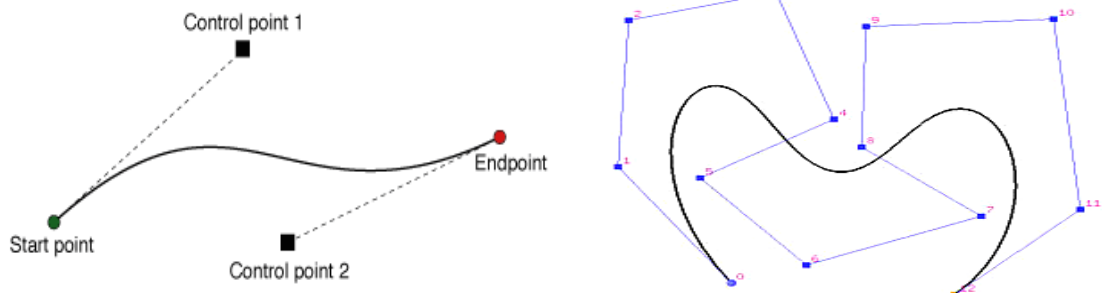


Figure 3.3.1 Demonstration of Bezier curves

Left: Bezier curve with two control points; right: Bezier curve with eleven control points

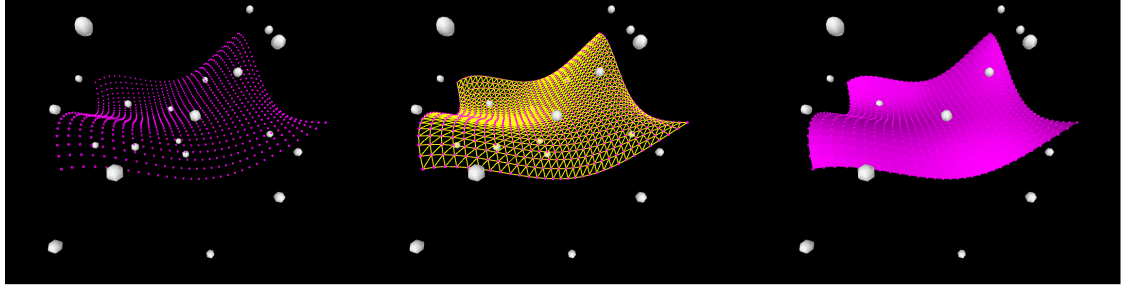


Figure 3.3.2 Demonstration of surface generated by Bezier curves

Left: surface nodes; middle: triangular faces; right: rendered surface (white balls are 2D-array control points)

Since the curved surface is composed of many small triangular pieces which are all flat (three points can define a plane), they can be regarded as many single inclined surfaces and thus be measured individually using Hay's anisotropic model. The results of all pieces can be summed up to get an overall radiation of the curved surface and the average radiation of it is calculated by:

$$E_{sum} = \sum E_i = \sum (e_i * s_i) \quad \text{Formula (2)}$$

$$\bar{e} = E_{sum} / S_{sum} \quad \text{Formula (3)}$$

Where:

\bar{e} average total annual solar radiation on the whole curved surface ($\text{MJ} \cdot (\text{m}^2 \cdot \text{year})^{-1}$)

E_{sum} total annual solar radiation on the whole curved surface ($\text{MJ} \cdot \text{year}^{-1}$)

S_{sum} total area of curved surface (m^2)

E_i total annual solar radiation on a single triangular piece of the curved surface ($\text{MJ} \cdot \text{year}^{-1}$)

e_i total annual solar radiation on a single triangular piece of the curved surface, that equals to the radiation on any parallel inclined surface of it ($\text{MJ} \cdot (\text{m}^2 \cdot \text{year})^{-1}$)

s_i area of a single triangular piece of the curved surface (m^2)

In order to calculate e_i , the tilt angle and the azimuth angle of each triangular piece are required, which can be calculated if the position of the curved surface (reference position ' P_i ') is defined. The angle-setting [β_i] [γ_i] can be regarded as the referent position for a curved surface when a range of tilt angle β and azimuth angle γ is given. The trick for the calculation is to use the other two angular parameters: $\Delta\beta$ and $\Delta\gamma$, which can be measured by the normal vector of each individual piece to the normal vector of the plane of the reference position P_i (Figure 3.3.3).

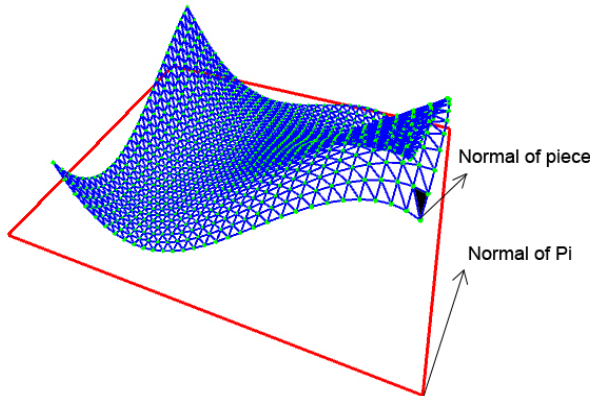


Figure 3.3.3 Demonstration of relationship between normal vectors of an individual piece and position P_i

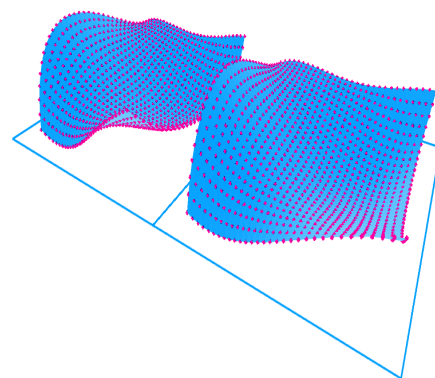


Figure 3.3.4 Demonstration of cladding problem for curved PV surfaces

Unlike flat PV modules with straight profiles, the profile of a curved surface is usually having different curvature in each side, so it tends to be a challenge for cladding curved PV modules. Two same curved PV surfaces can be put together side by side but they possibly have no any joint at all so as not to be fabricated (e.g. Figure 3.3.4). Before tackling the problem, we might be inspired by another type of special curves: trigonometric curves. The trigonometric graphs (e.g. sine and cosine waves) are periodic, which means the shape repeats itself exactly after a certain amount of distance (Figure 3.3.5). So the strategy used is to add the periodic characteristics to Bezier curves to allow a curved surface repeating itself in each side of the profile. Every control point of the 2D array is initiated as a sum of two vectors along independent sine/cosine waves in u and v directions respectively (Figure 3.3.6) so that the Bezier curves could get well controlled following some certain periodic patterns. The curved surfaces can thus be endowed with the feature of repeatability and be able to be seamlessly joined together (Figure 3.3.7).

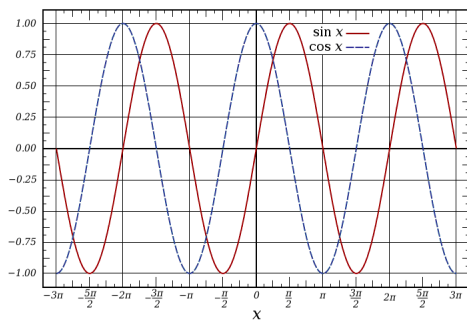


Figure 3.3.5 Periodic pattern of sine and cosine waves
Source: http://en.wikipedia.org/wiki/Sine_wave

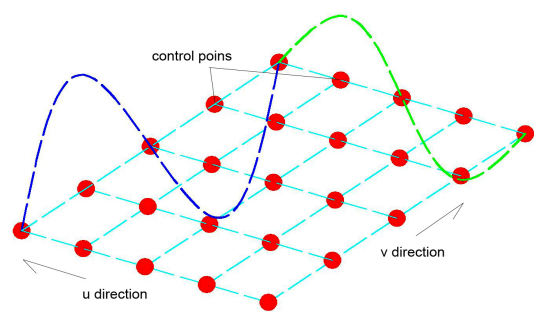


Figure 3.3.6 2D array of control points follows periodic patterns in both u and v directions

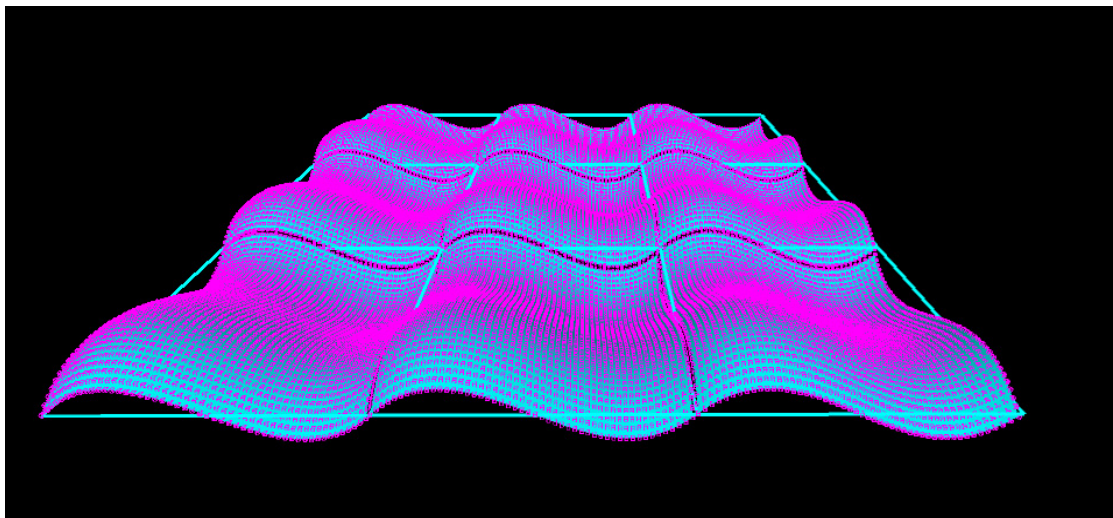


Figure 3.3.7 Demonstration of cladding the curved PV surfaces in a 3×3 array

3.4 Optimization of curved PV surfaces by Genetic Algorithm

The definitions of Genotype and Phenotype for curved PV surfaces are the key for a successful GA optimization. For each individual (curved surface), the class of Genotype (written in Processing language) contains four different genes that are related to the two Bezier curves used to generate periodic patterns in both u and v directions. Each Bezier curve has two genes—one records the ‘movable distance’ along its own direction (either u or v) and the other limits a peak

amplitude for its control points in the normal direction of the plane defined by u and v (Figure 3.4.1). Through testing, the range for moveable distance is set to $[-0.375\hat{L}, 0.375\hat{L}]$ and that for amplitude is $[0, 0.5\hat{L}]$ (\hat{L} is the wavelength). Note that the original positions of control points are distributed evenly at first, and only two corresponding control points (the second and the fourth) need be moved randomly by GA mutation function. Within the given ranges of tilt angle β and azimuth angle γ , the optimal position ($[\beta_{opt}] [\gamma_{opt}]$) of the flat surface is chosen as the first reference position ' P_o ' used to initiate all curved surfaces and the radiations according to all angle-settings ($[\beta_i] [\gamma_i]$) could be calculated. When the initial population is randomly generated at the beginning (Figure 3.4.2), the 3D and 2D radiation plots (in purple) of each individual can be immediately displayed together with that (in yellow) of the flat surface (Figure 3.4.3).

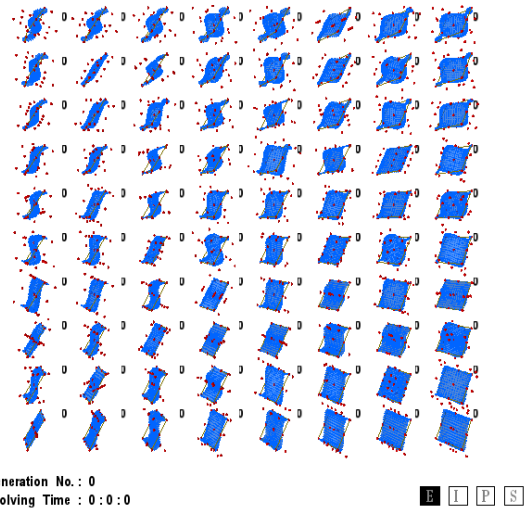
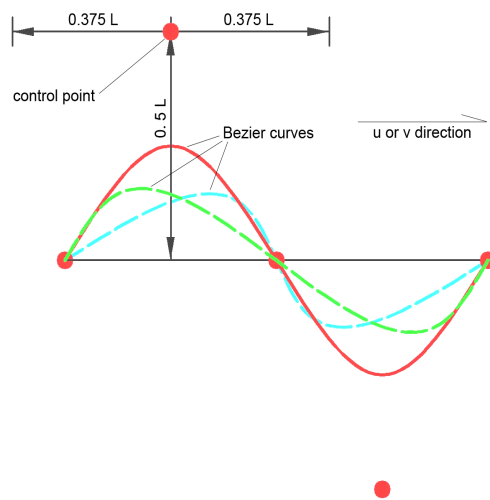


Figure 3.4.1 A Bezier curve with two genes: movable distance & peak amplitude (\hat{L} is the wavelength)

Figure 3.4.2 Initial population (80 individuals)

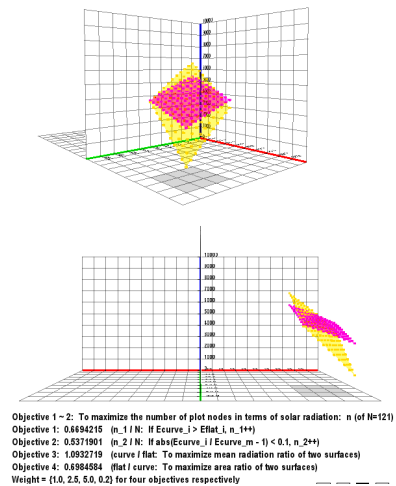
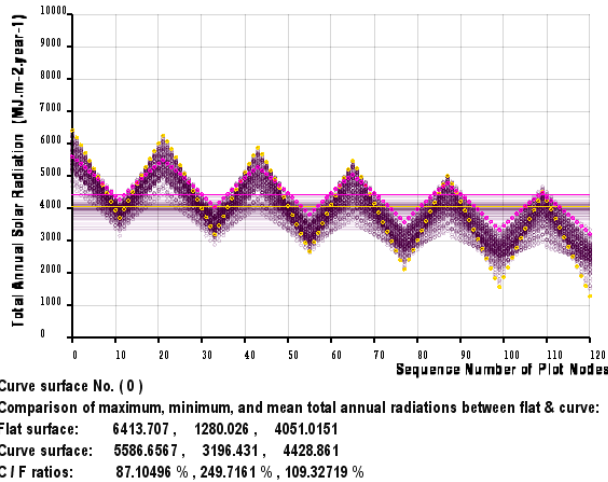


Figure 3.4.3 Comparison of solar radiation between curved surfaces and flat surface

Left: 2D plots comparison (flat surface in yellow, the optimal curved surface in purple, other individuals in grey purple); right: 3D plots comparison (flat surface in yellow and the optimal curved surface in purple) (Angle-setting: $\beta = 60^\circ \sim 90^\circ$, $\gamma = 60^\circ \sim 90^\circ$; solar condition setup: $L = 51.3^\circ N$, clear-sky mode)

In the class of Phenotype, the GA evaluation function is used for the calculation of the fitness of each individual in the population. Four objectives taken into consideration when determining the

fitness are as below:

- **Objective 1:** To maximize the number of plot nodes ($Num_{objective1}$) ahead of those of flat surface at each angle-setting ($[\beta_i] [\gamma_i]$), $E_{curve_i} > E_{flat_i}$
- **Objective 2:** To maximize the number of plot nodes ($Num_{objective2}$) which meets the expression: $|E_{curve_i} - E_{curved_mean}| / E_{curve_mean} < k$
- **Objective 3:** To maximize the mean total annual radiation, E_{curve_mean}
- **Objective 4:** To minimize the area of curved surface, S_{curve}

The above objectives are expressed as four ratios with different given weights as below:

$$\begin{aligned}
 R1 &= Num_{objective1} / Num_{total} && \text{(given Weight1)} \\
 R2 &= Num_{objective2} / Num_{total} && \text{(given Weight2)} \\
 R3 &= E_{curve_mean} / E_{flat_mean} && \text{(given Weight3)} \\
 R4 &= S_{flat} / S_{curve} && \text{(given Weight4)}
 \end{aligned}$$

Then, the fitness can be calculated by:

$$\text{Fitness} = \frac{1}{(1 + R1 \times \text{Weight1} + R2 \times \text{Weight2} + R3 \times \text{Weight3} + R4 \times \text{Weight4})} \quad \text{Formula (4)}$$

Local ranges of angle-settings where there will be more radiation on curved surface than that on flat surface can be found by means of Objective 1. The ‘stabilized coefficient’ k in the expression of Objective 2 is a key parameter to generate curved PV surfaces with the characteristic of being less sensitive to the change of angle-settings. This characteristic can be viewed as an important aspect that the curved surface exceeds the flat surface. In terms of different radiation modes, k should be given suitable values. In the preliminary testing, for instance, $k = 0.1$ is set for clear-sky mode. Objective 3 can guarantee a competitive mean total annual radiation for curved surfaces. Although the cost factor of curved PV surfaces is a secondary concern in the study, the algorithm will prefer those curved surfaces with less surface areas by Objective 4 (that suggests a less complexity with a less cost).

3.5 Preliminary testing and specifying parameters

The testing of the algorithm involved two main goals. One was to test the global efficiency of the algorithm; the other was about specifying parameters for the formal experiments in Chapter 4. In the initial testing, the angle-setting and the solar condition setup for the algorithm are as below:

Angle-setting: $\beta = 60^\circ \sim 90^\circ$, $\gamma = 60^\circ \sim 90^\circ$

Solar condition setup: $L = 51.3^\circ\text{N}$, clear-sky mode

Total number of individuals of the population: 80

The weights of each objectives and the ‘stabilized coefficient’ k were adjusted in terms of the outcomes of the experiments. The algorithm was run for three times for each set of the parameters. Through observations and comparisons, the following set of parameters has seen to be able to produce relatively satisfied results:

Parameters: $k = 0.1$, $Weight1 = 1.0$, $Weight2 = 2.5$, $Weight3 = 5.0$, $Weight4 = 0.2$

Besides, the algorithm also demonstrated a good consistency. At first, the comparisons between the result of each run were made according to the appearance, 3D and 2D radiation plot (Figure 3.5.1 and Figure 3.5.2). The appearance is displayed in a 3×3 PV array to produce the cladding effect, where the grid frames the reference position. From these illustrations, almost no macroscopic difference can be distinguished.

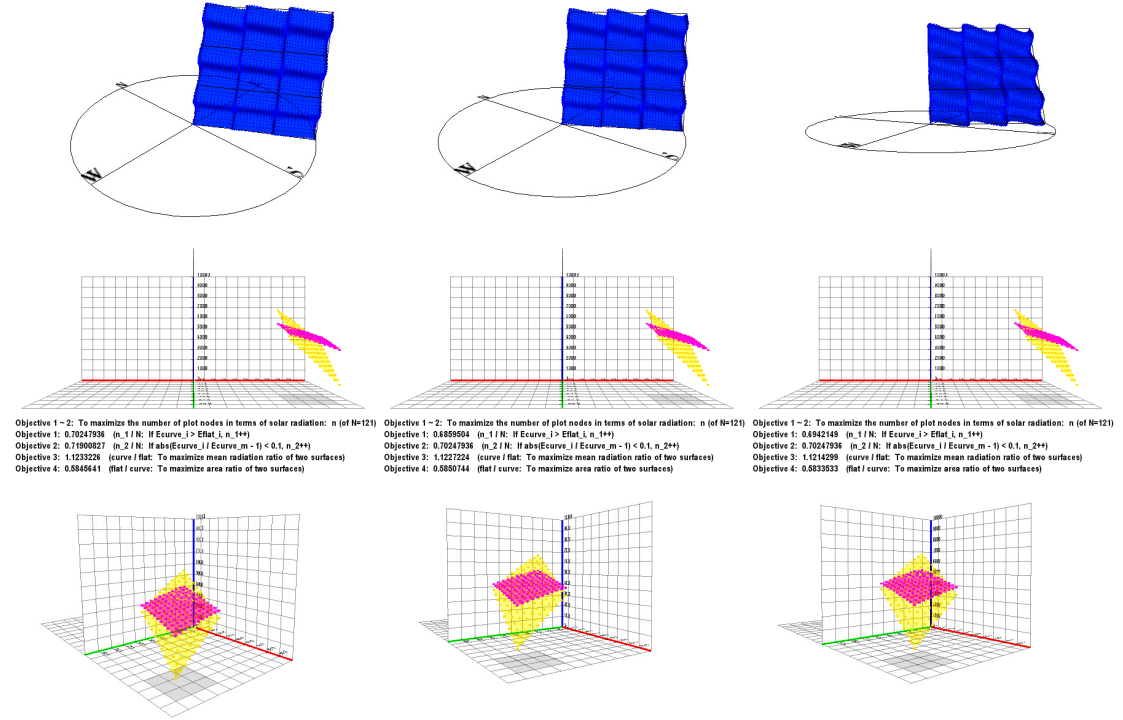


Figure 3.5.1 Comparisons of appearances and 3D radiation plots of the final optimal curved PV surfaces
Left: RUN 1; middle: RUN 2; right: RUN 3;
Top: the optimal curved PV surfaces joined in a 3×3 array; middle and bottom: 3D radiation plots

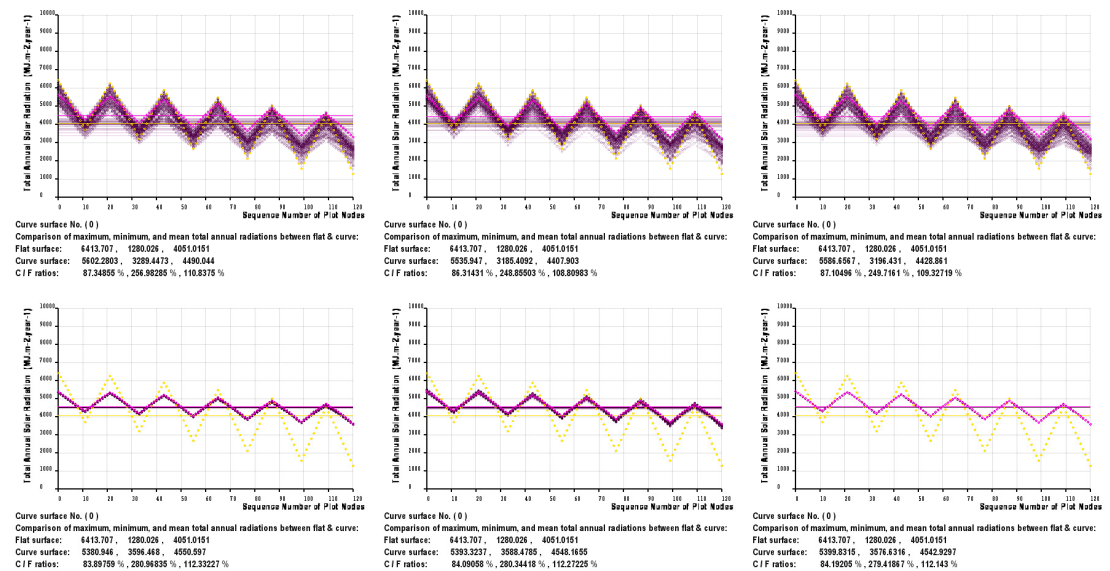


Figure 3.5.2 Comparison of 2D radiation plots between the optimal curved PV surfaces and all the others
Left: RUN 1; middle: RUN 2; right: RUN 3;
Top: 2D plots of all surfaces before GA evolution; bottom: 2D plots of all surfaces after GA convergence

Second, in order to take a conclusive insight into the results, the following data comparisons were made in respect of the maximal, minimal and mean total annual radiations of the three final optimal curved surfaces (Figure 3.5.3). The two graphs not only indicate that the three final optimal curved surfaces have almost the same radiation values and percentage values (curved/flat), but also that the mean radiations are all above that of the flat surface (more than 20%) with the decrease in the maximal radiations and increase in the minimal radiations.

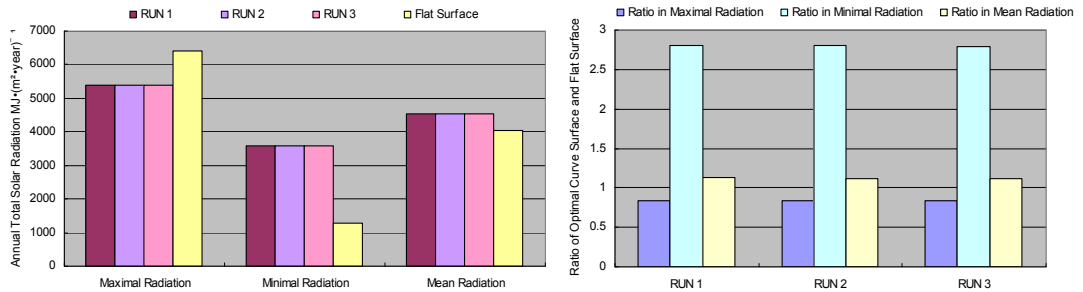


Figure 3.5.3 Comparison of maximal, minimal and mean total annual radiations

Left: numerical comparison of radiations; right: percentage comparison of curved surfaces by flat surface

The final comparisons were made according to the four objectives of the three final optimal curved surfaces (Figure 3.5.4). All the differences in the graphs are examined within small ranges of approximately only 2 per cent being acceptable for required reliability.

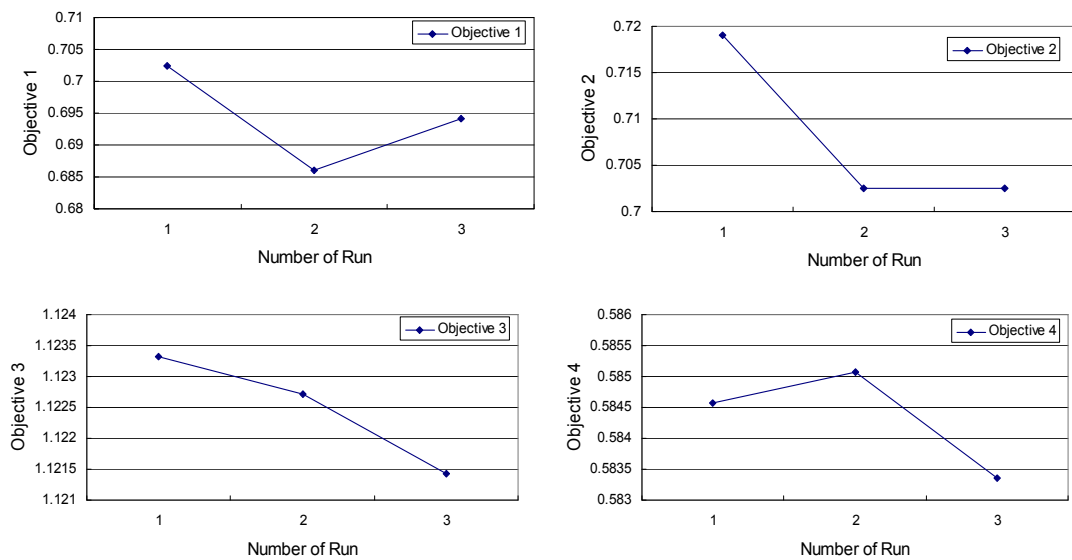


Figure 3.5.4 Comparisons of the four objectives of the final optimal curved surfaces between three-time run

Top left: Objective 1; top right: Objective 2; bottom left: Objective 3; bottom right: Objective 4

4. Testing and Results

This Chapter will start from an overview of results and then move onto more detailed analysis. At first, a single optimization process will be analyzed to gain an evolutionary perspective. Secondly, a set of experiments were carried on for the analysis according to different latitudes. Thirdly, more detailed systematic investigations will be made in terms of different divisionary scales of angle-settings. A few statements will be deduced by the findings. Finally, for the purpose of potential uses of the algorithm in practice, an adaptive approach for specifying the parameter will be discussed in order to achieve higher stabilization ratio for curved PV surfaces.

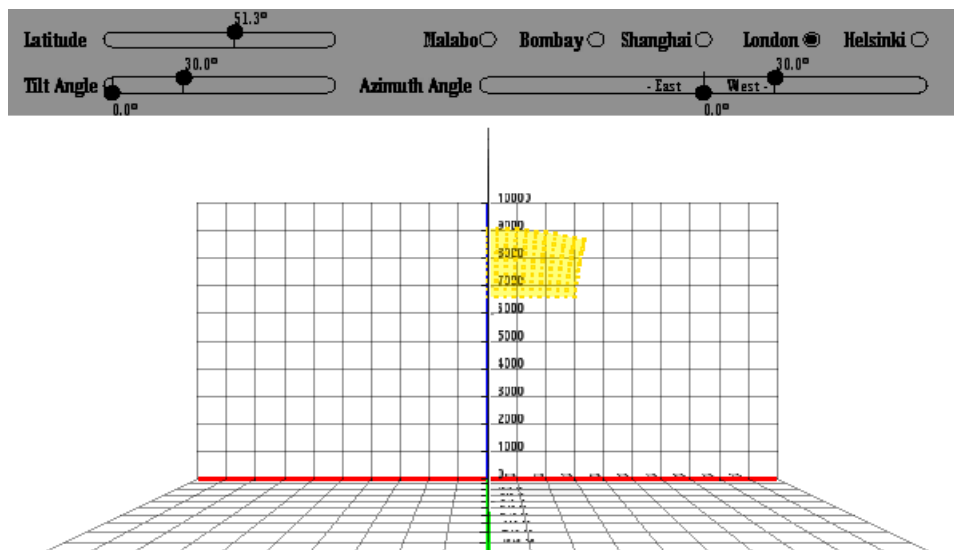
4.1 Evolutionary analysis on a single optimization process

The first formal testing is aimed at taking a thorough observation on the whole process of the optimization. The angle-settings and the solar condition setup are chosen as below (Figure 4.1.1):

Angle-setting: $\beta = 0^\circ \sim 30^\circ$, $\gamma = 0^\circ \sim 30^\circ$

Solar condition setup: $L = 51.3^\circ\text{N}$, clear-sky mode

Total number of individuals of the population: 80



Optimal tilt angle: 30.0°
Optimal azimuth angle: 0.0°
Optimal total annual radiation: 8643.406 (MJ.m-2.year-1)

Figure 4.1.1 Angle-setting and solar condition setup

(Note: the optimal angle-setting for the flat surface is showed at the bottom of the figure)

During the optimization, the data were recorded at the initial phase of GA evolution and several phases which were marked by every one hundred new generations bred by the algorithm. The general observations on each evolutionary phase can be taken in two ways. One is the overall appearance comparison in which the whole population can be displayed visually (Figure 4.1.2). The variety of individuals in the initial population was recorded (Phase 1). With the evolution

going on, as the better-fit individuals had more chances to be selected as the parents in breeding next generations and the population was upgraded in the way in which worse individuals were replaced by better ones continually, the variety continued to lose (Phase 2 and Phase 3) and convergence happened finally after the algorithm had run for a certain period of time (Phase 4).

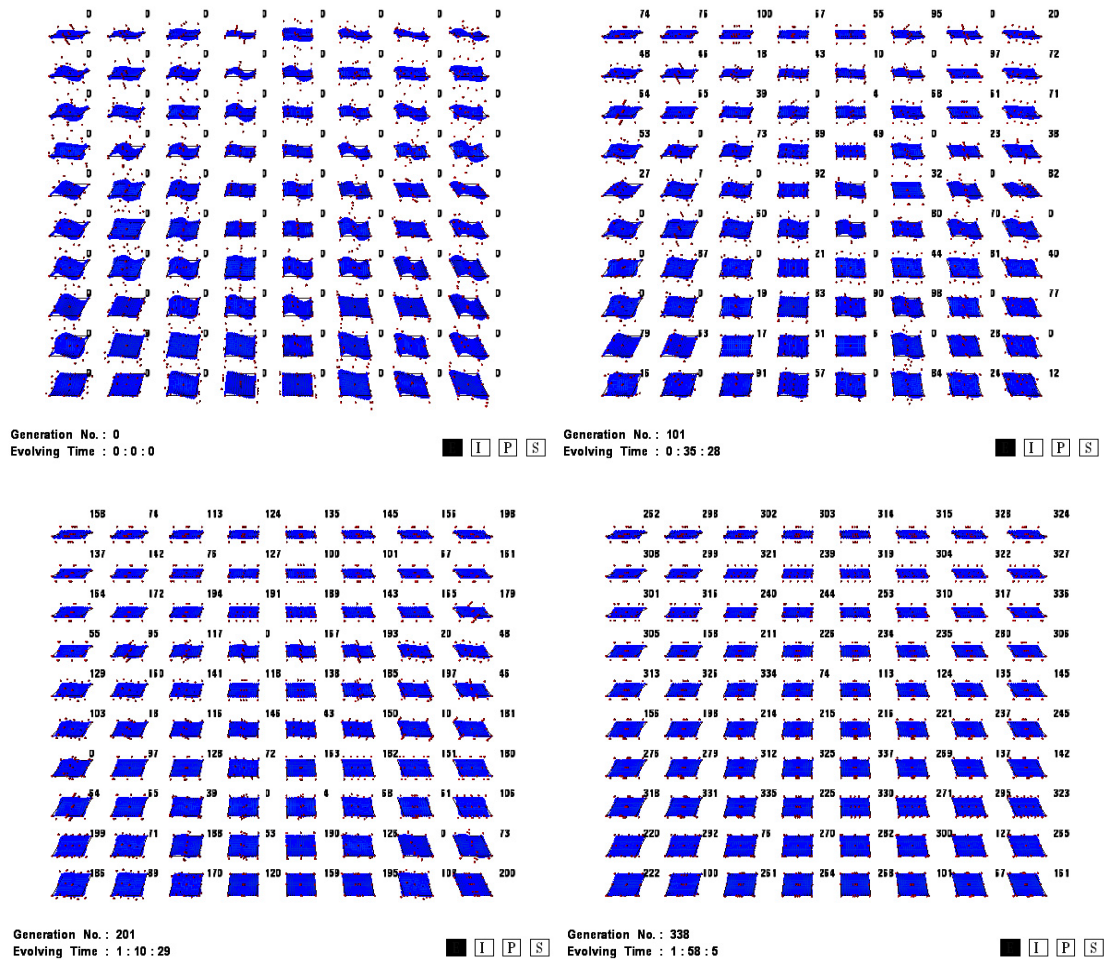
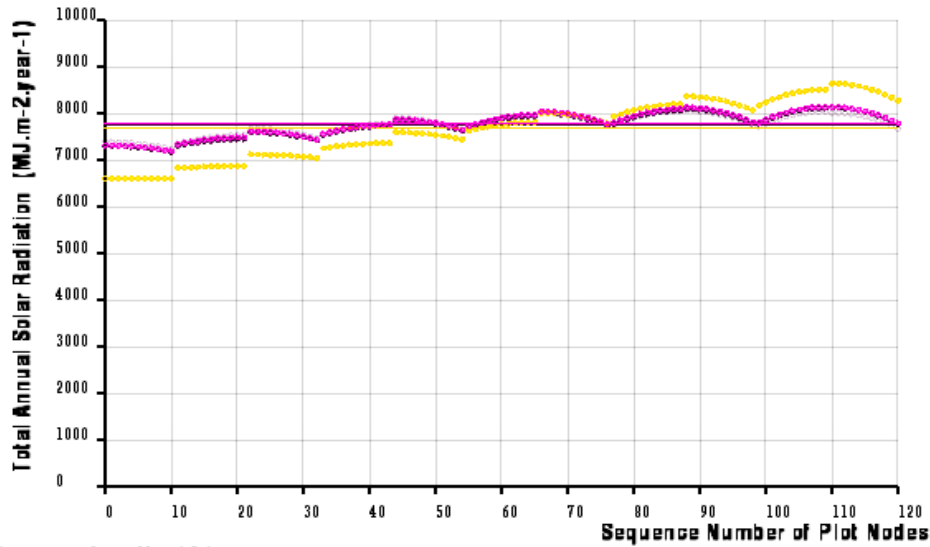
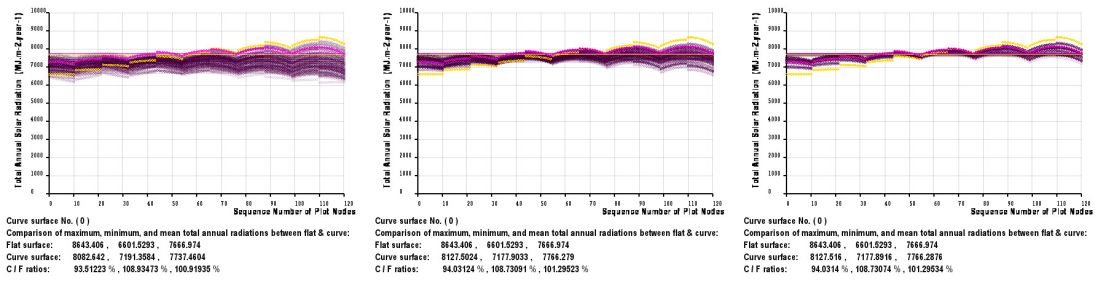


Figure 4.1.2 Overall view to the population at four evolutionary phases (80 individuals)

Top left: Phase 1 (Generation No.0); top right: Phase 2 (Generation No.101); bottom left: Phase 3 (Generation No.201); bottom right: Phase 4 (Generation No.338)

The other way of overall observation is by means of a combined diagram of 2D radiation plots, by which further comparison could be made (Figure 4.1.3). In the diagram, 3D radiation plot nodes of all curved surfaces are spread in one two-dimensional coordination system, where the optimal one (or the selected one) is in bright purple and the rest are in grey purple. The range the grey purple colour occupied displays a variety of characteristics of the generated curved surfaces in terms of their performances of solar radiation gain. The population had also seen a trend of convergence in the combined diagram of 2D radiation plots with the area of grey purple becoming narrower continually (from Phase 1 to Phase 3) and finally turning into only one spectrum (Phase 4). As mentioned in Chapter 3.2 that the yellow spectrum represents the 2D plots of the flat surface with the same solar condition setup and angle-setting of the curved surfaces being optimized, which can be compared with those purple spectrums anytime during the evolution process.



Curve surface No. (0)
Comparison of maximum, minimum, and mean total annual radiations between flat & curve:
Flat surface: 8643.406, 6601.5293, 7666.974
Curve surface: 8136.9814, 7186.7397, 7781.58
C / F ratios: 94.14091 %, 108.86478 %, 101.4948 %

Figure 4.1.3 Combined diagram of 2D radiation plots of all curved surfaces in four evolutionary phases
 Top left: phase 1 (Generation No.0); top middle: phase 2 (Generation No.101); top right: phase 3 (Generation No.101); bottom: phase 4 (Generation No. 338)

In the final phase of convergence, the following findings will be analyzed. First, the left half spectrum of the optimal curved surface is apparently ahead of that of the flat surface while the right half is below, which suggests the optimal curved surface can gain higher radiation than the flat surface when the tilt angle is less than about 15° ($\beta = 0^\circ \sim 30^\circ$) but lower radiation when the tilt angle is more than about 20°. Second, within the whole range, the mean total annual radiation (the horizontal purple line) is also enhanced slightly (about 1.5%) from that of the flat surface (the horizontal yellow line). Third, the characteristic of the overall spectrum of the optimal curved surface can be seen more ‘stable’ than that of the flat surface. This can be viewed as an important improvement of the optimal curved surface in general. All the findings may suggest that the final optimal curved PV surface generated by GA could be recommended as the alternative of the flat surface in this experiment.

The above findings can be similarly drawn from the combined diagram of 3D plots of the optimal curved surface and the flat surface (Figure 4.1.4), which provides an immediate and intuitive view to the optimization result. The values of the four objectives (at the bottom of Figure 4.1.4) can

show more accurate information. For instance, Objective 2 equals to 1.0, which means that the optimal curved surface achieved the target very well in terms of its stabilization characteristic. Also notice that there is an increase of surface area according to Objective 4 (the area ratio of two surfaces is about 92.4%), which can also be visually found in the appearance of the final optimal curved surface in the 3×3 PV array (Figure 4.1.5). The appearance shows a tiling-like effect with almost all curvatures happening on the left and right sides and none in the top and bottom. The phenomenon is believed resulted from that the algorithm was always pursuing the optimum according to the objectives in fitness, while the nature of the original radiation plot of the flat surface determined such a tiling-like direction for the optimization's going. After optimization, the optimal angle-setting of the final curved surface is $\beta = 27^\circ$ & $\gamma = 0^\circ$ which is different from the flat surface's $\beta = 30^\circ$ & $\gamma = 0^\circ$ (Figure 4.1.1).

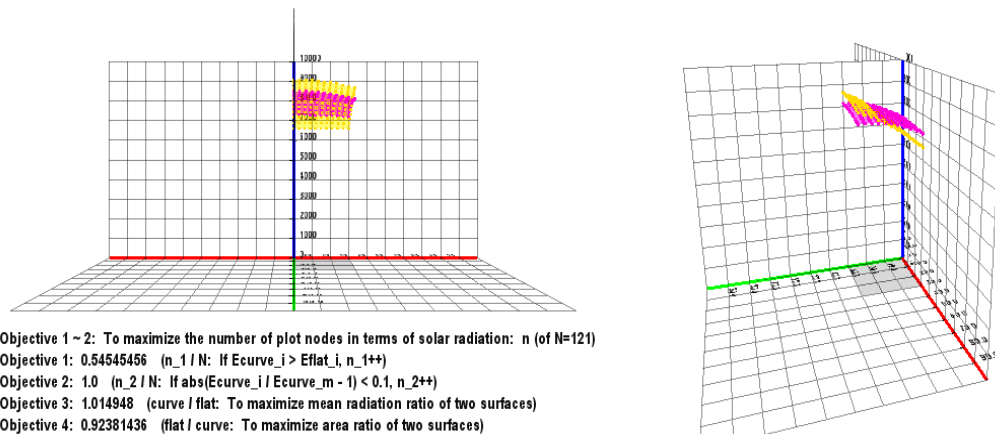
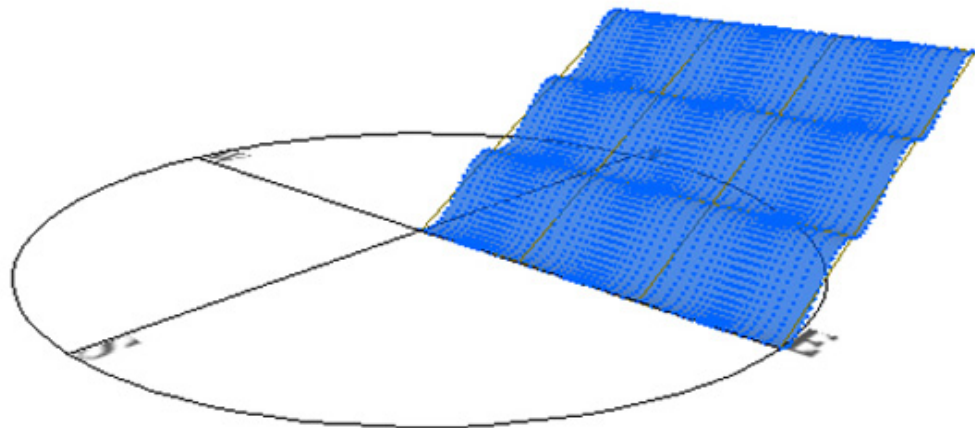


Figure 4.1.4 Combined diagram of 3D radiation plots of the optimal curved surface and the flat surface
 Left: front view; right: perspective



Curve surface No. (0) — Optimal tilt & azimuth angles: 27.0 & 0.0

Figure 4.1.5 Appearance of the optimal curved surface in a 3×3 PV array
 (Note: the grid frames show the reference position of the PV array)

In fact, there is another virtue of Genetic Algorithm that not only the optimal individuals could be chosen. As during the optimization, a variety of characteristics can be displayed by other individuals, which might also become another preference when making the decision. The data of other individuals were recorded in the two middle phases of the evolution with four individuals carefully selected for each phase (Figures are shown in Appendix II.4).

4.2 Analysis on results of different latitudes

With the experiment having been done for the latitude 51.3°N, the same experiment for different latitudes is also necessary for analysis with a global landscape. Four other latitudes were chosen carefully ranging from low to high shown as below (plus the latitude 51.3°N):

$L_1 = 3.45^\circ\text{N}$, equals to the latitude of Malabo, Equatorial Guinea

$L_2 = 18.58^\circ\text{N}$, equals to the latitude of Bombay, India

$L_3 = 31.2^\circ\text{N}$, equals to the latitude of Shanghai, China

$L_4 = 51.3^\circ\text{N}$, equals to the latitude of London, UK

$L_5 = 60.1^\circ\text{N}$, equals to the latitude of Helsinki, Finland

Angle-setting: $\beta = 0^\circ \sim 30^\circ$, $\gamma = 0^\circ \sim 30^\circ$

Solar condition setup: clear-sky mode

Total number of individuals of the population: 80

The reason for still choosing the above angle-settings is that the ranges of β and γ have seen more frequently used than other angle-settings in BIPV projects. The 3D radiation plot shows different characteristic of the flat surface for the five latitudes (Figure 4.2.1). Within the same range of angle-settings, the 3D plot displays a trend of declining down to the small tilt angle from high latitude to low latitude with also a decrease in the radiation as a whole (More details of the comparisons between the five latitudes can be found in Appendix I.5).

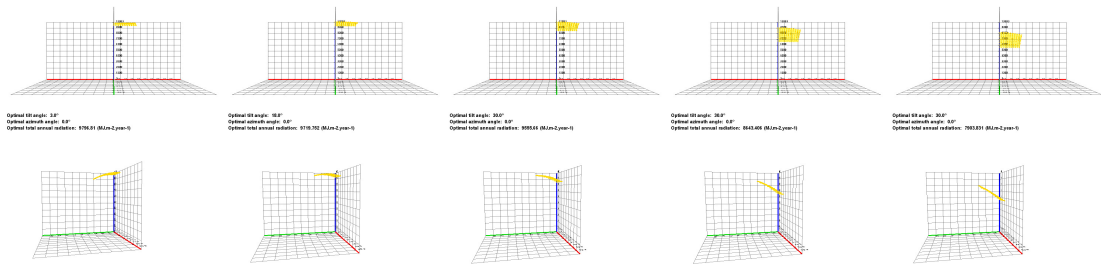


Figure 4.2.1 3D solar radiation plots of five latitudes

Latitude from left to right: 3.45°N, 18.58°N, 31.2°N, 51.3°N, 60.1°N

(Top: front view of 3D radiation plot; bottom: side view of 3D radiation plot)

From the combined 2D plots (Figure 4.2.2), some findings on the entire GA evolution process could be suggestive according to different latitudes. On one hand, in terms of the speed of convergence, the evolutionary features of GA may be classified into two types in general. The quicker convergence happened for the lower latitudes (3.45°N and 18.58°N) when the generation getting to around No.200. For the higher latitudes, the convergence might not be seen until the generation was over No.300. On the other hand, after the convergences, the final combined 2D plots also displayed two different sorts of the results. In Phase 4 for the lower latitudes 3.45°N and 18.58°N, the spectrums of the final optimal curved surfaces completely superposed that of the flat surface, which indicates that the curved ones finally converted into a flat or that no superior curved surface could be found. It is also believed that these results might be predicted from the combined 2D plots of the initial population in Phase 1. For the two lower latitudes, the ranges of grey purple color could be seen bigger than those of the higher latitudes, but all the grey purple spectrums are underneath the yellow one of the flat surface. It may suggest that in the lower

latitudes the flat surface is able to provide relative good performances for the given angle-settings. But for the other three higher latitudes, the curved alternatives were finally found. The final optimal curved surfaces generated for latitudes 31.2°N and 60.1°N had similar characteristics with that for latitude 51.3°N (Chapter 4.1), such as enhanced overall stabilization, increase of the mean total annual solar radiation and different optimal angle-setting from the flat surface.

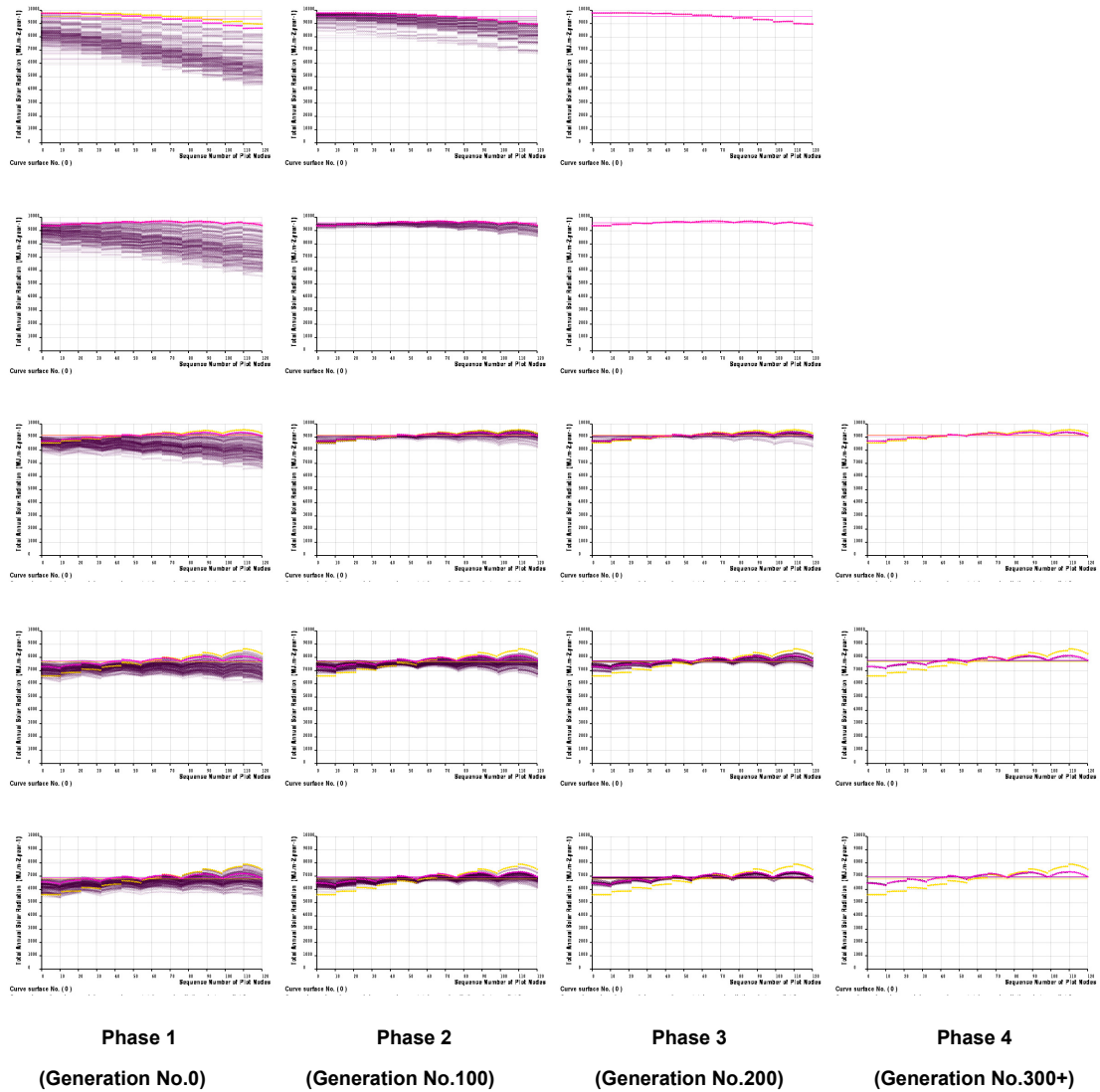


Figure 4.2.2 Evolutionary phases shown by combined 2D solar radiation plots of five latitudes
 Latitude from top to bottom: 3.45°N, 18.58°N, 31.2°N, 51.3°N, 60.1°N
 (From left to right: Phase 1; Phase 2; Phase 3; Phase 4)

The appearances of the final optimal curved surfaces also show different features, the reasons for which can be analyzed by means of their 3D radiation plots (Figure 4.2.3). First, the 3D plots of the flat surface both demonstrate good characteristics in the two lower latitudes 3.45°N and 18.58°N, so it is not surprised that the algorithm finally presented the flat surface as the optimum. Second, in the two higher latitudes 51.3°N and 60.1°N, the reasons for the appearances have been discussed in the last chapter. Only notice that the extent of curvature has seen a bit greater in latitude 60.1°N than in latitude 51.3°N. It is believed that for certain given angle-settings there is a corresponding relationship between the curvature extent and the decline degree of the 3D plots

(will be further confirmed in Chapter 4.3). Third, in the latitude 31.2°N , the curvature happened in both u and v directions which is different from the above two results. The curvature can be seen more apparent in the top and bottom sides than the other two sides. This phenomenon may suggest that the optimal curved surface is able to benefit from being contorted in both two directions (but in different degrees) in order to have a good performance in terms of solar energy gain in this case.

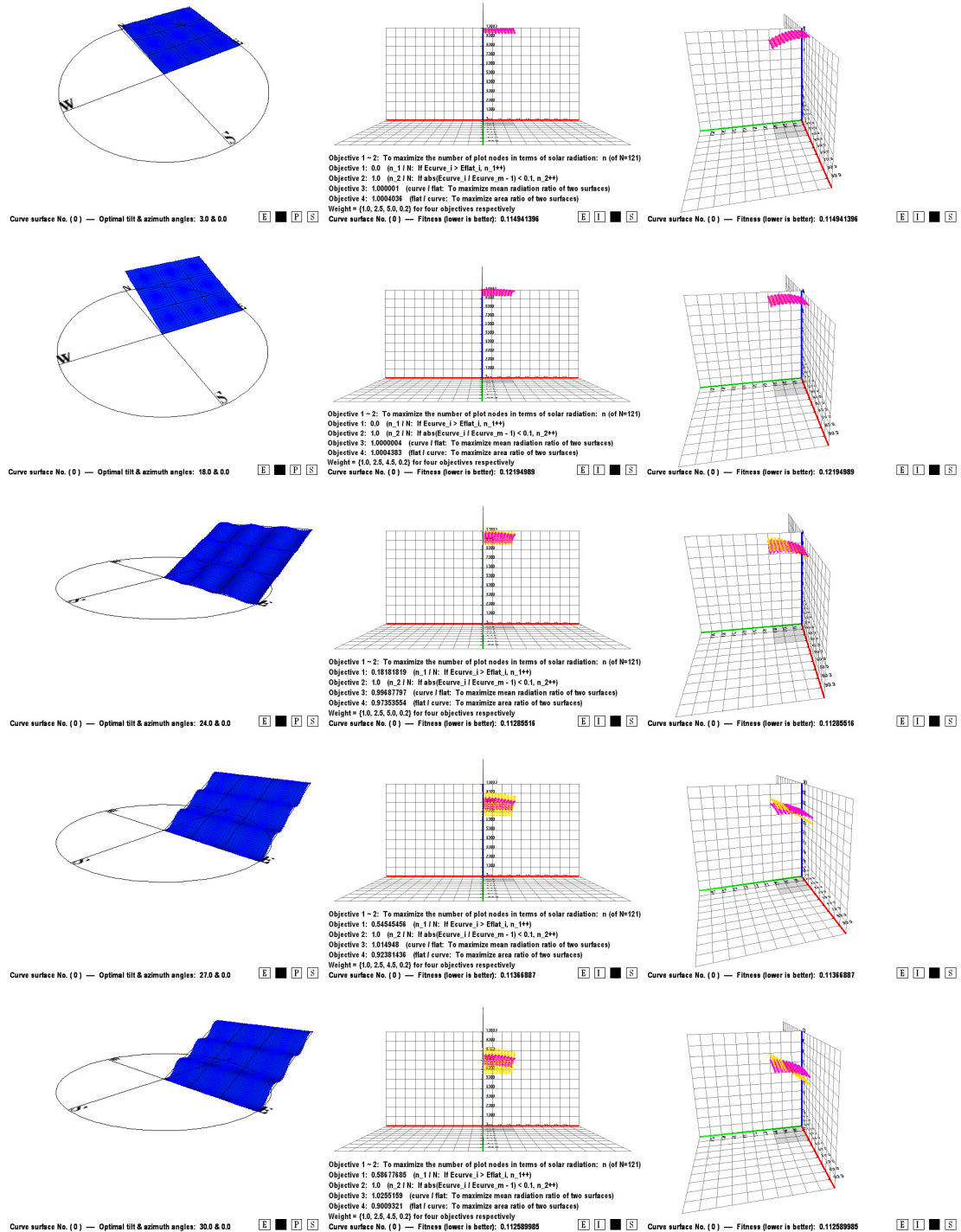


Figure 4.2.3 Results of the final optimal curved surfaces generated for five latitudes

Left: appearances in PV array; middle: front view of 3D radiation plots; right: perspectives of 3D radiation plots (Latitude from top to bottom: 3.45°N , 18.58°N , 31.2°N , 51.3°N , 60.1°N)

4.3 Analysis on results of different angle-settings

The influence on the optimization results by angle-settings of various divisionary scales will be thoroughly analyzed in this chapter. The solar condition setup for the experiments was still latitude 51.3°N and clear-sky mode. The method is that five different arbitrary scales were used for the division, ranging from the full area ($\beta = 0^\circ \sim 90^\circ$ & $\gamma = -90^\circ \sim 90^\circ$) to the small equal-sized subarea (e.g. $\beta = 0^\circ \sim 30^\circ$ & $\gamma = 0^\circ \sim 30^\circ$). The division details are as following (Figure 4.3.1):

| Division Scale / Method | Number of Subareas | Angle-settings of Subareas | Token |
|--|--------------------|---|--------------------------------|
| Full range | 1 | $\beta = 0^\circ \sim 90^\circ, \gamma = -90^\circ \sim 90^\circ$ | F* |
| Half full range | 1 | $\beta = 0^\circ \sim 90^\circ, \gamma = 0^\circ \sim 90^\circ$ | H* |
| Half full range divided by 3 equally according to β | 3 | $\beta = 0^\circ \sim 30^\circ, \gamma = 0^\circ \sim 90^\circ$ | Hβ-1 |
| | | $\beta = 30^\circ \sim 60^\circ, \gamma = 0^\circ \sim 90^\circ$ | Hβ-2* |
| | | $\beta = 60^\circ \sim 90^\circ, \gamma = 0^\circ \sim 90^\circ$ | Hβ-3 |
| Half full range divided by 3 equally according to γ | 3 | $\beta = 0^\circ \sim 90^\circ, \gamma = 0^\circ \sim 30^\circ$ | Hγ-1* |
| | | $\beta = 0^\circ \sim 90^\circ, \gamma = 30^\circ \sim 60^\circ$ | Hγ-2 |
| | | $\beta = 0^\circ \sim 90^\circ, \gamma = 60^\circ \sim 90^\circ$ | Hγ-3 |
| Half full range divided by 4 equally | 4 | $\beta = 0^\circ \sim 45^\circ, \gamma = 0^\circ \sim 45^\circ$ | H4-1 |
| | | $\beta = 0^\circ \sim 45^\circ, \gamma = 45^\circ \sim 90^\circ$ | H4-2 |
| | | $\beta = 45^\circ \sim 90^\circ, \gamma = 0^\circ \sim 45^\circ$ | H4-3* |
| | | $\beta = 45^\circ \sim 90^\circ, \gamma = 45^\circ \sim 90^\circ$ | H4-4 |
| Half full range divided by 9 equally | 9 | $\beta = 0^\circ \sim 30^\circ, \gamma = 0^\circ \sim 30^\circ$ | H9-1 |
| | | $\beta = 0^\circ \sim 30^\circ, \gamma = 30^\circ \sim 60^\circ$ | H9-2 |
| | | $\beta = 0^\circ \sim 30^\circ, \gamma = 60^\circ \sim 90^\circ$ | H9-3 |
| | | $\beta = 30^\circ \sim 60^\circ, \gamma = 0^\circ \sim 30^\circ$ | H9-4* |
| | | $\beta = 30^\circ \sim 60^\circ, \gamma = 30^\circ \sim 60^\circ$ | H9-5 |
| | | $\beta = 30^\circ \sim 60^\circ, \gamma = 60^\circ \sim 90^\circ$ | H9-6 |
| | | $\beta = 60^\circ \sim 90^\circ, \gamma = 0^\circ \sim 30^\circ$ | H9-7 |
| | | $\beta = 60^\circ \sim 90^\circ, \gamma = 30^\circ \sim 60^\circ$ | H9-8 |
| | | $\beta = 60^\circ \sim 90^\circ, \gamma = 60^\circ \sim 90^\circ$ | H9-9 |

Figure 4.3.1 Method for the divisions of angle-settings

(Note: Tokens will be used for the following figures and texts; ‘*’ means that this range of angle-setting contains the optimal angle-setting of the flat surface)

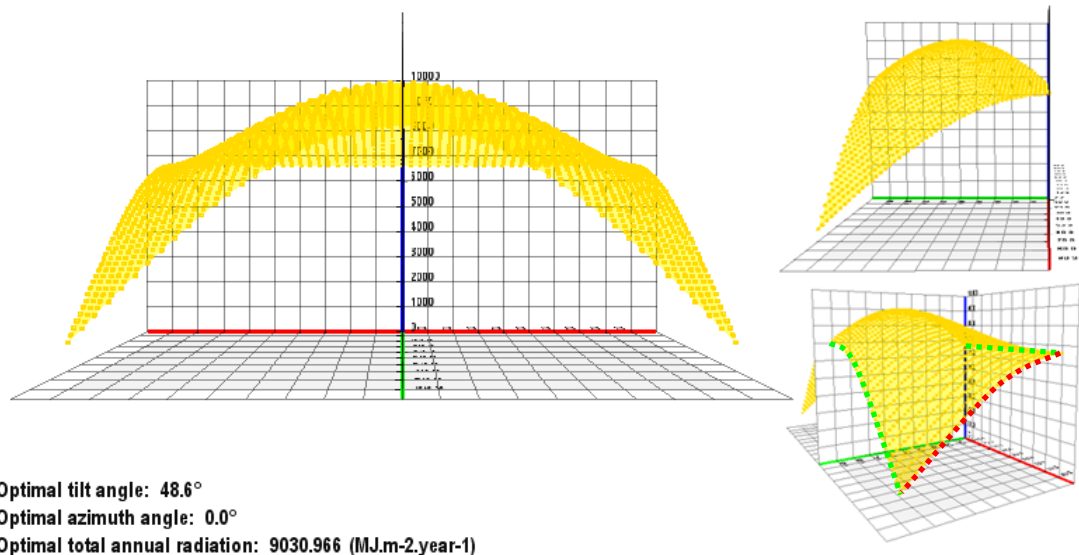


Figure 4.3.2 3D radiation plot of the flat surface for the full range of angle-settings

Left: front view; right top: side view; right bottom: perspective

(Angle-setting: $\beta = 0^\circ \sim 90^\circ, \gamma = -90^\circ \sim 90^\circ$; solar condition setup: $L = 51.3^\circ\text{N}$, clear-sky mode)

Figure 4.3.2 shows the general information of the solar radiation on the flat surface in the latitude 51.3°N . Within the full range the optimal angle-setting is $\beta = 48.6^{\circ}$ & $\gamma = 0^{\circ}$. Also notice that in the perspective view of the 3D radiation plot, the dot lines are representing the worst ranges in terms of solar radiation gain, with the two green ones for the tilt angle β and one red for the azimuth angle γ . The above information will be used as the important references for the later analysis.

The following figures (from Figure 4.3.3 to Figure 4.3.7) demonstrate general information of the final optimal curved surfaces generated for the different divisionary scales respectively (represented by Division Token). In the last chapter, the reasons why the different appearances came into being have been discussed a bit. In this chapter, deeper reasons will be investigated in terms of the optimization objectives encapsulated in the fitness definition in GA (mentioned in Chapter 3.4).

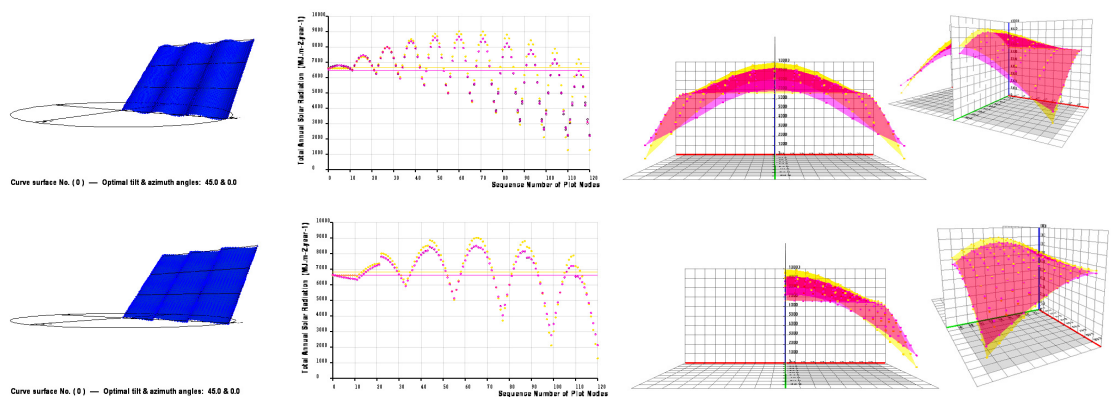


Figure 4.3.3 Final optimal curved surfaces for divisionary scales - **F** and **H**

Top: **F**; bottom: **H**

(From left to right: appearance; 2D radiation plot; front view and perspective of 3D radiation plot)

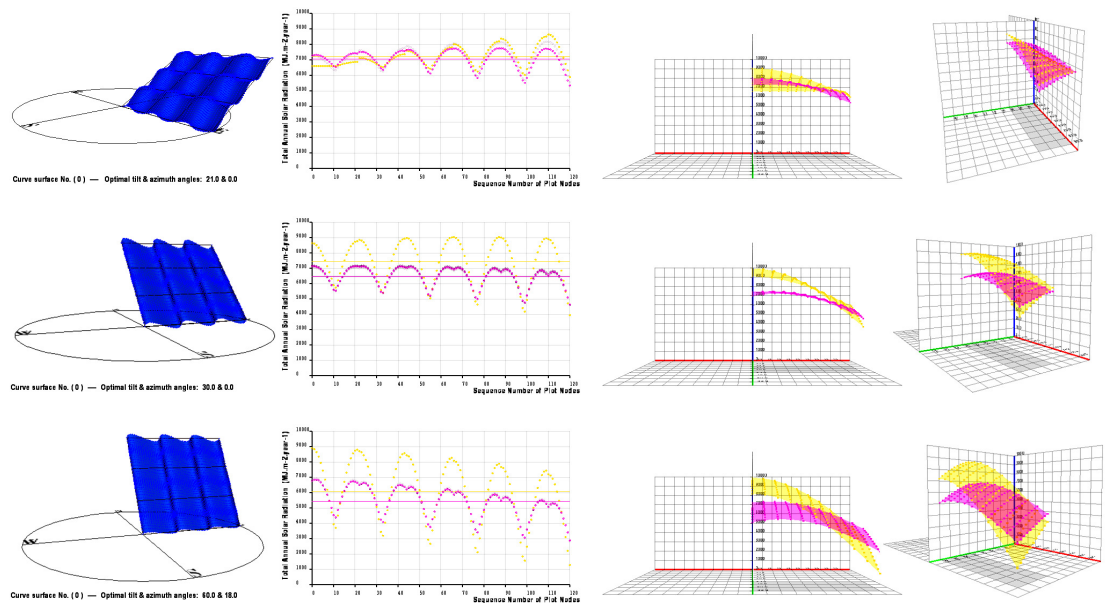


Figure 4.3.4 Final optimal curved surfaces for the set of divisionary scale - **Hβ**

From top to bottom: **Hβ-1**; **Hβ-2**; **Hβ-3**

(From left to right: appearance; 2D radiation plot; front view and perspective of 3D radiation plot)

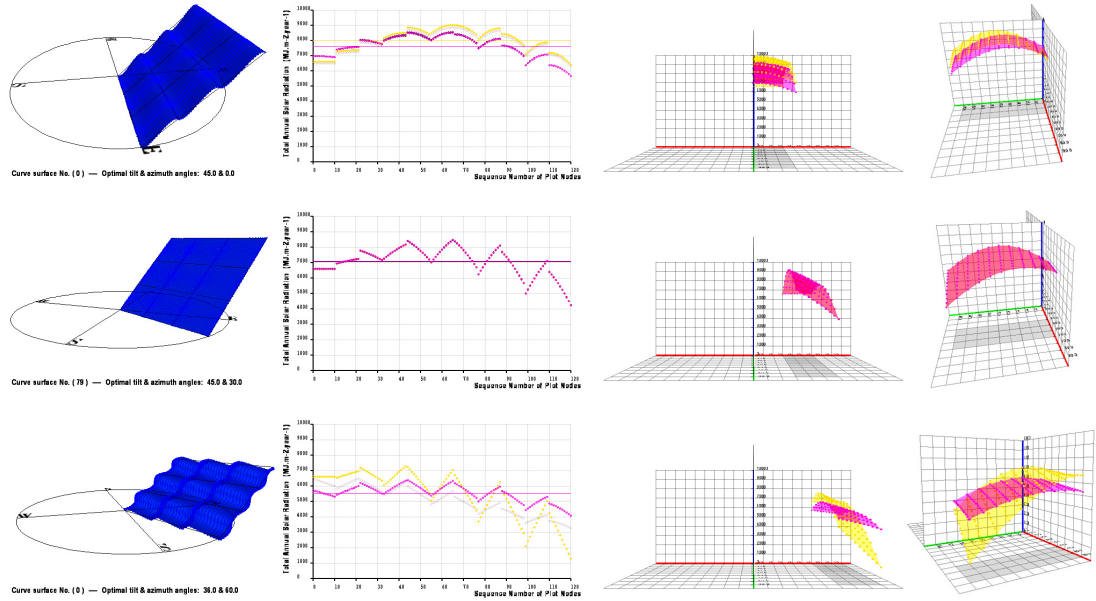


Figure 4.3.5 Final optimal curved surfaces for the set of divisionary scale - $H\gamma$

From top to bottom: $H\gamma-1$; $H\gamma-2$; $H\gamma-3$

(From left to right: appearance; 2D radiation plot; front view and perspective of 3D radiation plot)

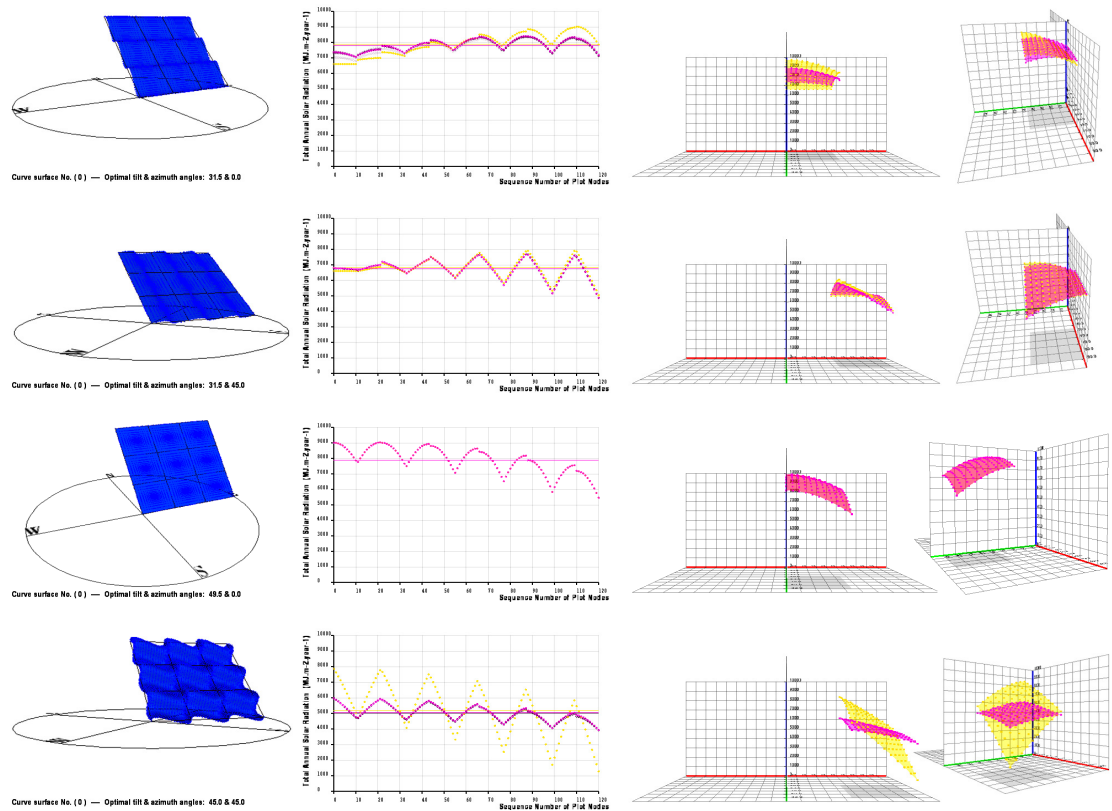


Figure 4.3.6 Final optimal curved surfaces for the set of divisionary scale - $H4$

From top to bottom: $H4-1$; $H4-2$; $H4-3$; $H4-4$

(From left to right: appearance; 2D radiation plot; front view and perspective of 3D radiation plot)

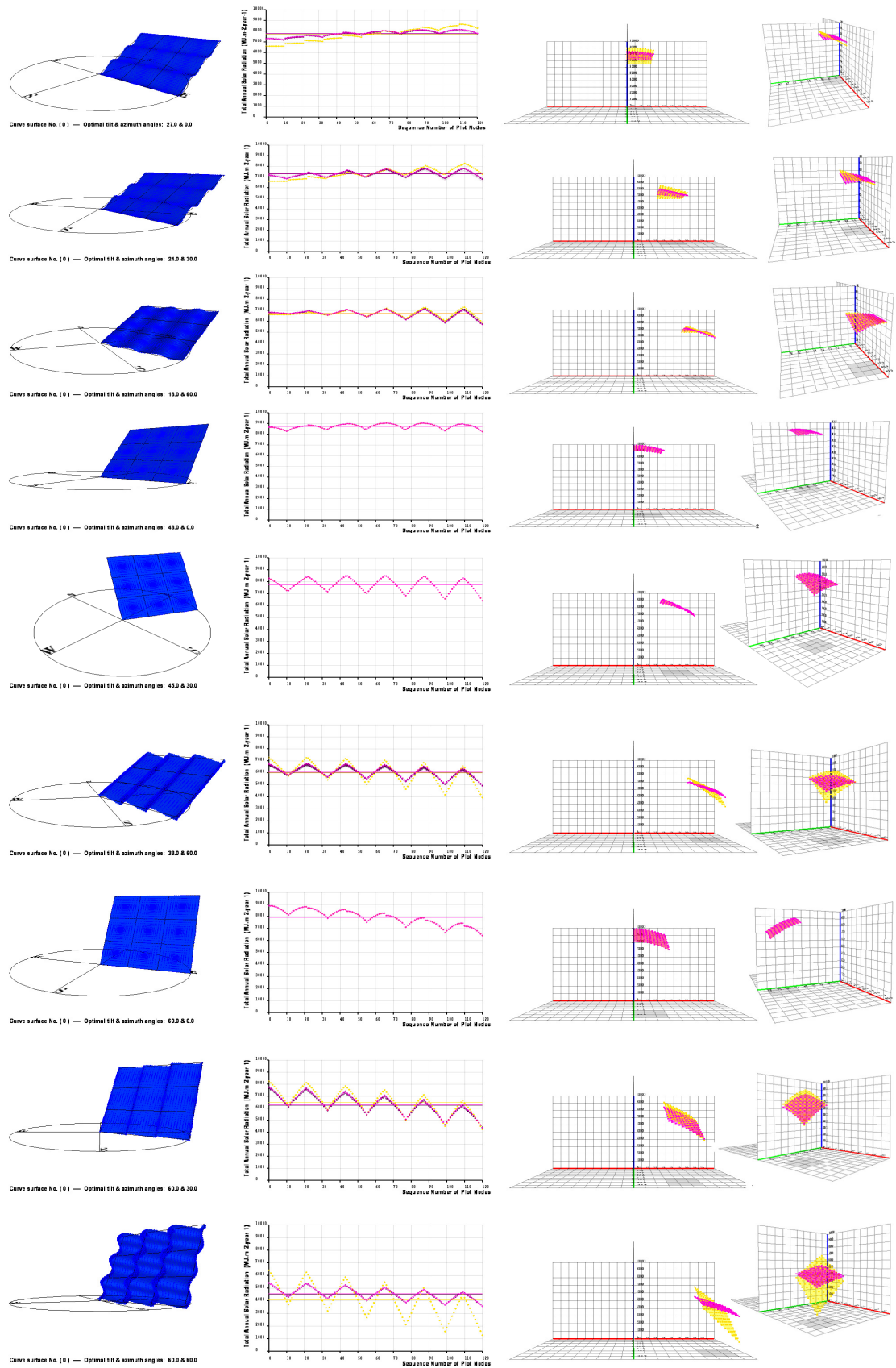


Figure 4.3.7 Final optimal curved surfaces for the set of divisionary scale - **H9**
 From top to bottom: **H9-1; H9-2; H9-3; H9-4; H9-5; H9-6; H9-7; H9-8; H9-8**
 (From left to right: appearance; 2D radiation plot; front view and perspective of 3D radiation plot)

As discussed in Chapter 3.5, Objective 2 and Objective 3 play the key roles for the algorithm to generate appropriate curved surfaces, weighted by 2.5 and 5.0 respectively. Objective 2, called the Stabilization Ratio, is used for pursuing the characteristic of less sensitivity to the change of angle-settings for curved surfaces. Objective 3 is the ratio of the mean total annual radiation of the curved surface and that of the flat surface, which is used to guarantee no much loss or to achieve an improvement in terms of solar energy gain. Hence, the results will mainly be analyzed in respect of Objective 2 and Objective 3. The stabilization ratio of the final optimal curved surface $R_{stab-curve}$ and that of the flat surface $R_{stab-flat}$, and their difference D_{stab} are recorded in the table of Figure 4.3.8, while the data involving R_{mean} (Objective 3) are shown in the table of Figure 4.3.9.

| Division Token | Stabilization Ratio of Flat Surface (Objective 2): $R_{stab-flat}$ | Stabilization Ratio of Optimal Curve Surface (Objective 2): $R_{stab-curve}$ | Difference between Curve and Flat: D_{stab} |
|----------------|--|--|---|
| F^* | 0.36363637 | 0.36363637 | 0 |
| H^* | 0.41322315 | 0.47107437 | 0.0579 |
| $H\beta-1$ | 0.74380165 | 0.87603307 | 0.1322 |
| $H\beta-2^*$ | 0.28099137 | 0.7355372 | 0.4545 |
| $H\beta-3$ | 0.1570248 | 0.41322315 | 0.2562 |
| $H\gamma-1^*$ | 0.6528926 | 0.75206614 | 0.0992 |
| $H\gamma-2$ | 0.61157024 | 0.61157024 | 0 |
| $H\gamma-3$ | 0.18181819 | 0.70247936 | 0.5207 |
| $H4-1$ | 0.6528926 | 1 | 0.3471 |
| $H4-2$ | 0.76033056 | 0.78512394 | 0.0248 |
| $H4-3^*$ | 0.6198347 | 0.6198347 | 0 |
| $H4-4$ | 0.25619835 | 0.7107438 | 0.4545 |
| $H9-1$ | 0.7107438 | 1 | 0.2893 |
| $H9-2$ | 0.9504132 | 1 | 0.0496 |
| $H9-3$ | 0.9834711 | 0.9586777 | -0.0248 |
| $H9-4^*$ | 1 | 1 | 0 |
| $H9-5$ | 0.92561984 | 0.92561984 | 0 |
| $H9-6$ | 0.5289256 | 0.8595041 | 0.3306 |
| $H9-7$ | 0.7933884 | 0.7933884 | 0 |
| $H9-8$ | 0.49586776 | 0.57024795 | 0.0744 |
| $H9-9$ | 0.24793388 | 0.70247936 | 0.4545 |

Figure 4.3.8 Table of stabilization ratio (Objective 2) of flat surface and curved surface, and their difference

| Division Token | Mean Total Annual Radiation of Flat Surface $MJ \cdot (m^2 \cdot year)^{-1}$ | Mean Total Annual Radiation of Optimal Curve Surface $MJ \cdot (m^2 \cdot year)^{-1}$ | Ratio of Curve and Flat (Objective 3): R_{mean} |
|----------------|--|---|---|
| F^* | 6635.1235 | 6454.767 | 0.9728 |
| H^* | 6809.3677 | 6626.701 | 0.9732 |
| $H\beta-1$ | 7211.1973 | 7057.7866 | 0.9787 |
| $H\beta-2^*$ | 7436.0547 | 6457.9805 | 0.8685 |
| $H\beta-3$ | 6085.6177 | 5413.957 | 0.8896 |
| $H\gamma-1^*$ | 7981.1323 | 7606.7227 | 0.9531 |
| $H\gamma-2$ | 7073.922 | 7073.9297 | 1 |
| $H\gamma-3$ | 5502.584 | 5519.11 | 1.003 |
| $H4-1$ | 7875.6455 | 7824.7554 | 0.9935 |
| $H4-2$ | 6803.982 | 6736.641 | 0.9901 |
| $H4-3^*$ | 7880.9644 | 7880.966 | 1 |
| $H4-4$ | 5170.6904 | 5049.278 | 0.9765 |
| $H9-1$ | 7666.974 | 7781.58 | 1.0149 |
| $H9-2$ | 7314.0996 | 7312.094 | 0.9997 |
| $H9-3$ | 6702.9033 | 6667.255 | 0.9947 |
| $H9-4^*$ | 8729.828 | 8720.831 | 0.999 |
| $H9-5$ | 7728.1523 | 7728.167 | 1 |
| $H9-6$ | 5993.201 | 6065.0317 | 1.012 |
| $H9-7$ | 7909.999 | 7910.016 | 1 |
| $H9-8$ | 6497.5146 | 6284.64 | 0.9672 |
| $H9-9$ | 4051.0151 | 4542.9297 | 1.1214 |

Figure 4.3.9 Table of ratio of mean total annual radiation of curved surface and that of flat surface (Objective 3)

Various estimation standards might be enacted to classify data in the above two tables. Herein, the stabilization ratio $R_{stab-curve}$ is more than 70, 80 and 90 per cent, and that the ratio R_{mean} is more than 0.98, 0.99 and 1.0 are adopted as the illustrative standards for the systematical analysis of the effects of angle-settings (Figure 4.3.10). Within the given ranges of angle-settings, if the conditional inequalities in the headers are fulfilled, then the value returns 1 else returns 0.

| Division Token | $R_{stab-curve} > 0.70$ | $R_{stab-curve} > 0.80$ | $R_{stab-curve} > 0.90$ | $R_{mean} > 0.98$ | $R_{mean} > 0.99$ | $R_{mean} > 1.0$ |
|----------------|-------------------------|-------------------------|-------------------------|-------------------|-------------------|------------------|
| F^* | 0 | 0 | 0 | 0 | 0 | 0 |
| H^* | 0 | 0 | 0 | 0 | 0 | 0 |
| $H\beta-1$ | 1 | 1 | 0 | 0 | 0 | 0 |
| $H\beta-2^*$ | 1 | 0 | 0 | 0 | 0 | 0 |
| $H\beta-3$ | 0 | 0 | 0 | 0 | 0 | 0 |
| $H\gamma-1^*$ | 1 | 0 | 0 | 0 | 0 | 0 |
| $H\gamma-2$ | 0 | 0 | 0 | 1 | 1 | 0 |
| $H\gamma-3$ | 1 | 0 | 0 | 1 | 1 | 1 |
| $H4-1$ | 1 | 1 | 1 | 1 | 1 | 0 |
| $H4-2$ | 1 | 0 | 0 | 1 | 1 | 0 |
| $H4-3^*$ | 0 | 0 | 0 | 1 | 1 | 0 |
| $H4-4$ | 1 | 0 | 0 | 0 | 0 | 0 |
| $H9-1$ | 1 | 1 | 1 | 1 | 1 | 1 |
| $H9-2$ | 1 | 1 | 1 | 1 | 1 | 0 |
| $H9-3$ | 1 | 1 | 1 | 1 | 1 | 0 |
| $H9-4^*$ | 1 | 1 | 1 | 1 | 1 | 0 |
| $H9-5$ | 1 | 1 | 1 | 1 | 1 | 0 |
| $H9-6$ | 1 | 1 | 0 | 1 | 1 | 1 |
| $H9-7$ | 1 | 0 | 0 | 1 | 1 | 0 |
| $H9-8$ | 0 | 0 | 0 | 0 | 0 | 0 |
| $H9-9$ | 1 | 0 | 0 | 1 | 1 | 1 |

Figure 4.3.10 Table of different standards used for estimation according to $R_{stab-curve}$ and R_{mean}

By means of counting the number of ‘1’ and ‘0’ for each range of angle-settings in the above table, as well as the distribution features of the two binary digits, the following tentative statements might be deduced:

- 1) The smaller divisionary scale the range of angle-settings has, the more opportunities of high qualified optimal curved surface can be achieved by the algorithm. The statement can be seen from the fact that there is a general trend in the table from the largest scale of F down to the smallest scale of the set of $H9$ that the number of ‘1’ is increasing while that of ‘0’ is reducing. Thus, for practical uses of the algorithm in BIPV, the suggestion may be given that it should be less efficient to generate the better curved alternatives for the very large-scale ranges of angle-settings (e.g. F and H), while smaller ranges are otherwise recommended.
- 2) In each different divisionary scale, the smaller the tilt angle β is, the higher $R_{stab-curve}$ could be achieved. In the table, for instance, the number of high $R_{stab-curve}$ (marked by ‘1’) can be seen more in $H\beta-1$, $H4-1$, and from $H9-1$ to $H9-6$. Note that the statement may be also proved by an opposite case that few of ‘1’ can be found in the set of $H\gamma$, which is because all angle-settings in $H\gamma$ are containing the whole range of β ($0^\circ \sim 90^\circ$).
- 3) A bigger difference (or improvement) of stabilization ratio between the curved and the flat surfaces (e.g. $D_{stab} > 0.20$) may be achieved, if the range of angle-settings contains either the worst range of β or that of γ for the flat surface, or both of the two (the worst ranges were demonstrated in Figure 4.3.2). In the table of Figure 4.3.8, the case of $D_{stab} > 0.20$ can be seen in the following angle-settings: $H\beta-2$, $H\beta-3$, $H\gamma-3$, $H4-1$, $H4-4$, $H9-1$, $H9-6$ and $H9-9$.
- 4) The opportunity of achieving high mean total annual radiation on the curved surface might be

increased, if the range of angle-settings contains either the worst range of β or that of γ for the flat surface, or both of the two. The examples can be seen in the table, such as **H γ -3**, **H9-1**, **H9-6** and **H9-9**. Thus, the algorithm can be more effective for the angle-settings in which the flat surface is at a disadvantage.

- 5) For the range that contains the optimal angle-setting of the flat surface (marked by '*'), the mean total annual radiation on the curved surface cannot exceed that of the flat surface. For such ranges, the main target for the algorithm would become pursuing higher stabilization ratio $R_{stab-curve}$ and trying to make R_{mean} as close as 1.0 (see $R_{mean} > 0.98$ and $R_{mean} > 0.99$).
- 6) For the case with the range between what mentioned in 4) and 5), the mean total annual radiation of the optimal curved surface may also be mediate between those of 4) and 5).

4.4 Analysis on importance of stabilization coefficient

As analyzed before, the most important advantage of curved surfaces should be that, for certain given angle-settings, they may be able to hold higher stabilization characteristic than flat surfaces. The stabilization ratio $R_{stab-curve}$ has been defined in Chapter 3.3 which is also shown here again:

$$R_{stab-curve} = \text{Numobjective2} / \text{Numtotal}$$

Objective 2: To maximize the number of plot nodes (Numobjective2) which meets the expression:
 $|E_{curve_i} - E_{curve_mean}| / E_{curve_mean} < k$

If to compare Objective 2 with the other three objectives, it is easy to realize that the other objectives can all be viewed as independent parameters so that there is no need to define them by extra parameters, while Objective 2 is affected by another parameter 'k' that must be arbitrarily given before the algorithm runs. As mentioned in Chapter 3.4, the value of Stabilization Coefficient k (equals to 0.1) was obtained by the preliminary testing and thus was used as a constant later. However, for two reasons, it is believed necessary to reinterrogate it.

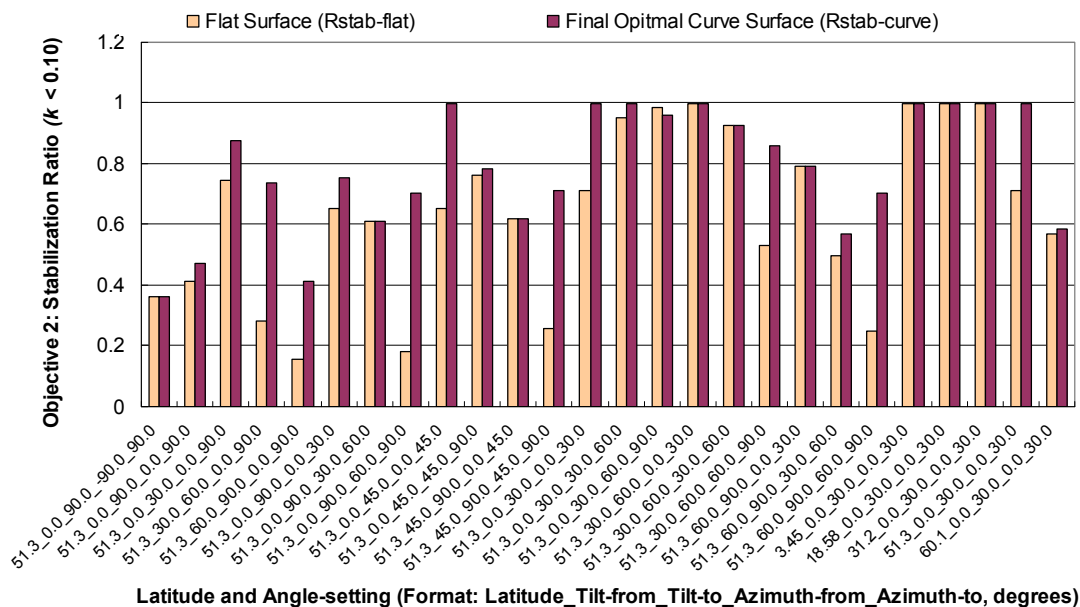


Figure 4.4.1 Comparison of Stabilization Ratio between flat surface and final optimal surface

On one hand, through further observations on Objective 2 of all the formal experiments (Figure

4.4.1), some of the results tend to suggest that k might not be a globe constant fit for all situations. On the other hand, since there are different solar condition setups (e.g. cloud-cover mode) and a variety of possibilities of angle-settings in the practice (must be beyond the testing in the paper), the approach for specifying the parameter ‘ k ’ should be also adaptive for these usages .

From the comparison between $R_{stab-curve}$ and $R_{stab-flat}$ for all experiments being listed in the graph, we may notice that only a few $R_{stab-curve}$ are greatly enhanced from $R_{stab-flat}$ (e.g. $D_{stab} = R_{stab-curve} - R_{stab-flat} \geq 20\%$), for which the stabilization coefficient k might be regarded as appropriate ($k = 0.1$). So the results of those cases are picked up for the further investigations. Through analysis, it is found necessary to set a watershed (50%) for $R_{stab-flat}$ by which different sets of data could be distinguished and put into the following two tables (Figure 4.4.2 and Figure 4.4.3).

| Latitude and Angle-setting | $R_{stab-flat} \geq 50\%$ | $D_{stab} \geq 20\%$ | $k / R_{stab-flat}$ |
|----------------------------|---------------------------|----------------------|---------------------|
| 51.3 0.0 45.0 0.0 45.0 | 0.6528926 | 0.3471074 | 0.153164548 |
| 51.3 0.0 30.0 0.0 30.0 | 0.7107438 | 0.2892562 | 0.140697675 |
| 51.3 30.0 60.0 60.0 90.0 | 0.5289256 | 0.3305785 | 0.189062507 |
| 51.3 0.0 30.0 0.0 30.0 | 0.7107438 | 0.2892562 | 0.140697675 |

Figure 4.4.2 Table of selected results in terms of $R_{stab-flat} \geq 50\%$ and $D_{stab} \geq 20\%$

| Latitude and Angle-setting | $R_{stab-flat} < 50\%$ | $D_{stab} \geq 20\%$ | $k / R_{stab-flat}$ |
|----------------------------|------------------------|----------------------|---------------------|
| 51.3 60.0 90.0 0.0 90.0 | 0.1570248 | 0.25619835 | 0.636842078 |
| 51.3 30.0 60.0 0.0 90.0 | 0.28099137 | 0.45454583 | 0.355882816 |
| 51.3 0.0 90.0 60.0 90.0 | 0.18181819 | 0.52066117 | 0.549999975 |
| 51.3 45.0 90.0 45.0 90.0 | 0.25619835 | 0.45454545 | 0.390322576 |
| 51.3 60.0 90.0 60.0 90.0 | 0.24793388 | 0.45454548 | 0.40333334 |

Figure 4.4.3 Table of selected results in terms of $R_{stab-flat} < 50\%$ and $D_{stab} \geq 20\%$

The reason why $R_{stab-flat}$ is chosen is that it can be calculated when solar condition setup and angle-settings are given. A relation is established between k and $R_{stab-flat}$ by means of their quotient. As seen in the above two tables, the average quotient for each column of “ $k / R_{stab-flat}$ ” can be calculated respectively:

$$Q_1 = \sum (k / R_{stab-flat}) = 0.156 \quad (\text{for } R_{stab-flat} \geq 50\%, \text{ Figure 4.4.2})$$

$$Q_2 = \sum (k / R_{stab-flat}) = 0.467 \quad (\text{for } R_{stab-flat} < 50\%, \text{ Figure 4.4.3})$$

$$k_1 = Q_1 \times R_{stab-flat-floor} = 0.156 \times 50\% = 0.078 \approx 0.08 \quad (R_{stab-flat} \geq 50\%)$$

$$k_2 = Q_2 \times R_{stab-flat-ceiling} = 0.467 \times 50\% = 0.2335 \approx 0.2 \quad (R_{stab-flat} < 50\%)$$

The approach can be described as following:

- $R_{stab-flat}$ is firstly calculated by $k = 0.1$
- If $R_{stab-flat} \geq 50\%$, then $k = R_{stab-flat} \times k_1$ ($k_1 = 0.08$) Formula (5)
- If $R_{stab-flat} < 50\%$, then $k = R_{stab-flat} \times k_2$ ($k_2 = 0.2$) Formula (6)

Thus, according to the range that $R_{stab-flat}$ belongs to, one of the two figures (k_1 or k_2) might be used as the first try to define the stabilization coefficient k . But notice that the simple method is still tentative and its validity needs to be verified by more experiments and further investigations.

5. Demonstrations for Practical Application

5.1 Review of ECN-building (NL) and new target

In this chapter, a real example is chosen dealing with a famous BIPV building—General Laboratory of the Netherlands Energy Research Foundation ECN, located in Petten, Netherland. The building was built in 1963, with total floor area of 3530 m². Because of the poor performance of energy consumption and non-ideal comfort for users, the building was renewed from year 1997 to 2001 (Henk F. Kaan and Tjerk Reijenga, 1998). The renewal constructions concerned by this paper mainly involved a PV-integrated façade shading system for the building No.31 and a PV-integrated roof shading system for its continuation building No.42 (Figure 5.1.1).



Figure 5.1.1 General Laboratory of the Netherlands Energy Research Foundation ECN
Left: perspectives; middle: illustration of ECN-building; right: under renew construction
Source: <http://www.bear.nl/>; pictures by Het Houtblad

The improvement of the building's performance by the innovative construction might be beyond the discussion of this paper. Herein, we may be more interested in if we can use the algorithm to generate appropriate curved PV surfaces for the above renewal constructions as the alternative of the flat ones being used in the building. Through the analysis it can be found that in both of the PV shading systems mentioned above, there is a fact that the PV arrays of them have to face a same problem of nonuniform tilt angles (Figure 5.1.2 and Figure 5.1.3).



Figure 5.1.2 PV-integrated façade shading system for ECN-building No.31
Source: <http://www.bear.nl/>; pictures by Het Houtblad



Figure 5.1.3 PV-integrated roof shading system for ECN-building No.42
Source: <http://www.bear.nl/>; pictures by Het Houtblad

On one hand, according to Kaan and Reijenga, the façade PV shading system for the building No.31 was designed as a special movable system in term of a balance between the cost and solar energy gain. The system can be altered between the optimal position to the sun with the tilt angle 37° and the horizontal position for users to have a good outside view. The lamella in the horizontal position can automatically change back to 37° after an interval of 20 minutes (Figure 5.1.2). On the other hand, it is seen more apparently in the building No.42 that the roof with PV shading system follows a curvature way as a quarter of the circle in which each row of the glass PV panels has a different tilt angle (Figure 5.1.3). As mentioned in Chapter 1, the change of angle-settings in PV array suffers a problem of conflict with the goal of achieving stable electric power generated by the BIPV system. Thus, it is believed feasible to take experiments on the two BIPV systems of the ECN-building, not only in order to have a practical experience of the usage of the algorithm, but more importantly, to investigate that in what degrees the curved PV panels can be competitive with the flat ones. The target will emphasize on achieving a relatively stable solar radiation on all curved panels for the given range of angle-settings and at the same time having a good performance of mean total annual solar energy gain for each PV shading system.

In order to fulfill the target, the experiments will use the real solar condition setup of the site and refer as close as possible to the available data of other construction criteria used for the flat PV panels in the renewal construction. The latitude of Petten is 52.8°N and the building leans from the north to the west with an angle of 10° . Cloud-cover mode rather than clear-sky mode is considered more suitable. The average monthly bright sunshine durations of Petten are calculated by the recorded data of a decade (Figure 5.1.4). The 3D radiation plot for the full range of angle-settings can be displayed in the cloud-cover mode by the programme (Figure 5.1.5).

| Year | Jan | Feb | Mar | Apr | May | Jun | Jul | Aug | Sep | Oct | Nov | Dec |
|---------|------|------|------|------|------|------|------|------|------|------|-----|------|
| 2007 | 2 | 2 | 6.9 | 9.3 | 6.9 | 6.4 | 7 | 7.6 | 4.7 | 4.1 | 2.2 | 2.1 |
| 2006 | 2.5 | 2.1 | 5.3 | 6 | 7.5 | 8.4 | 10.5 | 5.3 | 6.1 | 3.3 | 2.7 | 1.4 |
| 2005 | 3.3 | 3.4 | 4.2 | 6.7 | 7.9 | 8.3 | 4.6 | 6.4 | 6.6 | 5.2 | 2.2 | 2.4 |
| 2004 | 1.5 | 2.9 | 5 | 6.6 | 6.9 | 6.3 | 7.6 | 6.2 | 6.4 | 4.6 | 1.9 | 2 |
| 2003 | 2.5 | 5.2 | 5.8 | 8.3 | 8.1 | 8.5 | 8.5 | 8 | 7.2 | 5.5 | 2.4 | 2 |
| 2002 | 2.7 | 4.4 | 5.5 | 6.6 | 7.3 | 7.2 | 6.8 | 6.2 | 5.6 | 3.8 | 2.3 | 1.2 |
| 2001 | 2.4 | 3.9 | 3.1 | 6.2 | 9.7 | 8.4 | 8.5 | 6.6 | 4.1 | 4.3 | 2.2 | 2.4 |
| 2000 | 2.1 | 3.8 | 3.6 | 5.6 | 8.3 | 7.4 | 4.5 | 7.5 | 3.9 | 2.6 | 1.5 | 2.1 |
| 1999 | 2.6 | 4.8 | 3.4 | 7.1 | 8.7 | 8.7 | 8.2 | 6 | 5.4 | 4.3 | 2.6 | 1.9 |
| 1998 | 2.3 | 4.1 | 3.4 | 4.5 | 7.2 | 5.9 | 5.6 | 6.9 | 3.4 | 2.4 | 3 | 2.1 |
| Average | 2.39 | 3.66 | 4.62 | 6.69 | 7.85 | 7.55 | 7.18 | 6.67 | 5.34 | 4.01 | 2.3 | 1.96 |

Figure 5.1.4 Data of monthly bright sunshine duration of Petten

Source: World Radiation Data Center (<http://wrdc.mgo.rssi.ru>)

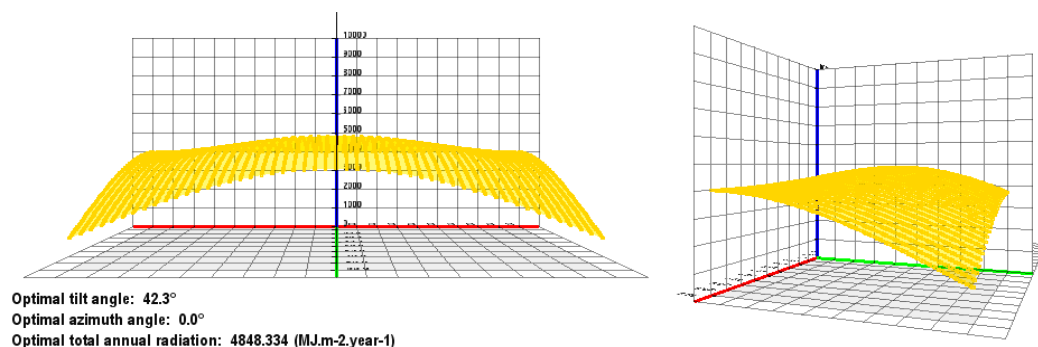


Figure 5.1.5 3D radiation plot of full range of angle-settings in Petten

(Angle-setting: $\beta = 0^\circ \sim 90^\circ$, $\gamma = -90^\circ \sim 90^\circ$; solar condition setup: $L = 52.8^\circ\text{N}$, cloud-cover mode)

5.2 Optimization of curved PV lamellas for façade shading system

In the PV façade shading system of the building No.31, the size of the lamella is about 840 mm wide, 3000 mm long with three standard multi-crystalline PV modules on the front part (Kaan and Reijenga, 1998). Thus the input data being known so far for the experiment are as below:

Solar condition setup: $L = 52.8^\circ\text{N}$, cloud-cover mode

Angel setting: $\beta = 0^\circ \sim 37^\circ$, $\gamma = -10^\circ$

Size of single PV module: 800 mm \times 1000 mm

As shown by Figure 5.2.1, there are 51 plot nodes used for the 3D and 2D radiation plots. In the 2D radiation plot, it can be found that the mean total annual radiation is approximate $4,500 \text{ MJ} \cdot (\text{m}^2 \cdot \text{year})^{-1}$, and the spectrum fluctuates greatly between the two ends with about 20 per cent difference. By using Formula (5) in Chapter 4.4, the stabilization coefficient k was adjusted to 0.075, by which $R_{stab-flat} = 0.86$ is achieved for the stabilization ratio of the flat PV surface.

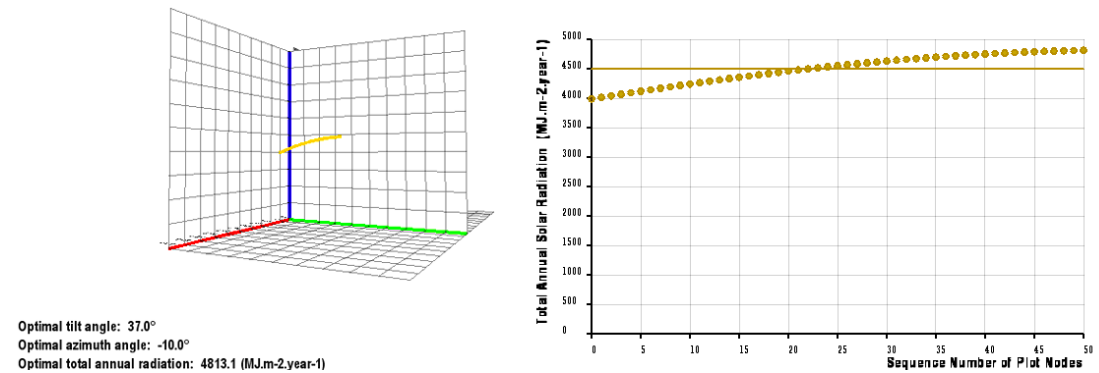


Figure 5.2.1 3D and 2D radiation plots of flat surface

Left: side view of 3D radiation plot; right: 2D radiation plot

The two combined diagrams of 2D radiation plots (Figure 5.2.2) show a variety of characteristics of the initial population in the first phase and the final optimal curved surface in the final phase after GA convergence. The radiation spectrums of the curved surfaces in purple can be compared with that of the flat surface in brown. The optimization results are satisfied that the stabilization ratio was improved by 14 per cent ($R_{stab-curve} = 1.0$) and the mean total annual radiation had only a very small decrease by 0.35 per cent ($R_{mean} = 99.65\%$) while comparing with the flat surface.

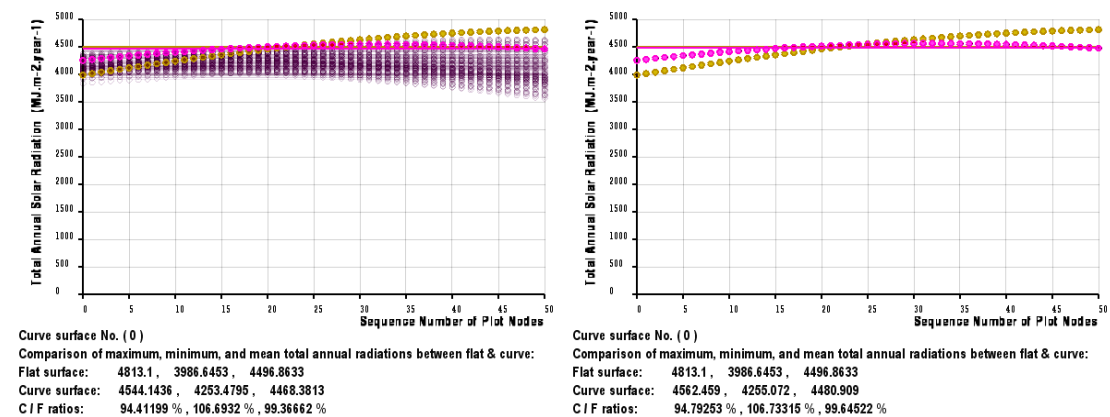


Figure 5.2.2 Combined diagrams of 2D radiation plots

Left: initial phase; right: final phase (bottom: comparison data between optimal curved surface and flat surface)

As the method of specifying k is still in trial, other three parallel experiments have also been done with k equaling to 0.025, 0.05 and 0.1 respectively. Through comparisons (Figure 5.2.3), it is found that the first one ($k = 0.025$) has slight higher $R_{stab-curve}$ but the R_{mean} is reduced to 98%, and the other two have similar $R_{stab-curve}$ but neither R_{mean} of them (99.64% and 99.54%) can be over that for $k = 0.075$. So it is affirmed that the result by $k = 0.075$ is the optimal one so far.

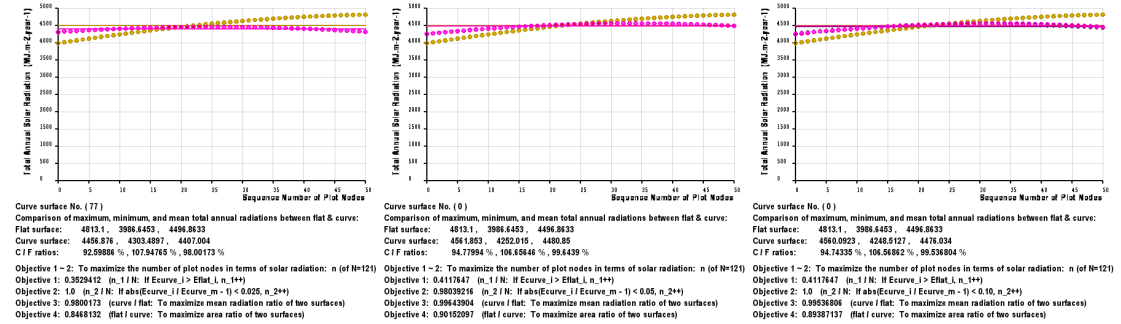


Figure 5.2.3 Combined diagrams of 2D radiation plots of other three parallel experiments

Left: $k = 0.025$; middle: $k = 0.05$; right: $k = 0.1$

Figure 5.2.3 shows the appearance of the final optimal curved PV surface displayed in a 3×3 array (maybe only 3×1 array needed) and the 3D radiation plot and its objective data of the fitness, by which further comparisons could be made between the curved PV lamella and the flat one.

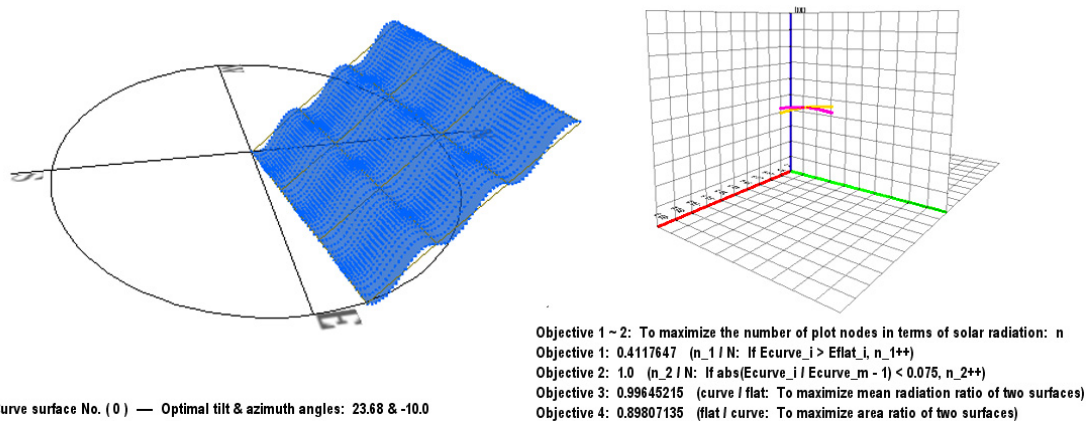


Figure 5.2.4 Appearance and 3D radiation plot of final optimal curved surface

Left: a 3×3 array with the optimal angle-setting; right: 3D radiation plot with the objectives' data at the bottom

First, the overall stabilization characteristic of the curved PV lamella is greatly improved when comparing with that of the flat one ($R_{stab-curve} = 1.0 > R_{stab-flat} = 0.86$) for the given range of angle-settings. Second, the mean total annual radiation ($\text{MJ} \cdot (\text{m}^2 \cdot \text{year})^{-1}$) of the curved lamella has a very small decrease of only 0.35% from that of the flat one, which is believed acceptable. Third, from the fact that Objective 1 equals to about 0.41 (Figure 5.2.3 - right) and the combined diagram of 2D plots in the final phase (Figure 5.2.2 - right), it is revealed that when the tilt angle is within the first 2/5 range, the mean total annual radiation of the curved PV lamella always exceeds that of the flat one. While considering that the 2/5 range ($0^\circ \sim 15^\circ$) also holds positions of the lamella for the good outside view, this improvement seems suggest that there are more potential good positions can be used besides the two predefined positions (0° and 37°) if using curved PV

lamellas. Finally, the optimal tilt angle for the curved PV lamella is 23.68° ($< 37^\circ$), which indicates that the optimal position also provides a broader outside view. The overall improvements suggest that, if configured by the optimal curved PV lamellas, the PV façade shading system may be used as flexibly as other normal movable façade shading systems, since there will be no much reduction of solar gain when the tilt angle of the lamellas is freely changed by users. The final effect of the curved PV façade shading system is produced by Processing modeling (Figure 5.2.5).

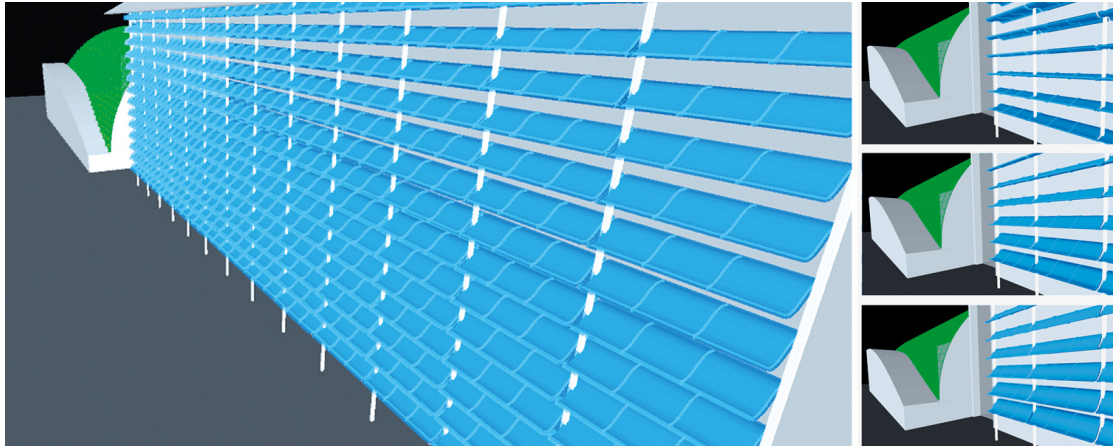


Figure 5.2.5 Façade shading system configured by curved PV lamellas

Left: Overall perspective; right top: tilt angle 0° ; right middle: tilt angle 23.68° ; right bottom: tilt angle 37°

A reasonable claim is that the curved lamella may be not really competitive to the flat one, perhaps for two main reasons. On one hand, the curved lamella has been actually bended so as to ‘borrow’ other angles to balance the solar gain. On the other hand, just because of the bending, the curved lamella will hide more view than the flat one in any position (tilt angle). Admittedly, it can be partially explained as that way. However, another option might be found to release the query if micro curved module/cell could also be technically feasible (e.g. by thin-film, Figure 5.2.6).

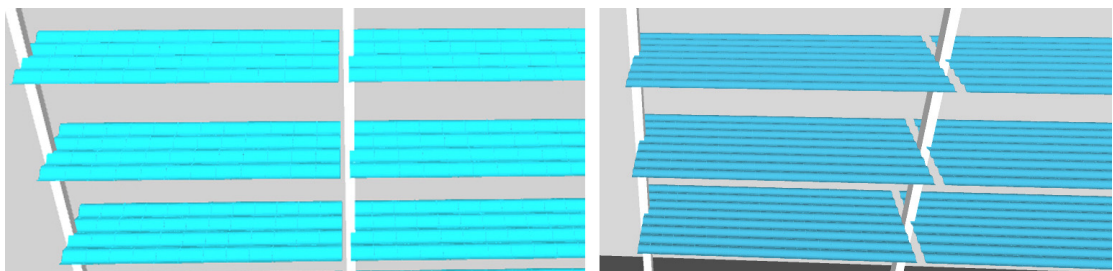


Figure 5.2.6 Hypothesis of micro curved PV module/cell

Left: 12×4 array; right: 24×8 array

5.3 Optimization of curved PV glass panels for roof shading system

Figure 5.3.1 demonstrates the geometry of the PV roof shading system of the building No.42. The range of tilt angle of PV panels is from 1.875° to 58.125° with an increase of 3.75° for each step of the total sixteen rows of PV panels. So the available input data for the experiment are as below:

Solar condition setup: $L = 52.8^\circ\text{N}$, cloud-cover mode

Angel setting: $\beta = 1.875^\circ \sim 58.125^\circ$, $\gamma = -10^\circ$

Size of single PV panel: 750 mm \times 1500 mm (reckoning)

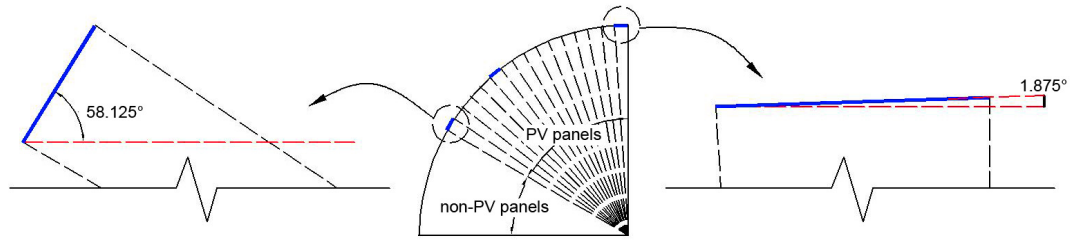


Figure 5.3.1 Geometry of PV roof shading system of building No.42

Left: the biggest tilt angle of PV panels; middle: overall geometry; right: the smallest tilt angle of PV panels

(Note: because of the inadequacy of data, 16 rows of PV panels used might be a simplified version of the real roof)

Different from the experiment in the last chapter in which the lamella's angle is free to change, all the tilt angles have already been known in this case, so several adjustments were made before the experiment. First, only sixteen nodes are needed for computing the 3D and 2D radiation plots, representing the tilt angle of each row of PV panels. Objective 1 is canceled (weighted by zero), since each row of PV panels has the equal importance—no need to examine the performance of partial range. Third, the stabilization coefficient k is assigned to 0.07 by the preliminary testing, by which the stabilization ratio of the flat panel $R_{stab-flat}$ is calculated to be 0.875. Similarly, the combined diagrams of 2D radiation plots of the initial phase and the final phase are shown in Figure 5.3.2, and the appearance of the final optimal curved surface and its 3D radiation plot are shown in Figure 5.3.3, with the relative data at the bottom of each figure.

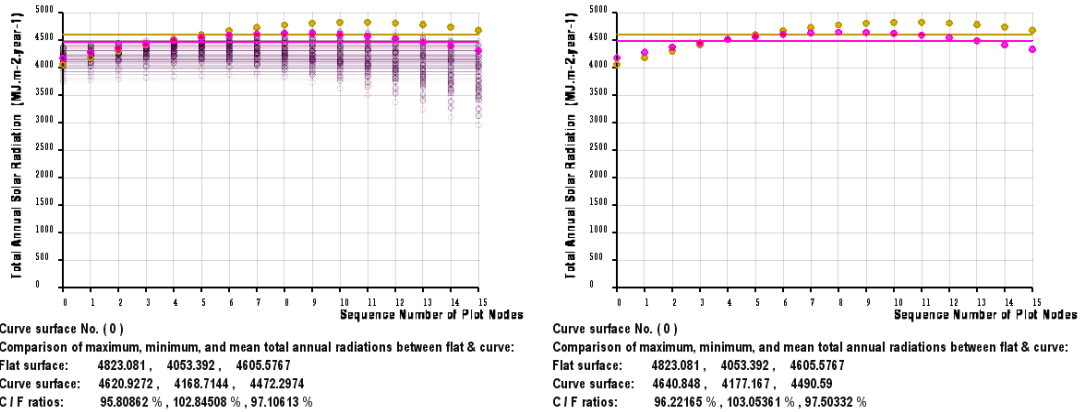


Figure 5.3.2 Combined diagrams of 2D radiation plots

Left: initial phase; right: final phase (bottom: comparison data between optimal curved surface and flat surface)

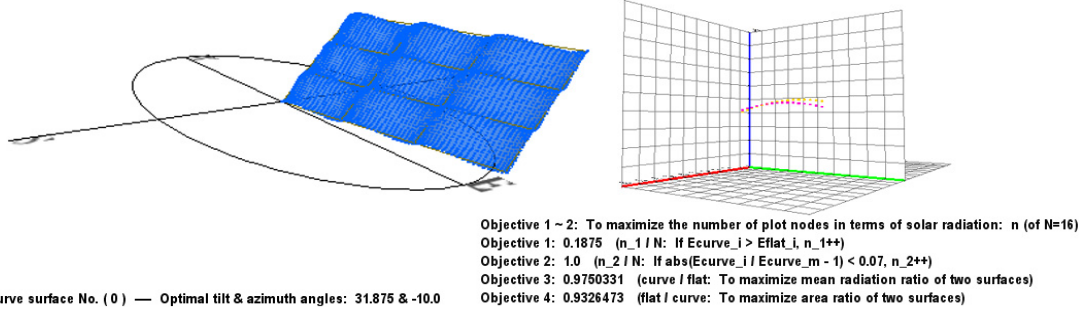


Figure 5.3.3 Appearance and 3D radiation plot of final optimal curved surface

Left: a 3×3 array with the optimal angle-setting; right: 3D radiation plot with the objectives' data at the bottom

(Note: objective 1 being weighted by 0 has no effect on the result)

In terms of the result, following comparisons could be made. First, through the optimization, $R_{stab-curve}$ of the final curved PV panel is improved to 1.0 which has 12.5 per cent increase from $R_{stab-flat}$. Second, there is about 2.5 per cent decrease in the mean total annual radiation comparing with that of the flat panel. It is believed that this reduction was a necessary compromise for achieving a better stabilization characteristic. Third, in terms of the distribution of the solar gain, the biggest difference between 16 rows of the flat PV panel is $769.7 \text{ MJ} \cdot (\text{m}^2 \cdot \text{year})^{-1}$ —about 17% of the mean total, while after optimization that of the curved PV panel is much improved by being reduced to $463.6 \text{ MJ} \cdot (\text{m}^2 \cdot \text{year})^{-1}$ —less than 10% of the mean total.

By means of Processing modeling, the roof and the overall effect of the ECN-building integrated curved PV shading systems can be seen roughly from the following figures.

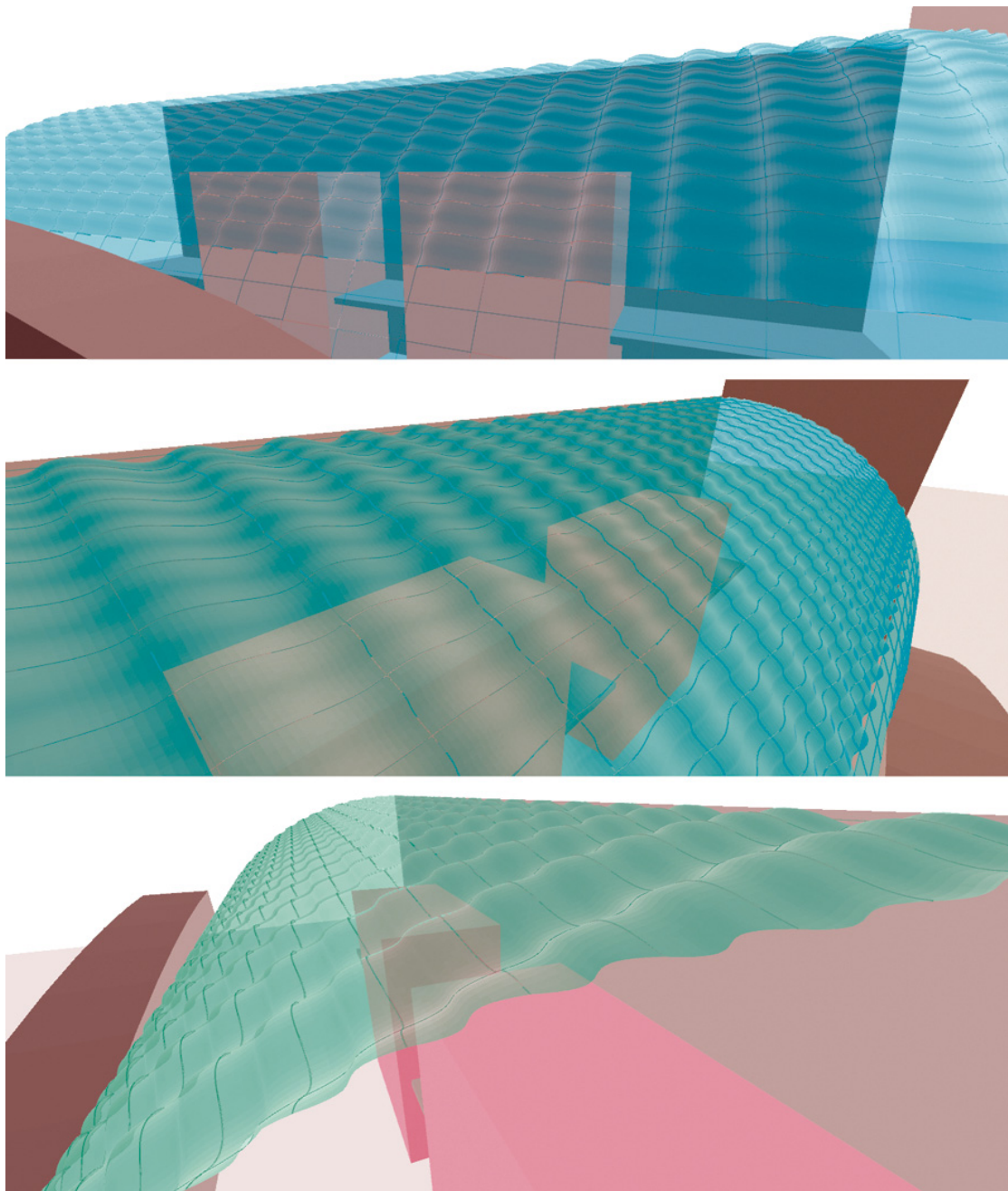


Figure 5.3.4 Close views of the roof integrated curved PV panels of the building No.42

Thus, although the mean total annual radiation is a bit lower than that of the flat PV panel, the curved one has other two apparent advantages. On one hand, much even distribution of the solar radiation on the whole PV area of the roof could guarantee a stable high efficiency of the BIPV system. On the other hand, the curved PV panels can produce a special and attractive appearance for the building, which is incomparable by other traditional flat PV panels.

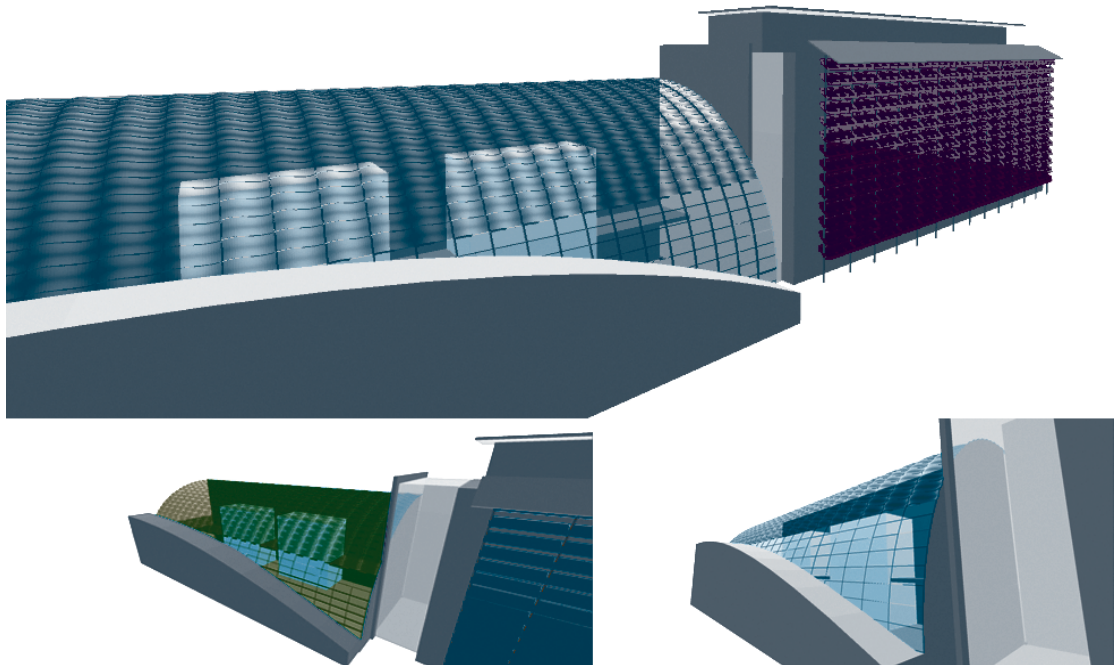


Figure 5.3.5 Perspectives of the ECN-building integrated curved PV shading systems



Figure 5.3.6 Indoor view of the roof integrated curved PV of the building No.42

6. Discussion

6.1 Overview of findings

Through experiments, the paper presented the characteristics of curved surfaces in terms of the solar energy gain, which can be compared with flat surfaces for the same angle-settings and solar condition setups. Basically, three types of comparison results can be classified according to the stabilization ratio and the mean total annual radiation—two key objectives for the optimization. The first type is that both of the two objectives of the optimal curved surface are better than those of the flat surface. This usually happens when the flat surface may not have good performances for the given angle-settings (e.g. the worst ranges in its solar radiation plot). As the second, the stabilization ratio of the curved surface can much more exceed that of the flat surface, but it must accompany more or less decrease in the mean total annual radiation. For these cases, the main goal of the algorithm would become pursuing the mean total annual radiation as close as that of the flat surface while keeping a high stabilization ratio for the curved surface. For the third, neither of the two objectives is able to competitive with that of the flat surface so that the algorithm cannot find better alternatives and would present the flat surface as the final optimal surface in the end.

In fact, all of the above results can be viewed as useful findings when using the algorithm for practical appliances. On one hand, a big problem for popularizing BIPV projects is that many buildings (or their parts) may have not good positions to the sun so that traditionally they are not considered suitable to be integrated with photovoltaics, such as vertical walls, roofs without the optimal angles, or architectural components with nonuniform angle-settings, etc. A promising solution for them might be found in the first type of results in which curved surfaces can overcome those disadvantages of the traditional flat surfaces in terms of the usage of solar energy. On the other hand, for the second type of results in which if the curved surface and the flat surface have similar performances or each of them has its own strong points, the curved surface will still be a competitive alternative of the flat one, as its merits may be appreciated by designers according to other architectural considerations. Finally, even if the third type of results comes out, it suggests that the flat surface can be proved as the optimal architectural surface to be recommended for the given situations. However, the opportunities to adopt curved PV surfaces should not be limited by those mentioned, since there are a wide spread of design purposes in practical BIPV projects.

In order to gain desirable results for practical usages, several suggestive findings were also deduced. First, the divisional scale of angle-settings will have a great relation with the quality of the optimization outcomes. The smaller scale is chosen, the more accurate and better results can be achieved. Second, specifying an appropriate stabilization coefficient k is a determinant factor for the success of the optimization. The tentative approach for it has been discussed in Chapter 4.4 and demonstratedly used in Chapter 5, but it still needs further investigations in respect of the validity. Third, proper radiation mode (e.g. clear-sky or cloud-cover mode) must be predisposed for the different purposes of solar energy usages. For instance, clear-sky mode might be more suitable for the projects in which the direct solar radiation is more important, while cloud-cover mode can provide a global consideration of the solar radiation according to a specific location.

6.2 Critical assessment

The proposed method for the optimization is derived from two challenges. One challenge is computing the solar radiation on curved surfaces; solving cladding problem for curved surfaces is the other. However, taking into account the cladding issue is a compromise to the fact that almost all current PV modules are following such a way in which they have to be designed in certain engineering standards in order to be manufactured in batches and therefore easily fabricated for buildings. But it also becomes a constraint for exploring more possibilities for curved PV surfaces for the architecture. In another word, without that constraint (or say that PV panels can be used as easily as and be adapted as conveniently as, the ordinary panels for buildings), more attractive curved surfaces could be generated by the algorithm for the use of an entire roof or other architectural elements rather than only a piece of curved surface being prepared for cladding.

Although the paper presents a heuristic approach for designs of BIPV projects, critically there are still two technical difficulties for adapting curved PV surfaces. First, the future of curved PV surfaces might rely on the development of thin-film technology rather than the traditionally well developed technologies for crystalline silicon. Second, another promising feasibility of curved PV surfaces is to be used in much smaller scales so that some required morphological structures or appearances of building elements could be reserved. But it is only an assumption yet determined by whether micro PV modules could be invented and proved suitable in the future. Besides, there will also be other challenges for integrating curved PV surfaces into buildings similarly with those unordinary forms being problems for architectural designs and engineering constructions.

As the time constraint, an unsolved problem for the algorithm is that some generated curved surfaces can produce self shading problem. The relative data, like the mean total annual radiation, might be overestimated as a result. Two possible approaches are conceived for the problem. First, an additional algorithm could be used for the shading calculation. But this algorithm might be very complex and involved large computing effort. Another easier solution could be a posterior procedure to examine in what degree the overestimation will be and thus a correctional approach can be taken. The development of the algorithm is one important aspect of further investigations.

6.3 Further investigations

The study of curved PV surfaces is still a complicated thesis, yet many future works are needed to equip the proposed method with augmented practical values for BIPV appliances. Besides those having been mentioned, there are still several aspects that require to be further explored:

- For various usages, relative objectives need be reexamined or adjusted for the algorithm.
- Cladding problems of curved PV surfaces should more refer to the requirements of BIPV system engineering so as to generate suitable PV elements at the initial phase of the design.
- The algorithm can affiliate other variables in order to serve as the augmented tools in solving different design issues, such as also taking into account other architectural or structural problems.
- More practical criterions can be explored while making comparisons for the optimization.
- Another strong potential of the algorithm can be explored for developing special curved PV tiles so that a wide range of residence buildings could benefit from.

7. Conclusions

The paper addressed the problem of the optimization of curved PV surfaces that may become the alternatives of the traditional flat PV surfaces for BIPV projects. The proposed method involved three parts: a simulation module of solar radiation, an evolutionary algorithm for optimization, and a comparison module for analysis. The simulation module has been developed for computing solar radiation on curved surfaces by means of adapted Hay's anisotropic radiation model. The cladding problem of curved PV modules was geometrically solved that may serve as the starting point for practical links with architectural and engineering considerations. Genetic Algorithm was chosen as the main algorithm for the optimization, in which different objectives were encompassed by the fitness definition for the GA population. A systematical approach for the comparisons between the curved and flat surfaces in terms of solar energy gain was established, involving specific 3D and 2D radiation plots and related data recording system. Through a set of testing, the capacities of the algorithm were confirmed and a series of findings were discussed and concluded so as to be used as references for the demonstration project and other practical appliances.

The outcomes of the proposed method are believed suggestive for facilitating the development of Building-integrated Photovoltaics—a new domain combined architecture and renewable energy. The practical credits of the method can be seen in the selected demonstration appliance of the algorithm. But more values are actually latent because of the content constraint of the paper, which may be further explored by means of augmented power of the algorithm and a number of practical feedbacks from the BIPV projects the method would be applied into in the future.

As one of the emergent and promising futures of the architecture, the present BIPV domain is still suffering from the difficulties of how to bring together the thoughts and the efforts of architects, PV engineers and other related specialists. The study in the paper therefore presented such a consideration and serves as a preliminary exploration in this field. In this context, the generated curved PV surfaces may not only enhance the richness of the usage of solar products, but more importantly, provide a heuristic approach for the purpose of bridging the gap between those different areas. It is believed worthy to have more researchers and architects endow themselves into the development of BIPV, to keep going the relative investigations, and to strengthen further the collaborations among them.

Appendix I

I.1 Solar radiation models

In the optimization of curved PV surfaces in terms of better usage of solar energy, an accurate model is firstly necessary for the measurement of solar radiations on them. Over the years, several empirical models have been proposed, tested and revised for achieving more efficient predication of solar energy for applications in various practical fields. Those models can be classified into two types: the Isotropic Model and the Anisotropic Model (e.g. Klucher's and Hey's anisotropic models). Despite the two types of models both might under-estimate or over-estimate solar radiation in certain seasons of a year, the anisotropic models are definitely superior than the isotropic model and recommended for predicting solar radiation on inclined surfaces (C.C.Y.MA and M.IQBAL, 1982). Relative comparisons have also been made by different authors continually. Among them, Salem Nijmeh and Rustom Mamlook (1999) in their experiments reported that, the isotropic model could produce slightly better results during summer, while Hay's model resulted in generally better results for the rest of the year.

I.2 Solar radiation geometry

The solar radiation geometry could be illustrated as below:

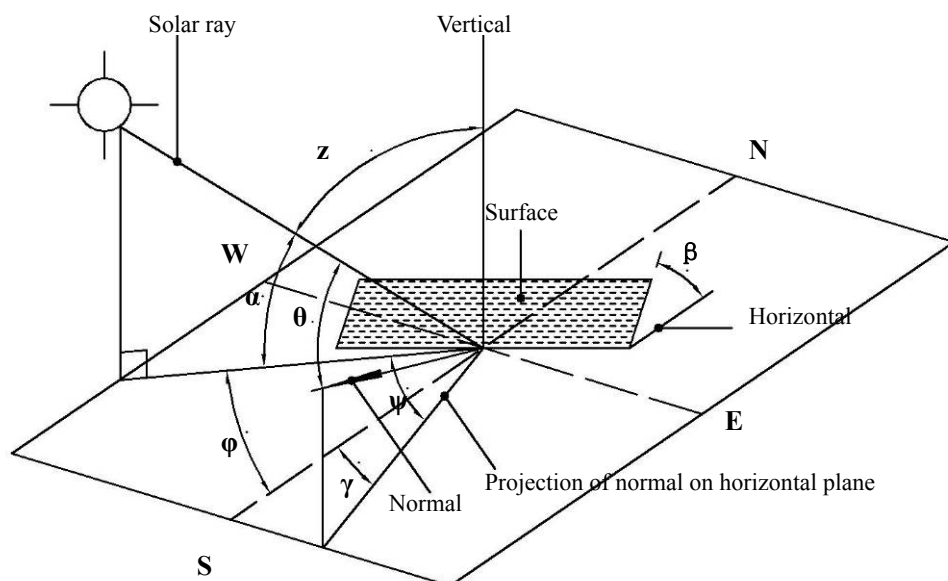


Figure I.2.1 Solar radiation geometry for an inclined surface

Source: A K Athienitis and M Santamouris, Thermal Analysis and Design of Passive Solar Buildings, 2002

For describing the geometric relationship between the direct solar radiation, a horizontal plane and an inclined surface, following angular parameters may be used [1] (and will also be used in later calculations):

- L latitude, equal to the angle of the location relative to the equator (north is positive)
- δ solar declination angle, equal to the angular position of the sun at solar noon with respect

to the equatorial plane (varies from -23.45° to 23.45°)

α solar altitude angle, equal to the angle between the sun's rays and the horizontal ($0^\circ - 90^\circ$)

z zenith angle, equal to the angle between the sun's rays and the vertical

ϕ solar azimuth angle, equal to the angle between the horizontal projection of the sun's rays form due south (positive in the afternoon)

ψ surface solar azimuth angle, equal to the angle between the projections of sun's rays and of the normal to the surface on the horizontal plane

γ surface azimuth angle, equal to the angle between the projection of the normal to the surface on a horizontal plane and due south (west is positive, east is negative)

β surface tilt angle, the angle between the surface and the horizontal ($0^\circ - 180^\circ$)

θ angle of incidence, the angle between the sun's rays and a line normal to the surface

I.3 Hay's anisotropic model

The formula for calculation the daily total radiation incidence on an inclined surface H_T ($H_T = H_B' + H_D' + H_R'$, mentioned in Chapter 3.2) can be written in details as:

$$H_T = H_B R_B + H_D [R_B H_B / H_0 + 0.5(1 - H_B / H_0)(1 + \cos\beta)] + 0.5\rho H(1 - \cos\beta) \quad \text{Formula (7)}$$

Where:

H_T total solar radiation on an inclined surface, $\text{MJ} \cdot (\text{m}^2 \cdot \text{day})^{-1}$

H_B' direct solar radiation on an inclined surface, $\text{MJ} \cdot (\text{m}^2 \cdot \text{day})^{-1}$

H_D' diffuse solar radiation on an inclined surface, $\text{MJ} \cdot (\text{m}^2 \cdot \text{day})^{-1}$

H_R' diffuse solar radiation on an inclined surface, $\text{MJ} \cdot (\text{m}^2 \cdot \text{day})^{-1}$

H_B direct solar radiation on a horizontal surface, $\text{MJ} \cdot (\text{m}^2 \cdot \text{day})^{-1}$

H_D diffuse solar radiation on a horizontal surface, $\text{MJ} \cdot (\text{m}^2 \cdot \text{day})^{-1}$

H_0 whole day normal direct radiation at the top of the atmosphere, $\text{MJ} \cdot (\text{m}^2 \cdot \text{day})^{-1}$

H total solar radiation on a horizontal surface, $\text{MJ} \cdot (\text{m}^2 \cdot \text{day})^{-1}$

R_B ratio of the daily radiation on an inclined surface to that on a horizontal surface

ρ albedo (reflectivity) of the ground (usually is 0.20), dimensionless

R_B is calculated by the incidence angle of sun's rays to the inclined surface (θ) and the solar zenith angle (z), and the incidence angle to be calculated through other angular parameters mentioned in the solar radiation geometry. The expressions are written as:

$$R_B = \cos\theta / \cos z \quad \text{Formula (8)}$$

$$\theta = \cos^{-1}[\cos z \cos\beta + \sin z \sin\beta \cos(\psi - \gamma)] \quad \text{Formula (9)}$$

$$z = \cos^{-1}[\sin\delta \sin\phi + \cos\phi \cos\delta \cos\omega] \quad \text{Formula (10)}$$

Where:

ω solar hour angle

Other parameters refer to the solar radiation geometry

For calculation of solar radiation, the input data of hourly time intervals ω is often needed in Formula (10), which leads to an undesirable increase in the required computational effort. But Hay presented a simplified method of calculation of monthly mean solar radiation for inclined surfaces

by using daily rather than hourly time intervals without any significant reduction in the accuracy of the calculated value (Hay, 1979). He suggested using the mean daily solar zenith angle \hat{z} , which could be calculated using the following equation:

$$\cos \hat{z} = H_s/H_k \tag{Formula (11)}$$

Where:

H_s whole day total solar radiation incident on a horizontal surface at the top of the atmosphere for half day length ω_s , MJ \cdot (m² \cdot day)⁻¹

H_k whole day normal incidence direct radiation at the top of the atmosphere for half day length ω_s , MJ \cdot (m² \cdot day)⁻¹

The other formulas for calculations of H_s and H_k , as well as H_b , H_0 and H can refer to the Processing code in Appendix IV, and also Hay's original paper: *Calculation of monthly mean solar radiation for horizontal and inclined surfaces*, 1979.

I.4 3D and 2D radiation plots

Figure I.4.1 and Figure I.4.2 demonstrate 3D and 2D radiation plots of an example calculated by Hay's anisotropic model.

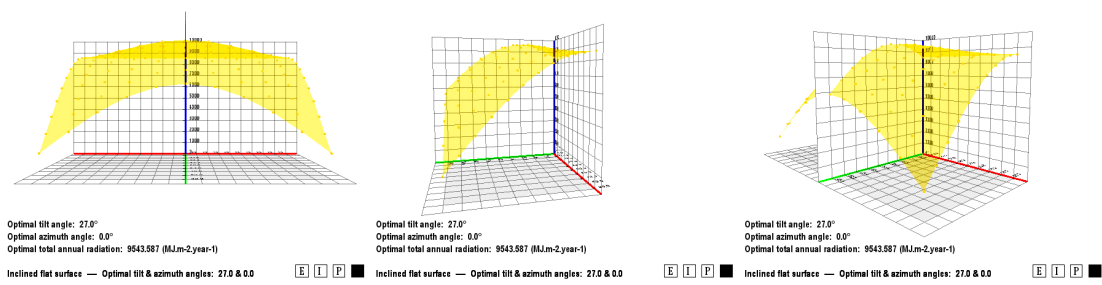


Figure I.4.1 3D radiation plot by Hay's anisotropic model

Left: front view; middle: side view; right: perspective

(Angle-setting: $\beta = 0^\circ \sim 90^\circ$, $\gamma = -90^\circ \sim 90^\circ$; solar condition setup: $L = 51.3^\circ N$, clear-sky mode)

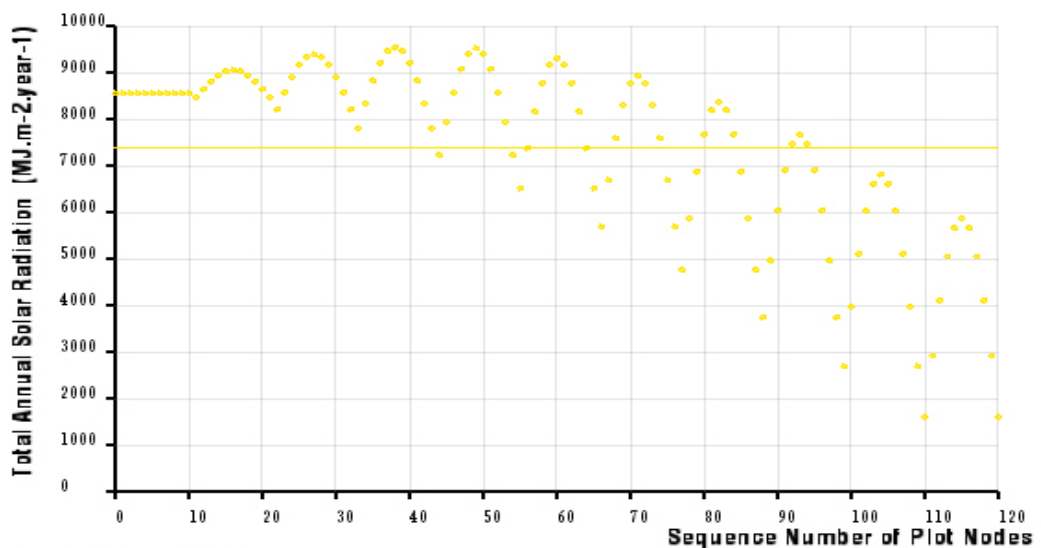


Figure I.4.2 2D radiation plot by Hay's anisotropic model

(Angle-setting: $\beta = 0^\circ \sim 90^\circ$, $\gamma = -90^\circ \sim 90^\circ$; solar condition setup: $L = 51.3^\circ N$, clear-sky mode)

In Figure I.4.1, the following important information can thus be known for an inclined surface:

- Optimal azimuth angle: 0.0° (equals to the due south)
- Optimal tilt angle: 27°
- Optimal total annual solar radiation: $9543.587 \text{ MJ} \cdot (\text{m}^2 \cdot \text{year})^{-1}$

In Figure I.4.2, it is easy to notice that, when the tilt angle β is equal to 0° (the section of the first eleven plot nodes), the radiation spectrum is seen as a horizontal line, which means if the flat surface is just horizontally mounted, no matter what value of the azimuth angle γ is, the radiation incidence on it would be all the same—or say there is no effect no matter how the surface might be rotated! However, with the increase of β , by the given range of γ (from -90° to 90°), the following ten sections of the spectrum (11 nodes for each) display gradually larger ranges of top-down vibratility, which may reveal that the surface azimuth angle can produce certain effects on the radiation incidence when the surface tilt angle becomes bigger (the worst positions are those that face the due west and the due east).

I.5 Solar radiation in different latitudes

Various 3D/2D radiation plots might also be achieved and thus compared if more different latitudes are chosen. For example, the following comparisons (Figure I.5.1 and Figure I.5.2) are made according to five different locations with latitudes from low to high (3.45° N ; 18.58° N ; 31.2° N ; 51.3° N ; 60.1° N).

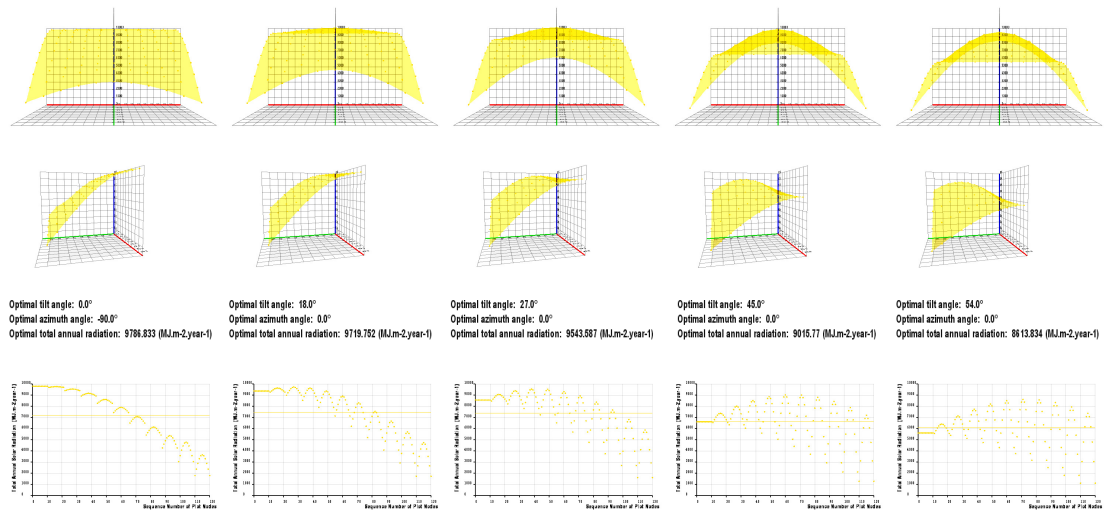


Figure I.5.1 3D and 2D solar radiation plots of five locations

From left to right: $L = 3.45^\circ \text{ N}$; 18.58° N ; 31.2° N ; 51.3° N ; 60.1° N (the latitudes respectively equal to Malabo, Equatorial Guinea; Bombay, India; Shanghai, China; London, UK; Helsinki, Finland)

(Angle-setting: $\beta = 0^\circ \sim 90^\circ$, $\gamma = -90^\circ \sim 90^\circ$; solar condition setup: $L = 51.3^\circ \text{ N}$, clear-sky mode)

In Figure I.5.1, the optimal angles for inclined surface (node $[\beta_{opt}] [\gamma_{opt}]$) changes in the way in which β_{opt} gets gradually increased and γ_{opt} keeps a value of 0° (always prefer to the due south). Notice that although this comparison is made in clear-sky mode, there should be a similar trend in cloud-cover mode, as the optimal angle-setting is primarily determined by the position of the sun to the location on the earth.

In Figure I.5.2, the combined diagram of the five 2D radiation plots seems suggest that the spectrums of the low latitudes are more sensitive to the change of surface tilt angle, while those of the high latitudes are more easily vibrated by the change of surface azimuth angle. When the tilt angle is within a small range (e.g. less than 20°), the total annual solar radiation of the lower latitudes can be seen more than that of the higher latitudes. The mean total annual solar radiation, represented by the horizontal line, is also having a similar declined trend from lower latitudes to higher latitudes. But because it is an average value calculated from a full range of angle-settings, the lowest latitude 3.45°N of the five does not take a lead for the reason that the radiation decreases very sharply when the tilt angle is increasing.

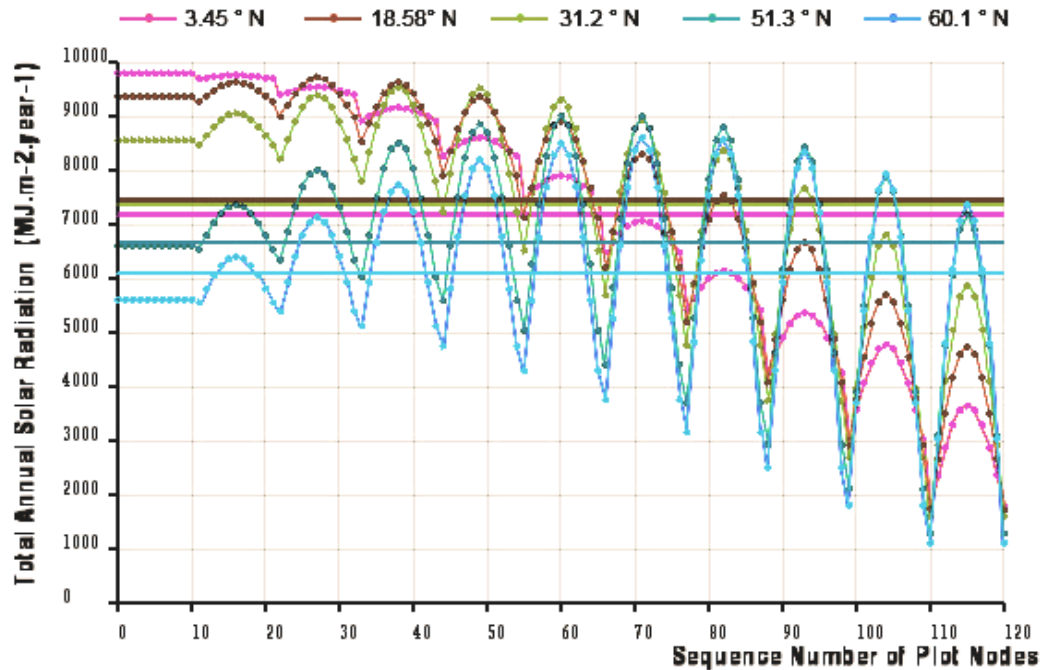


Figure I.5.2 Comparison of 2D solar radiation plots of five latitudes

Latitude: 3.45°N; 18.58°N; 31.2°N; 51.3°N; 60.1°N

(Angle-setting: $\beta = 0^\circ \sim 90^\circ$, $\gamma = -90^\circ \sim 90^\circ$; solar condition setup: clear-sky mode)

Appendix II

Illustrations of results of different latitudes

II.1 Latitude 3.45°N ($\beta = 0^\circ \sim 30^\circ$, $\gamma = 0^\circ \sim 30^\circ$)

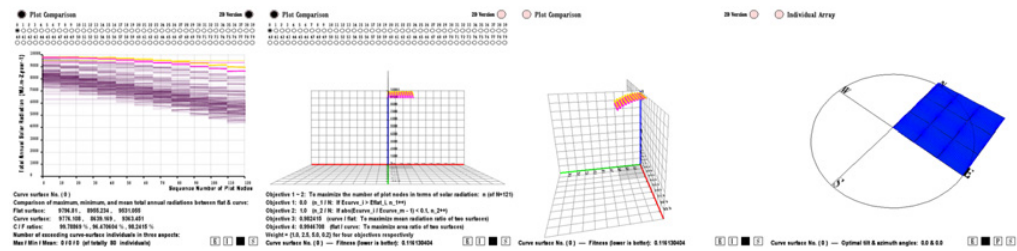


Figure II.1.1 Latitude 3.45°N – Phase 1 (Generation No.0; Individual No. 0)

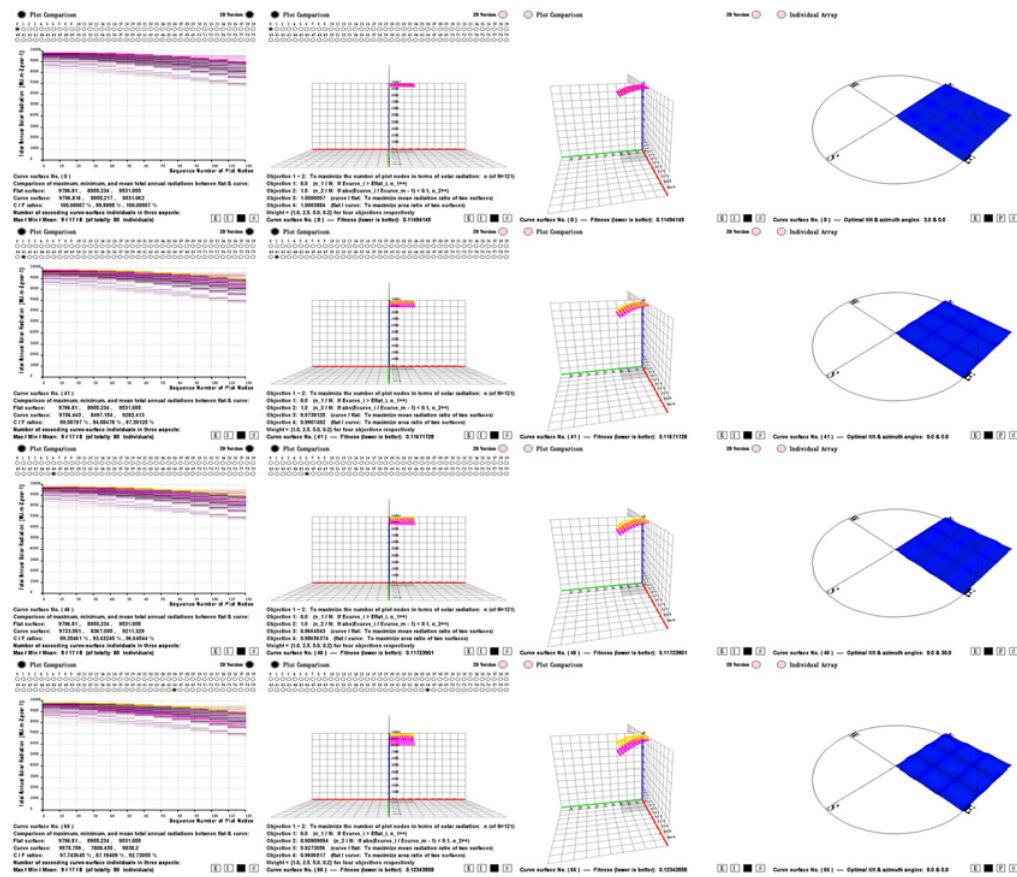


Figure II.1.2 Latitude 3.45°N – Phase 2 (Generation No.100; Individual No. from top to bottom: 0; 41; 46; 60)

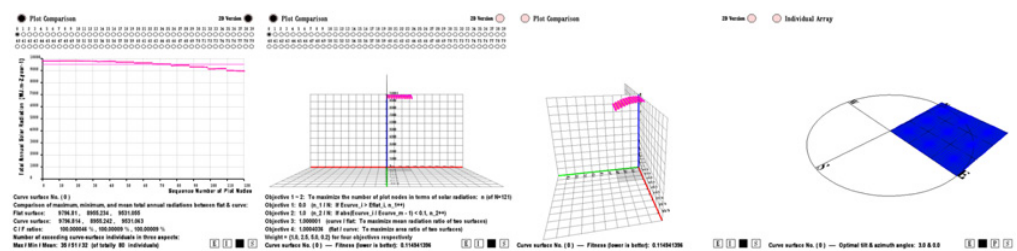


Figure II.1.3 Latitude 3.45°N – Phase 3 (Generation No.200; Individual No. 0 – final optimal curved surface)

II.2 Latitude 18.58°N ($\beta = 0^\circ \sim 30^\circ, \gamma = 0^\circ \sim 30^\circ$)

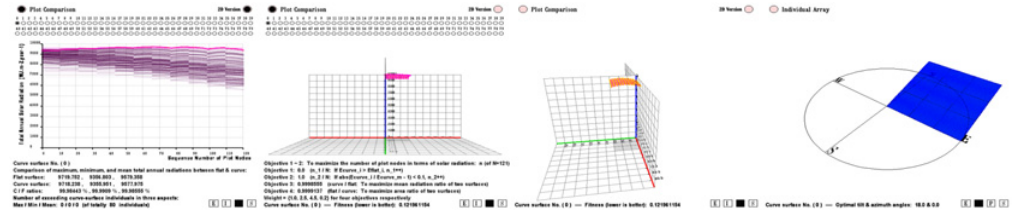


Figure II.2.1 Latitude 18.58°N – Phase 1 (Generation No. 0; Individual No. 0)

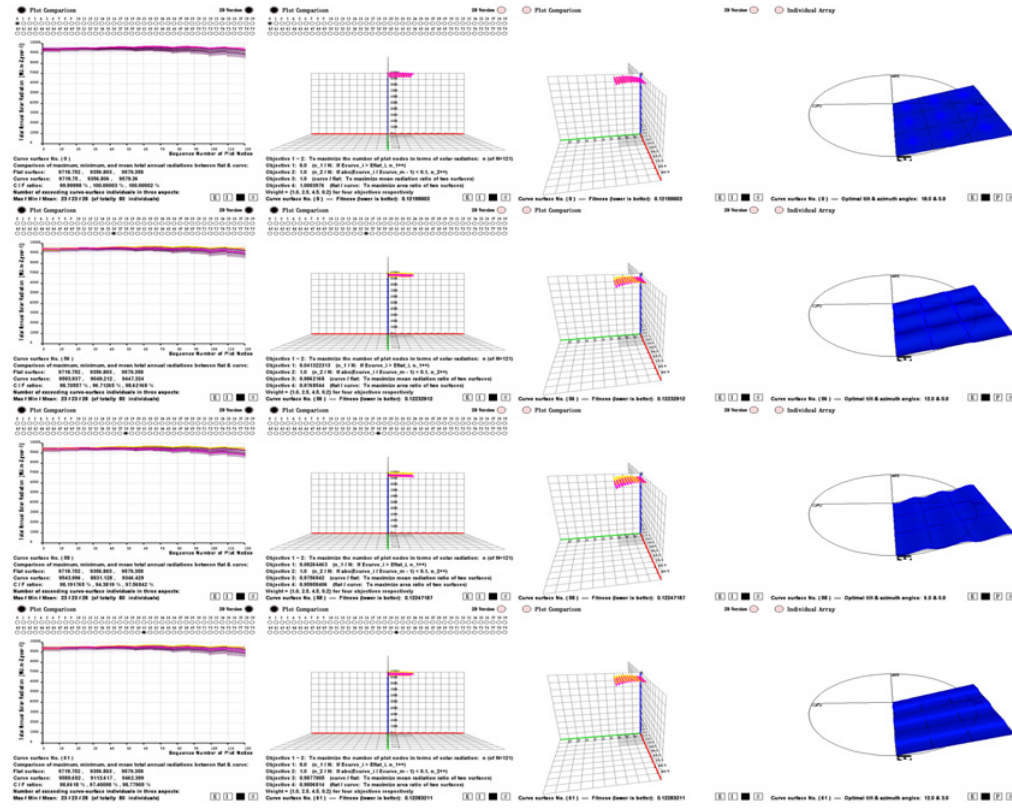


Figure II.2.2 Latitude 18.58°N – Phase 2 (Generation No.100; Individual No. from top to bottom: 0; 56; 58; 61)

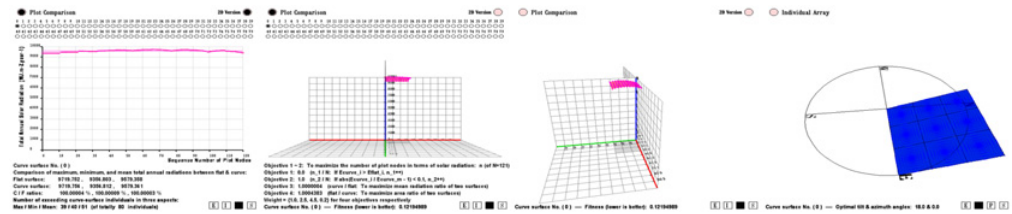


Figure II.2.3 Latitude 18.58°N – Phase 3 (Generation No.200; Individual No. 0 – final optimal curved surface)

II.3 Latitude 31.2°N ($\beta = 0^\circ \sim 30^\circ, \gamma = 0^\circ \sim 30^\circ$)

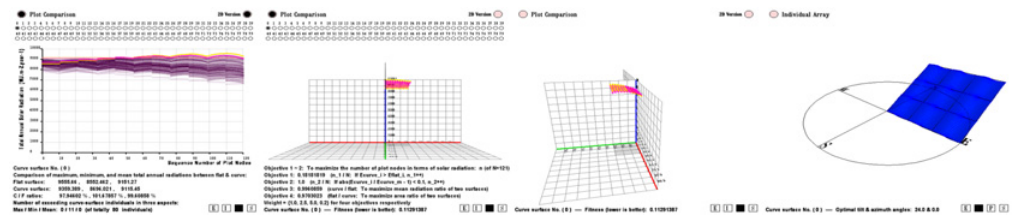


Figure II.3.1 Latitude 31.2°N – Phase 1 (Generation No. 0; Individual No. 0)

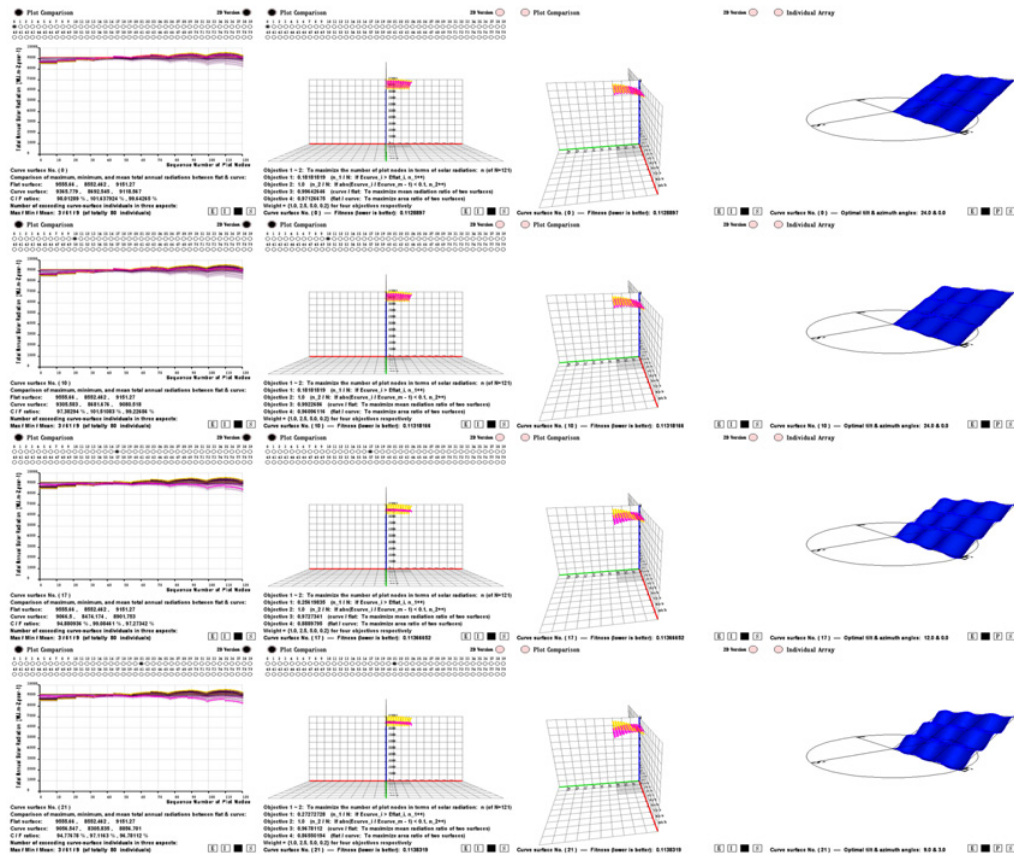


Figure II.3.2 Latitude 31.2°N – Phase 2 (Generation No.100; Individual No. from top to bottom: 0; 10; 17; 21)

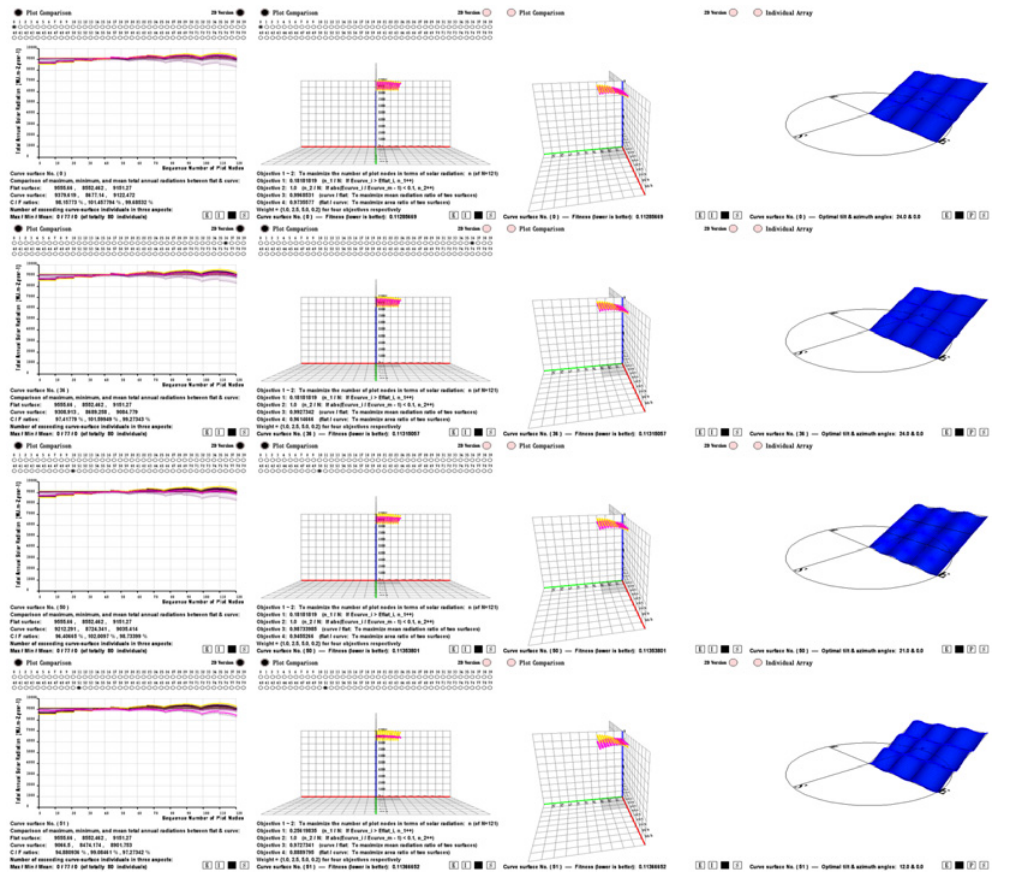


Figure II.3.3 Latitude 31.2°N – Phase 3 (Generation No.200; Individual No. from top to bottom: 0; 36; 50; 51)

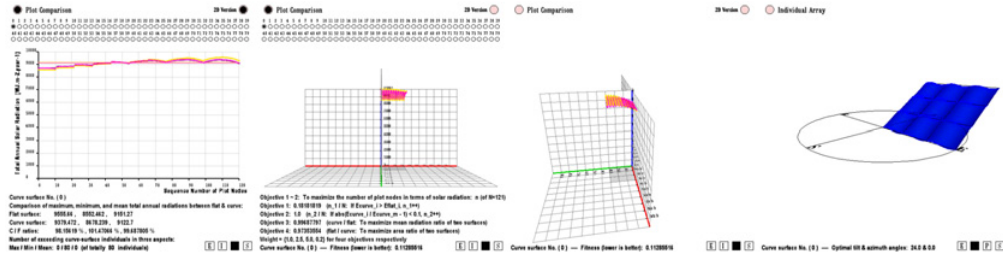


Figure II.3.4 Latitude 31.2°N – Phase 4 (Generation No.355; Individual No. 0 – final optimal curved surface)

II.4 Latitude 51.3°N ($\beta = 0^\circ \sim 30^\circ, \gamma = 0^\circ \sim 30^\circ$)

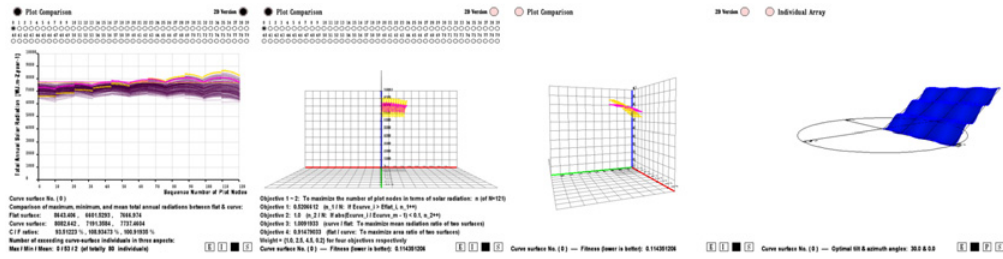


Figure II.4.1 Latitude 51.3°N – Phase 1 (Generation No. 0; Individual No. 0)

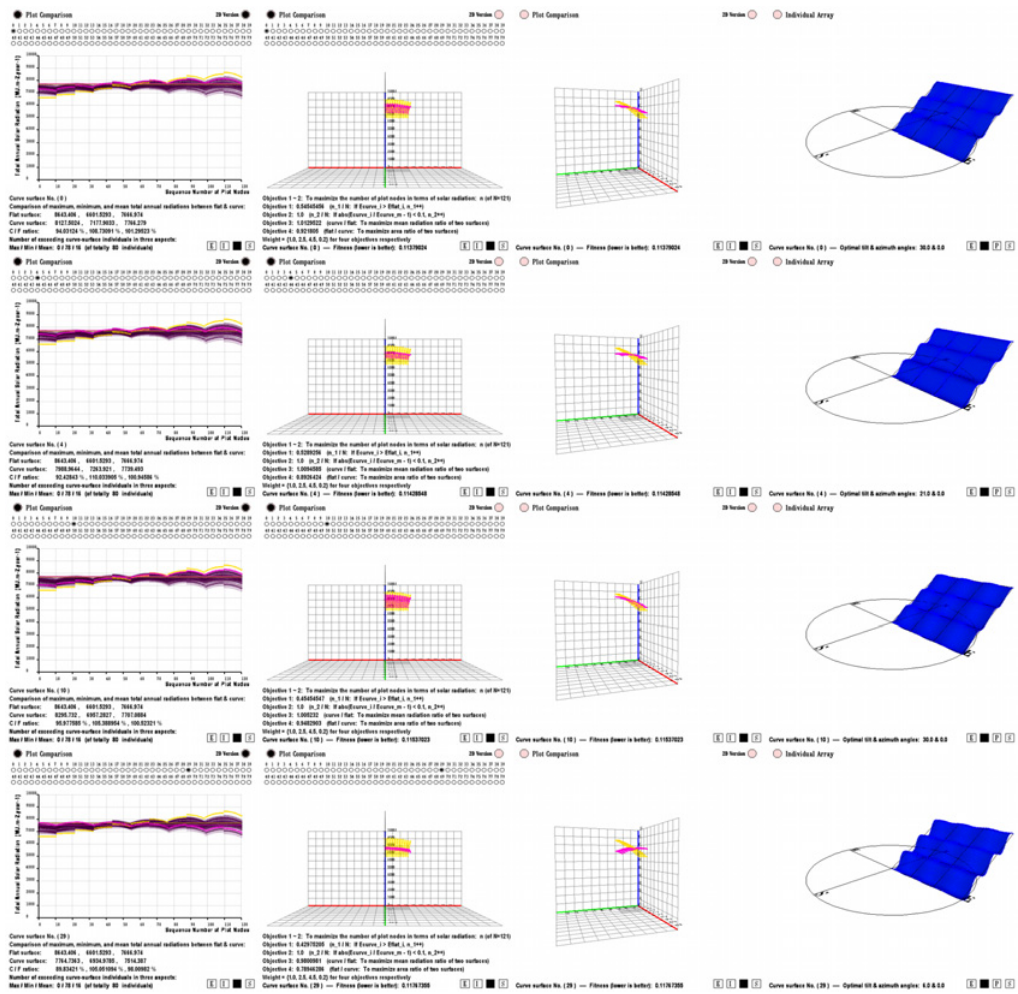


Figure II.4.2 Latitude 51.3°N – Phase 2 (Generation No.101; Individual No. from top to bottom: 0; 4; 10; 29)

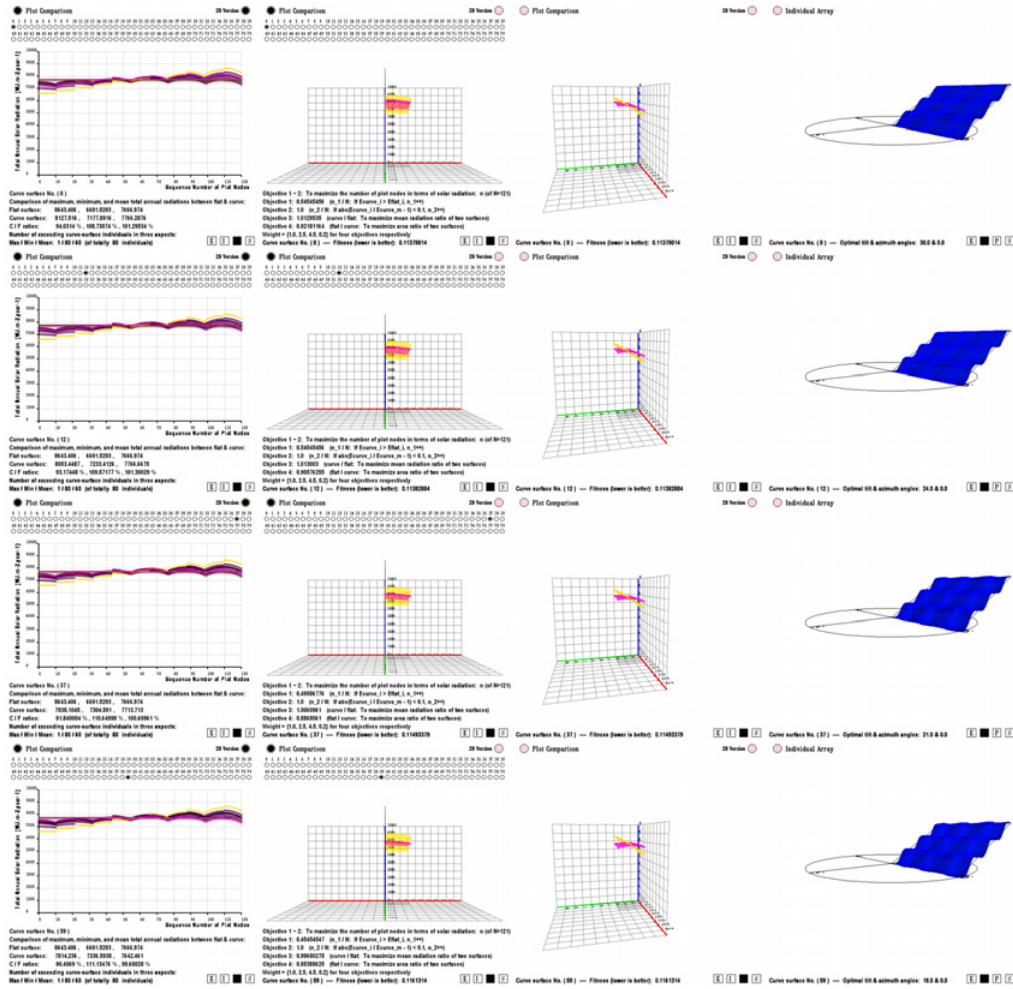


Figure II.4.3 Latitude 51.3°N – Phase 3 (Generation No.201; Individual No. from top to bottom: 0; 12; 37; 59)

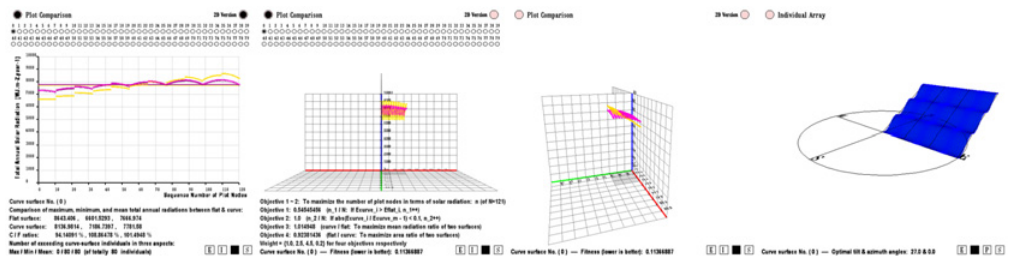


Figure II.4.4 Latitude 51.3°N – Phase 4 (Generation No.338; Individual No. 0 – final optimal curved surface)

II.5 Latitude 60.1°N ($\beta = 0^\circ \sim 30^\circ$, $\gamma = 0^\circ \sim 30^\circ$)

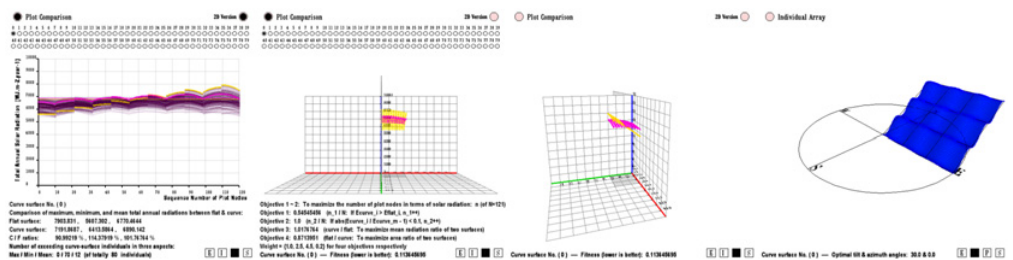


Figure II.5.1 Latitude 60.1°N – Phase 1 (Generation No. 0; Individual No. 0)

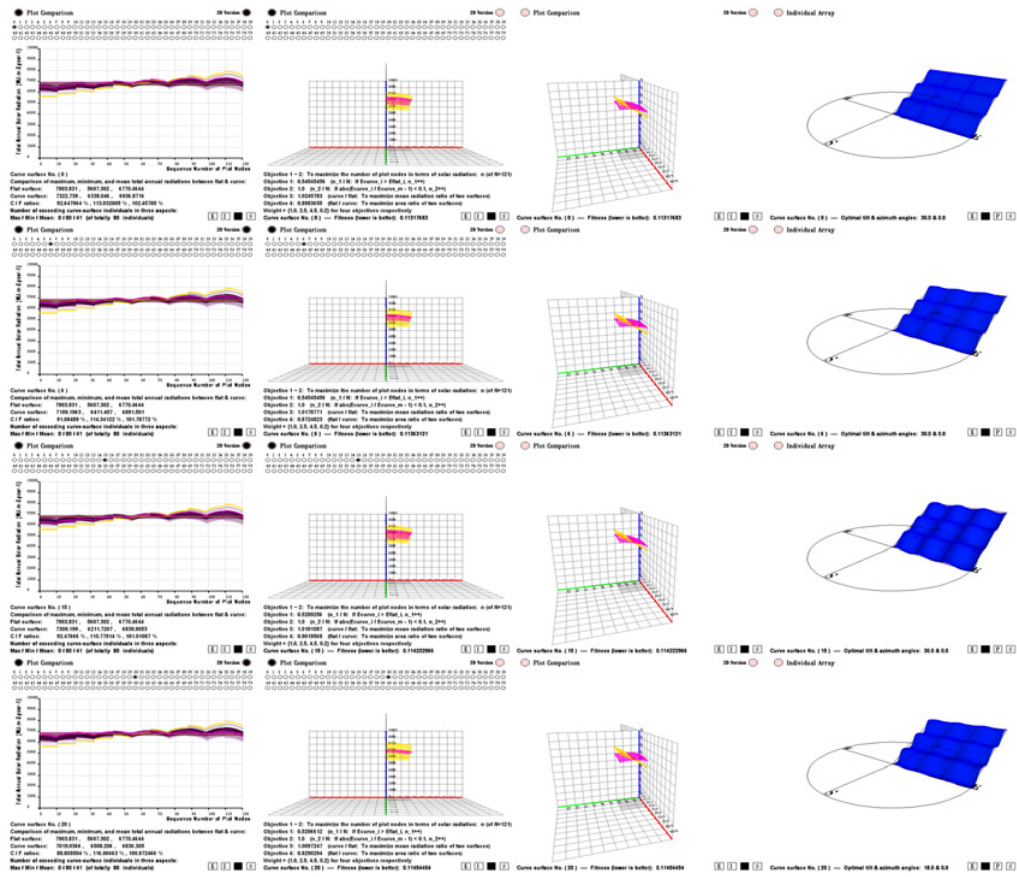


Figure II.5.2 Latitude 60.1°N – Phase 2 (Generation No.100; Individual No. from top to bottom: 0; 6; 15; 20)

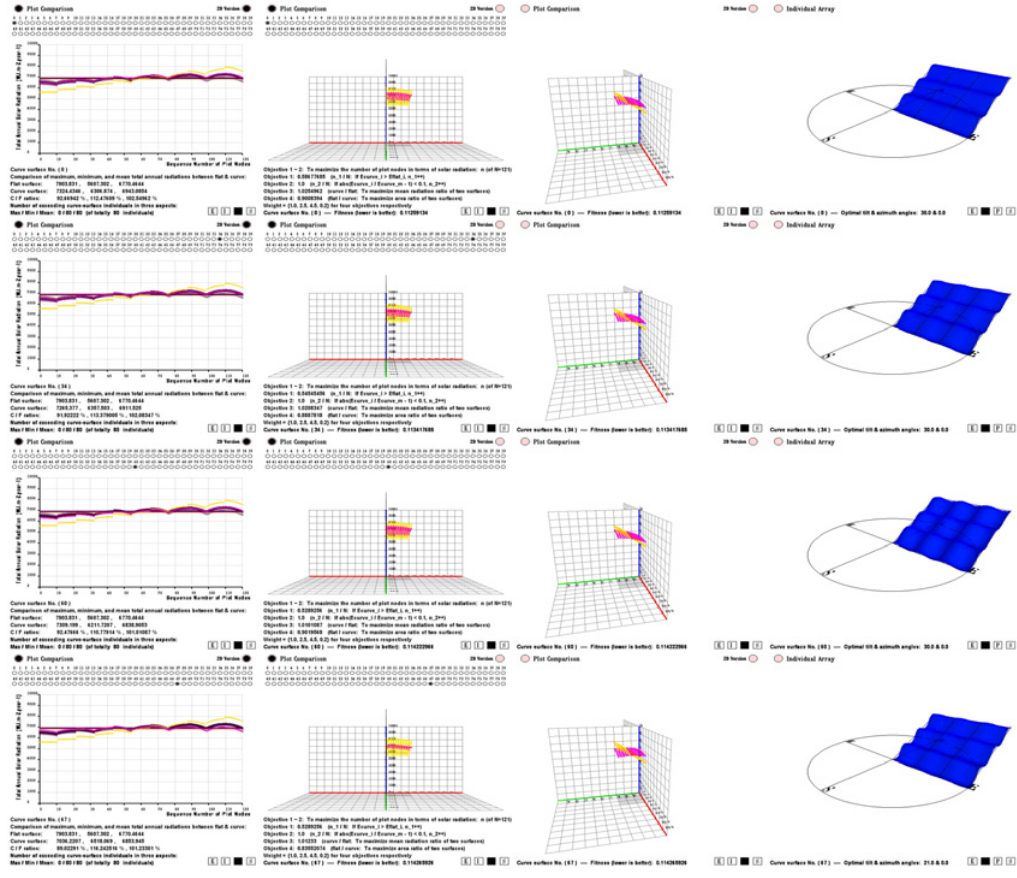


Figure II.5.3 Latitude 60.1°N – Phase 3 (Generation No.201; Individual No. from top to bottom: 0; 34; 60; 67)

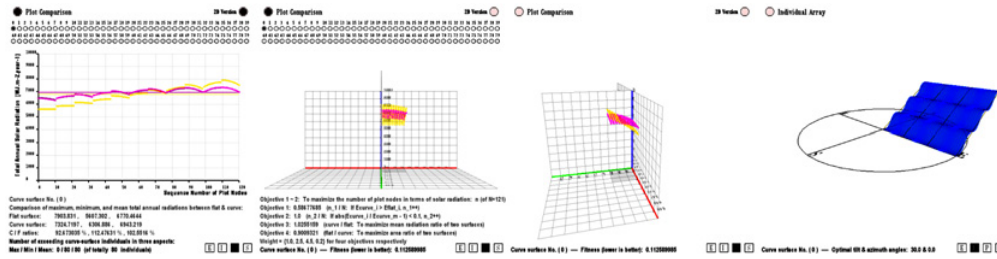


Figure II.5.4 Latitude 60.1°N – Phase 4 (Generation No.321; Individual No. 0 – final optimal curved surface)

Appendix III

Illustrations of results of different angle-settings

III.1 Angle-settings of F and H (L= 51.3°N)

Angle-setting of F: $\beta = 0^\circ \sim 90^\circ$, $\gamma = -90^\circ \sim 90^\circ$

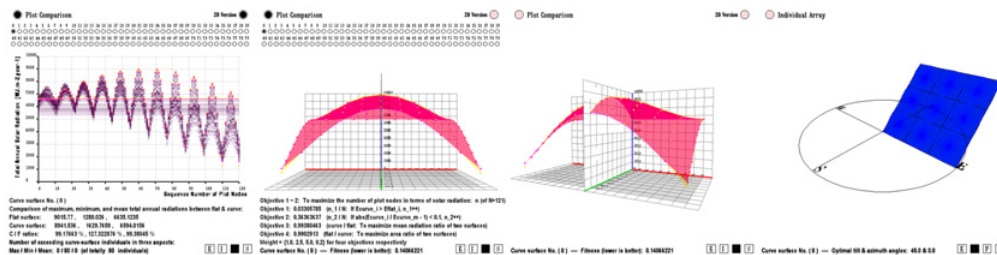


Figure III.1.1 F – Phase 1 (Generation No. 0; Individual No. 0)

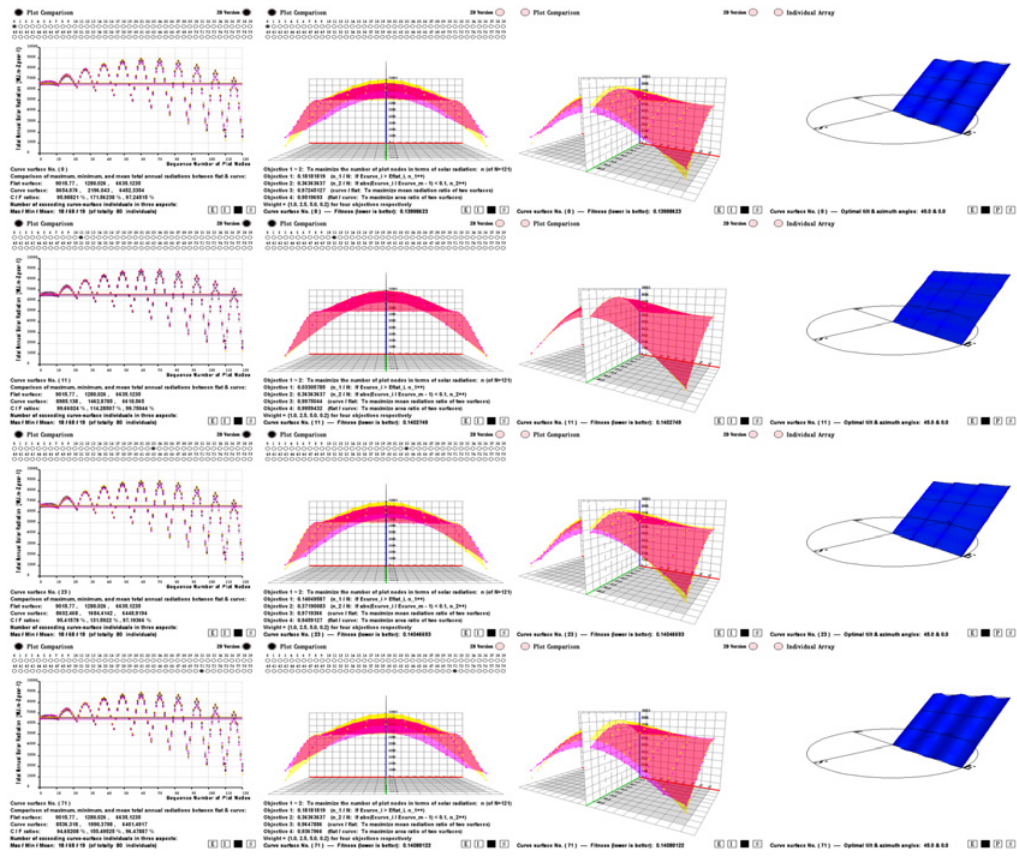


Figure III.1.2 F – Phase 2 (Generation No.100; Individual No. from top to bottom: 0; 11; 23; 71)

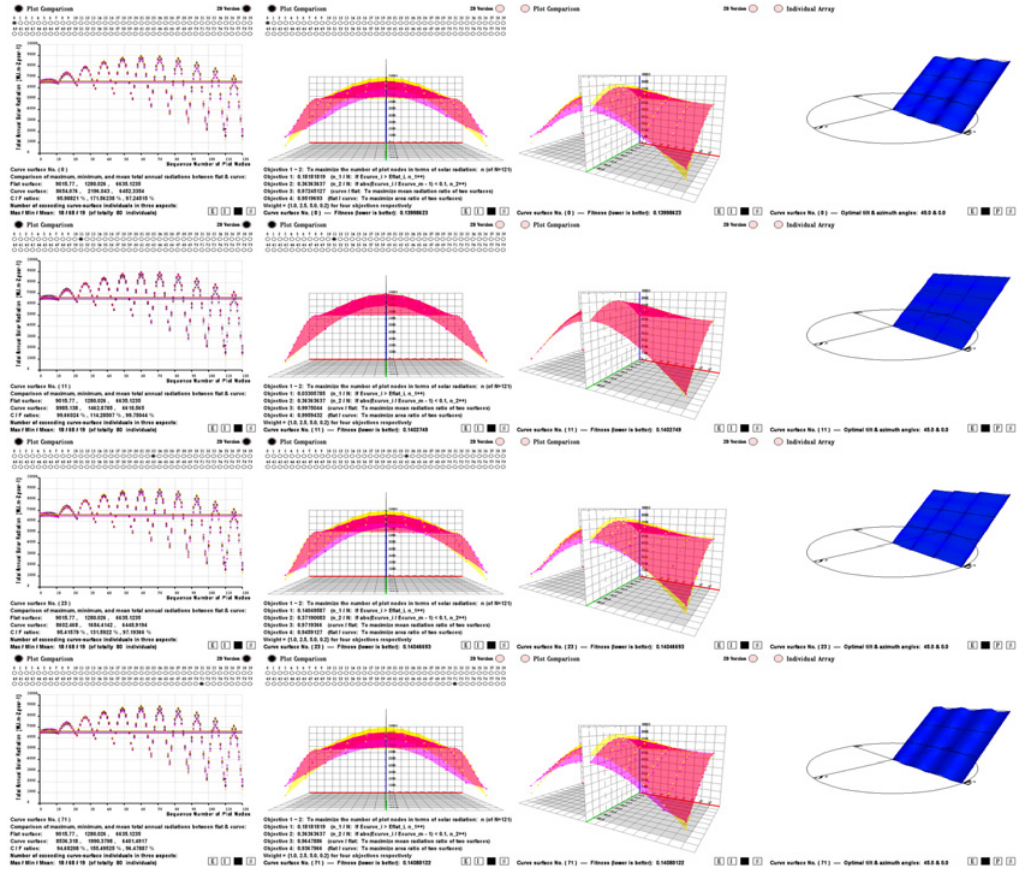


Figure III.1.3 F – Phase 3 (Generation No.100; Individual No. from top to bottom: 0; 18; 40; 60)

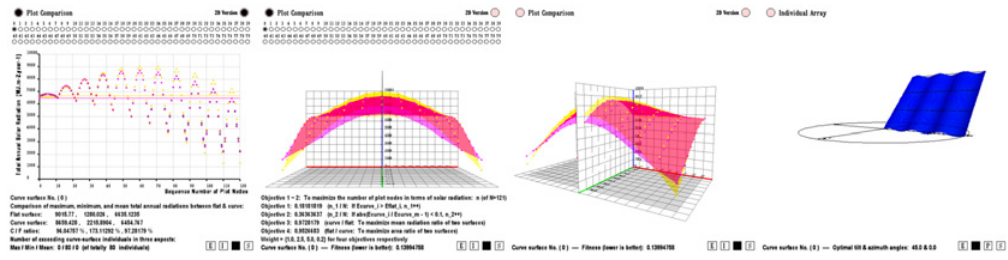


Figure III.1.4 F – Phase 4 (Generation No.337; Individual No. 0 – final optimal curved surface)

Angle-setting of H : $\beta = 0^\circ \sim 90^\circ$, $\gamma = 0^\circ \sim 90^\circ$

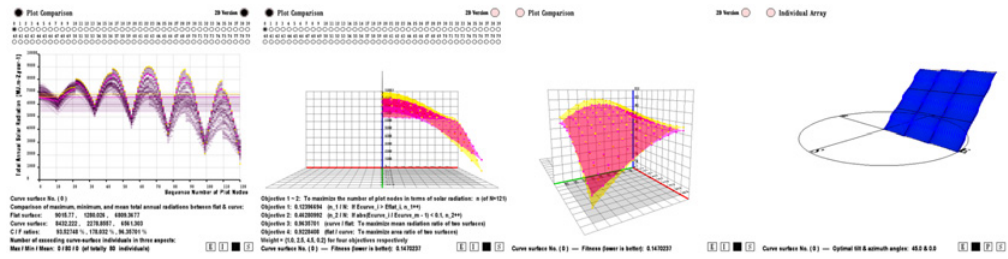


Figure III.1.5 H – Phase 1 (Generation No. 0; Individual No. 0)

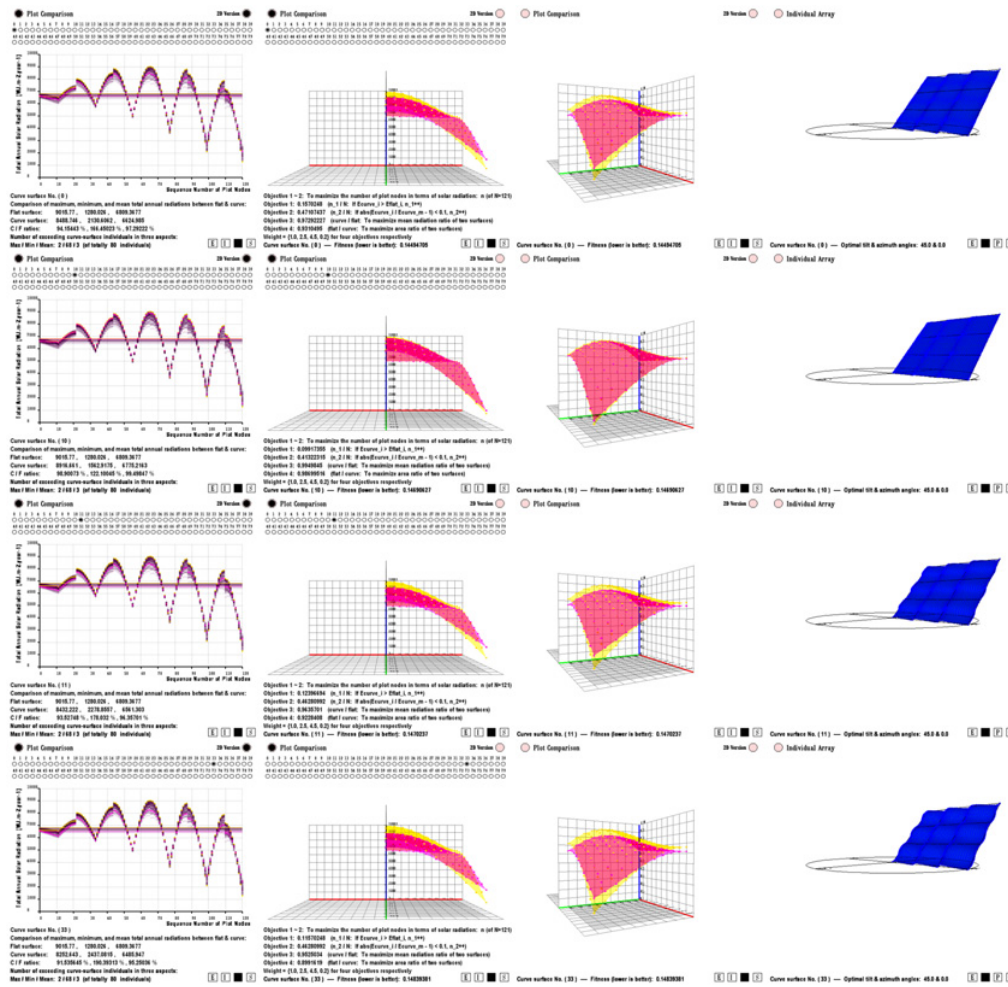


Figure III.1.6 H – Phase 2 (Generation No.100; Individual No. from top to bottom: 0; 10; 11; 33)

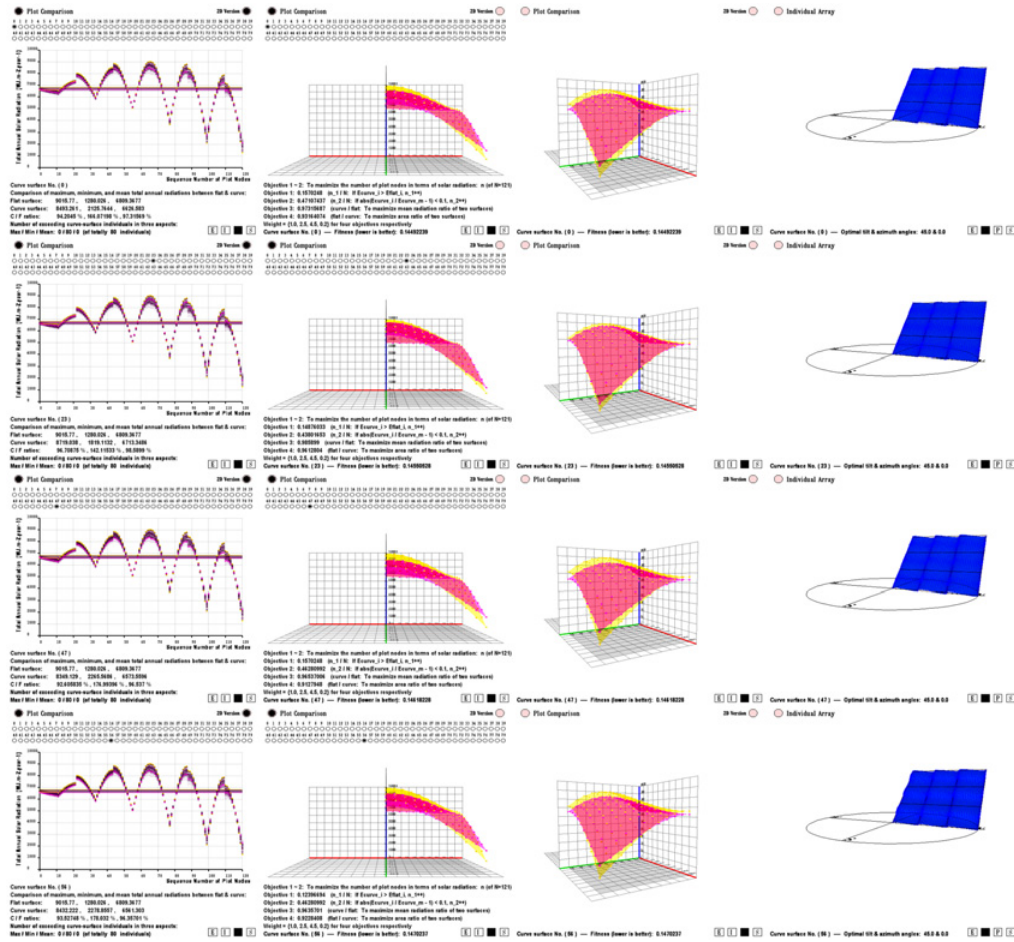


Figure III.1.7 H – Phase 3 (Generation No.200; Individual No. from top to bottom: 0; 23; 47; 56)

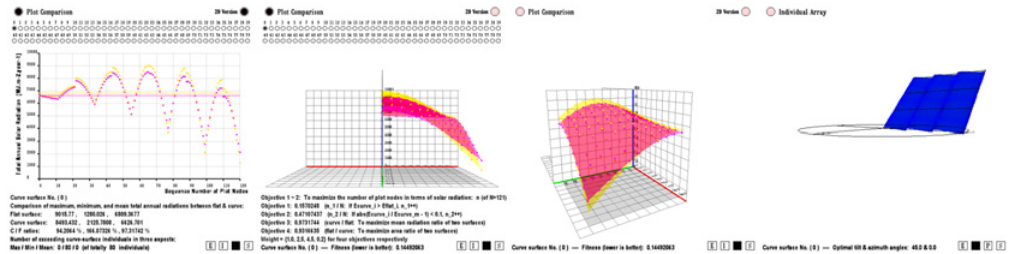
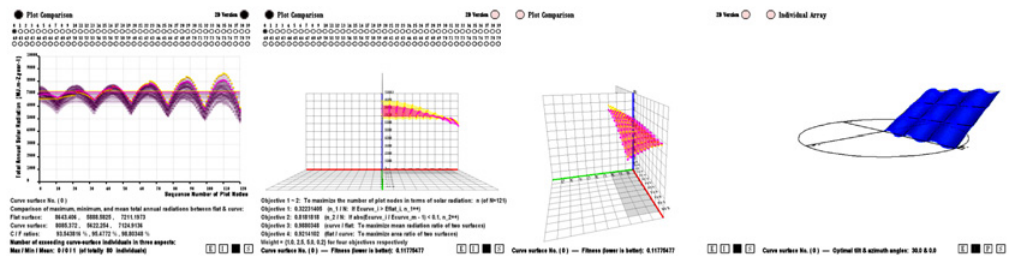


Figure III.1.8 H – Phase 4 (Generation No.315; Individual No. 0 – final optimal curved surface)

III.2 Angle-settings of H β (L= 51.3°N)

Angle-setting of H β -1: $\beta = 0^\circ \sim 30^\circ$, $\gamma = 0^\circ \sim 90^\circ$



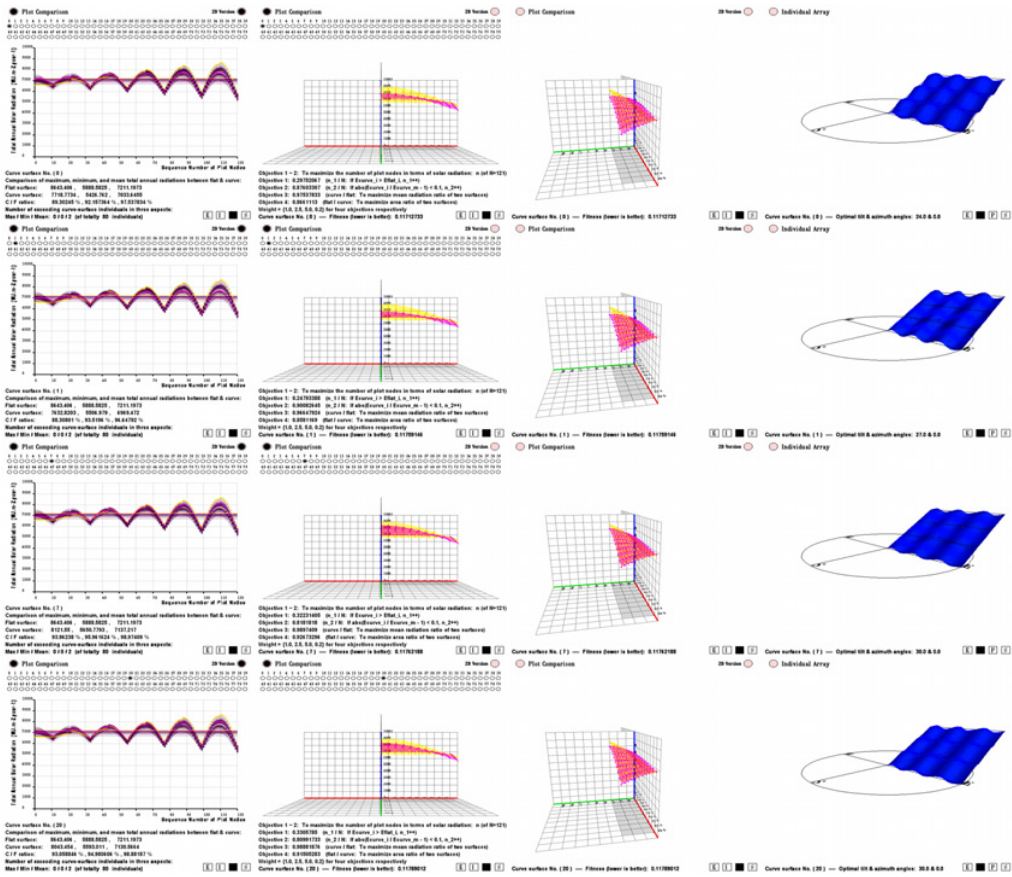


Figure III.2.2 H β -1 – Phase 2 (Generation No.100; Individual No. from top to bottom: 0; 1; 7; 20)

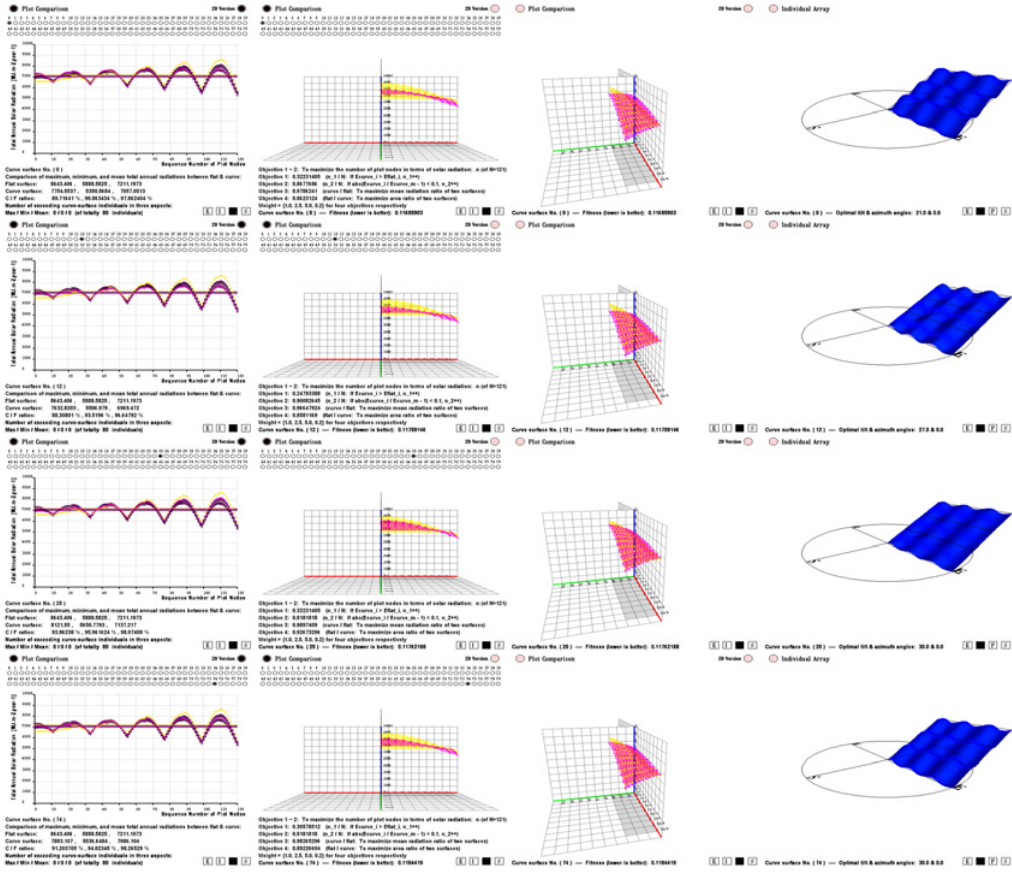


Figure III.2.3 H β -1 – Phase 3 (Generation No.100; Individual No. from top to bottom: 0; 12; 25; 74)

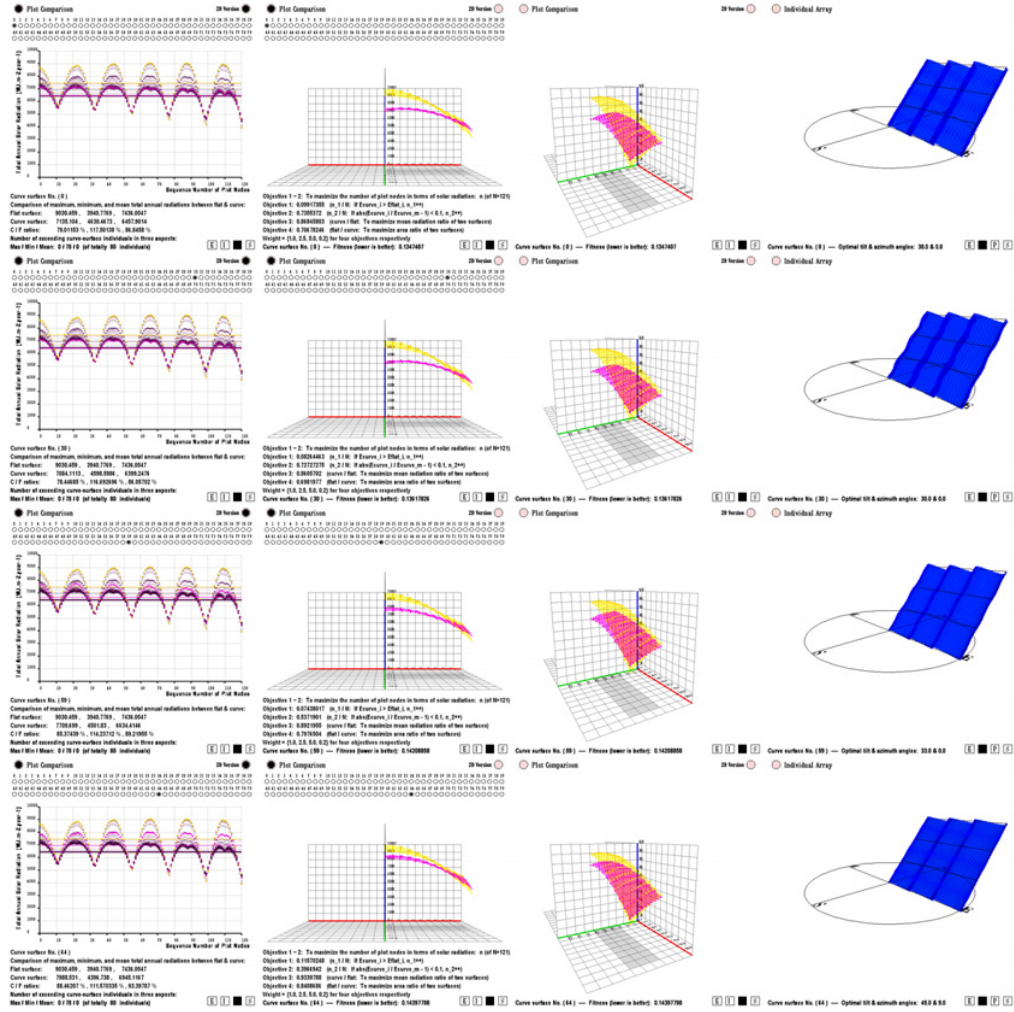


Figure III.2.7 $H\beta-2$ – Phase 3 (Generation No.202; Individual No. from top to bottom: 0; 30; 59; 64)

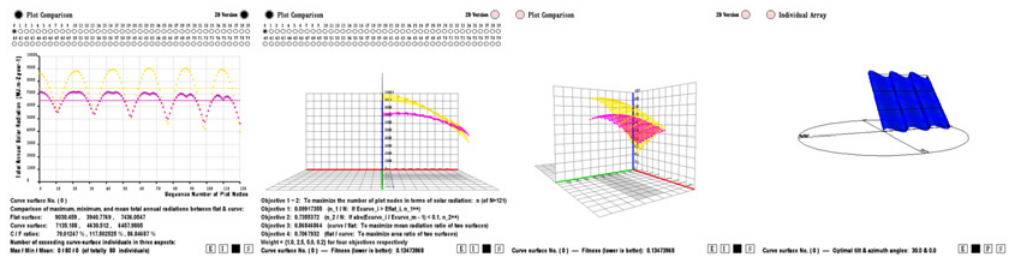


Figure III.2.8 $H\beta-2$ – Phase 4 (Generation No.309; Individual No. 0 – final optimal curved surface)

Angle-setting of $H\beta-3$: $\beta = 60^\circ \sim 90^\circ$, $\gamma = 0^\circ \sim 90^\circ$

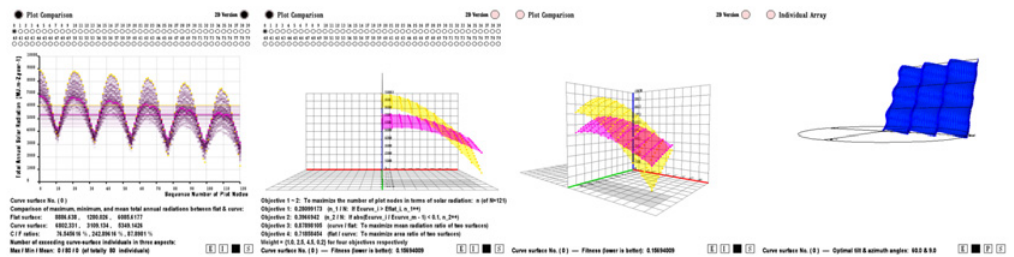
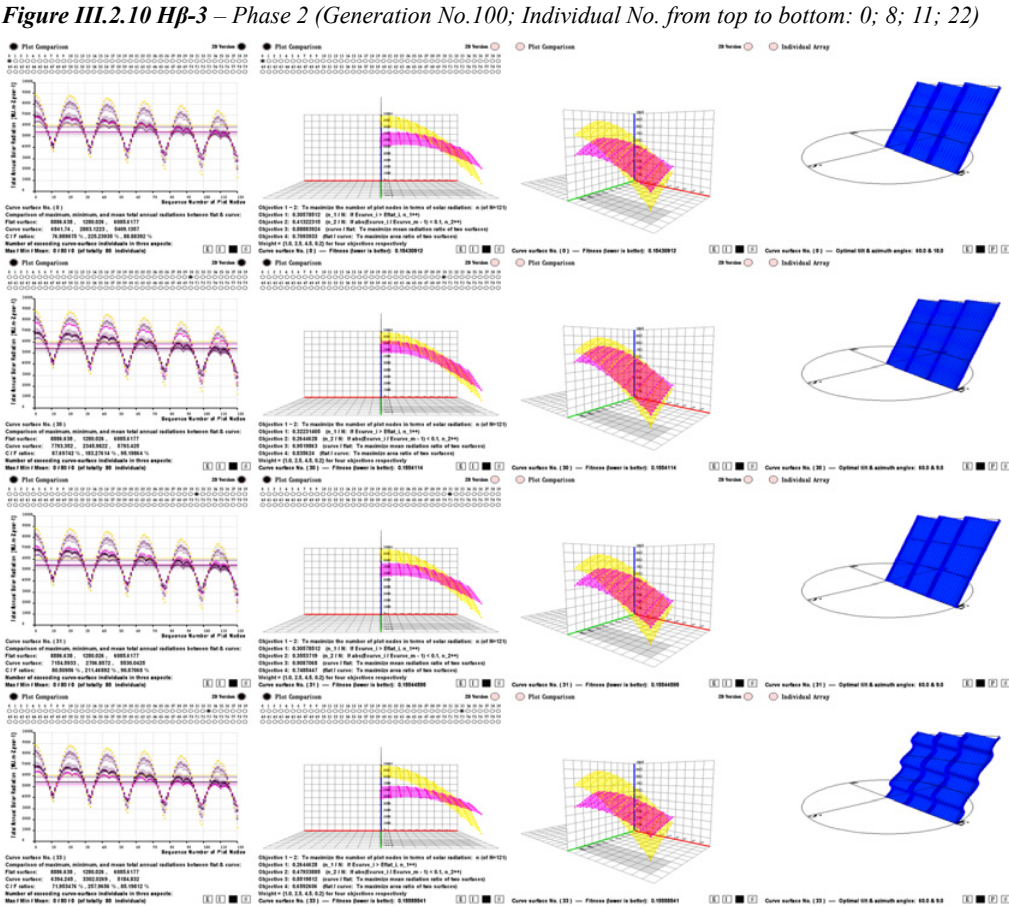
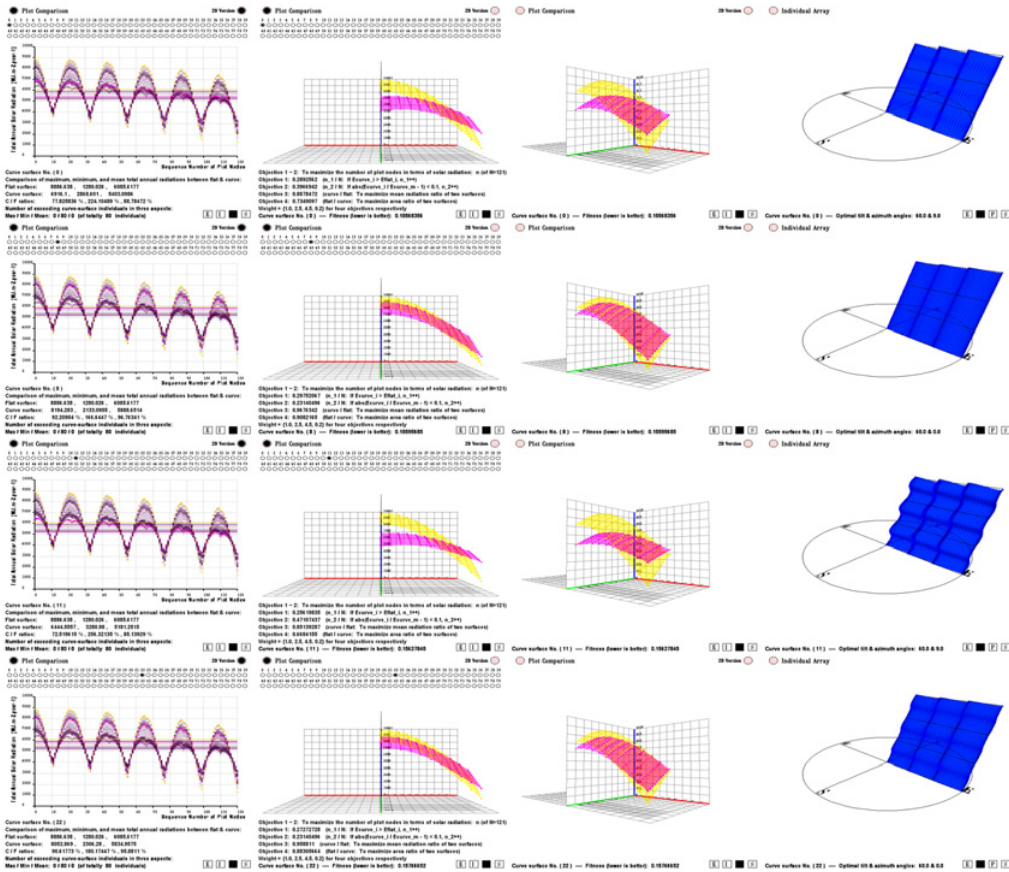


Figure III.2.9 $H\beta-3$ – Phase 1 (Generation No. 0; Individual No. 0)



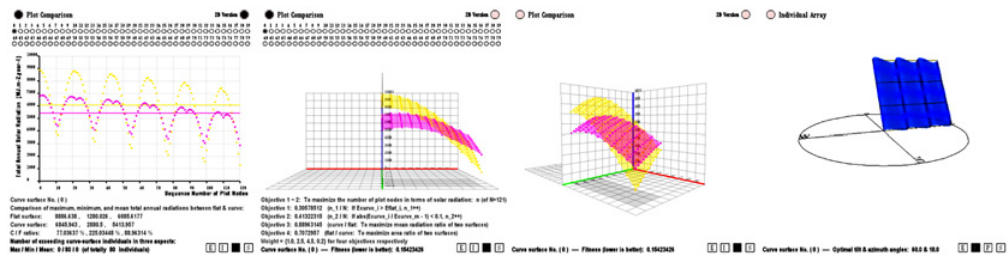


Figure III.2.12 Hβ-3 – Phase 4 (Generation No.350; Individual No. 0 – final optimal curved surface)

III.3 Angle-settings of Hy (L= 51.3°N)

Angle-setting of Hy-I: $\beta = 0^\circ \sim 90^\circ$, $\gamma = 0^\circ \sim 30^\circ$

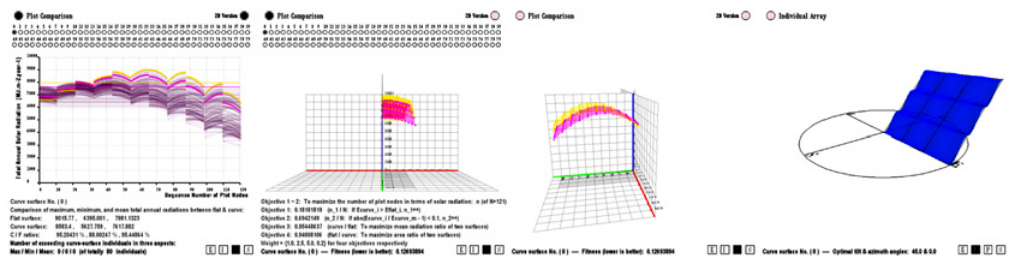


Figure III.3.1 Hy-1 – Phase 1 (Generation No. 0; Individual No. 0)

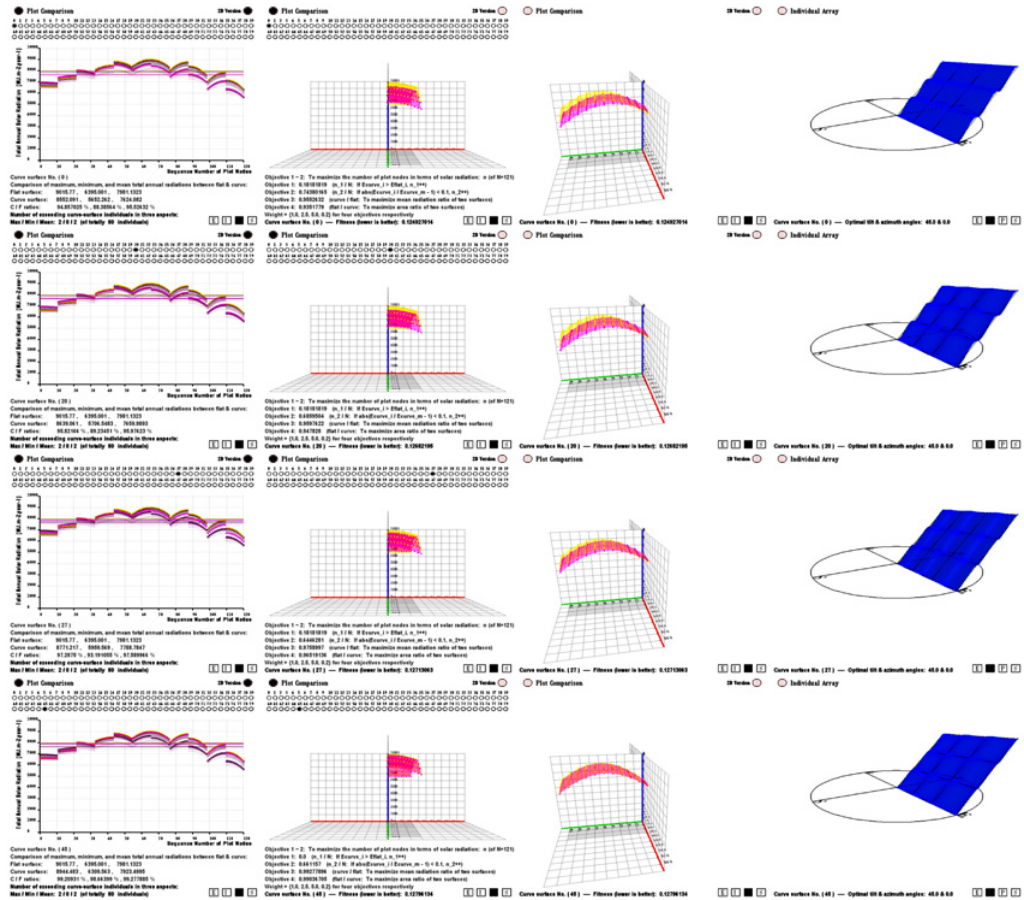


Figure III.3.2 Hy-1 – Phase 2 (Generation No.100; Individual No. from top to bottom: 0; 20; 27; 45)

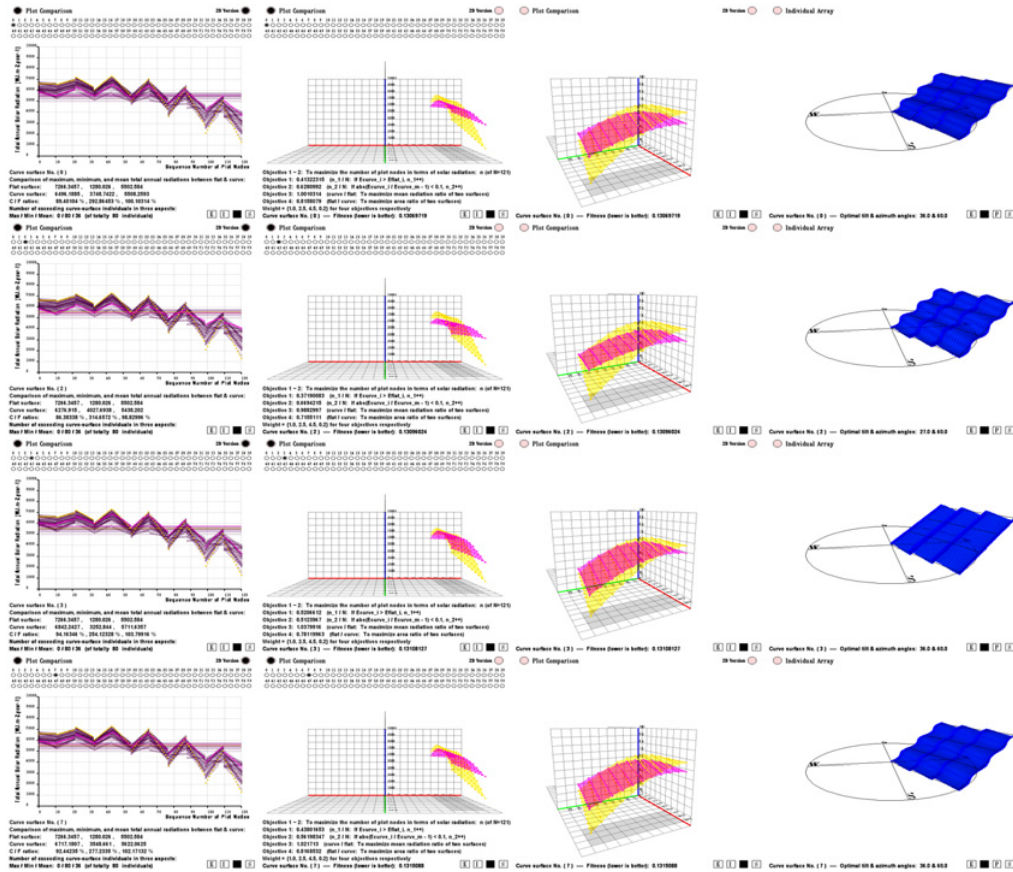


Figure III.3.9 Hy-3 – Phase 2 (Generation No.100; Individual No. from top to bottom: 0; 2; 3; 7)

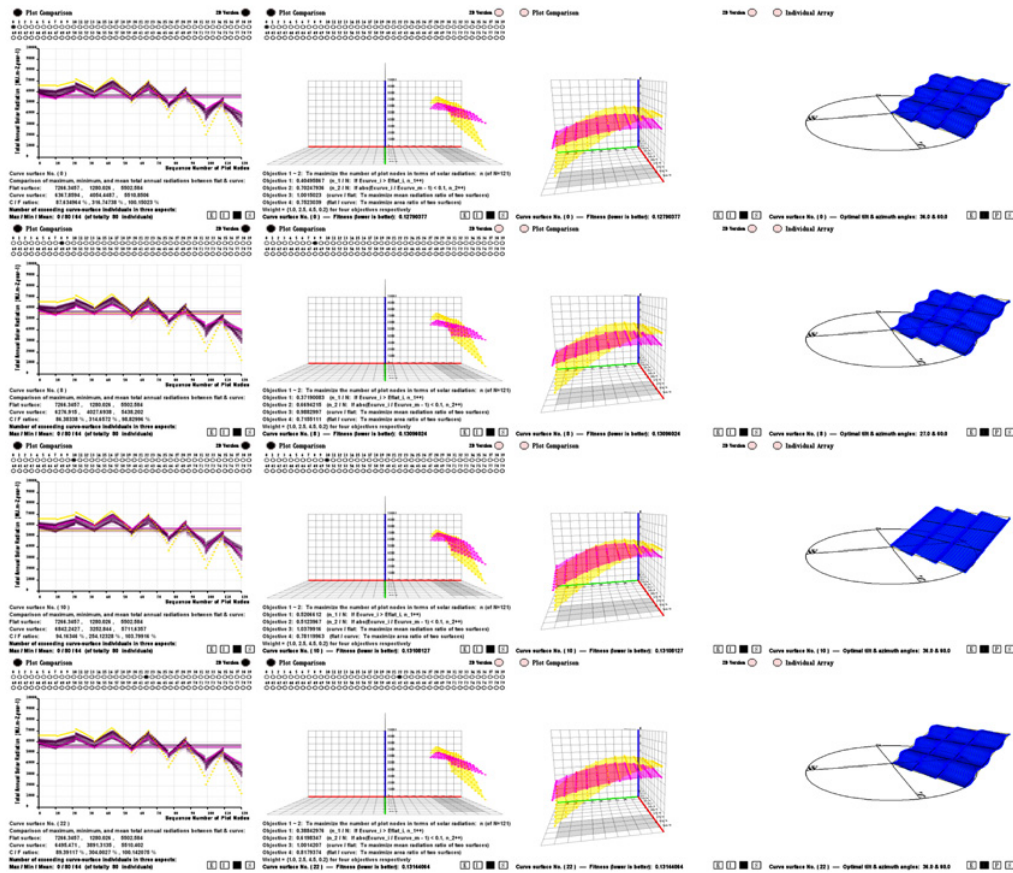


Figure III.3.10 Hy-3 – Phase 3 (Generation No.100; Individual No. from top to bottom: 0; 8; 10; 22)

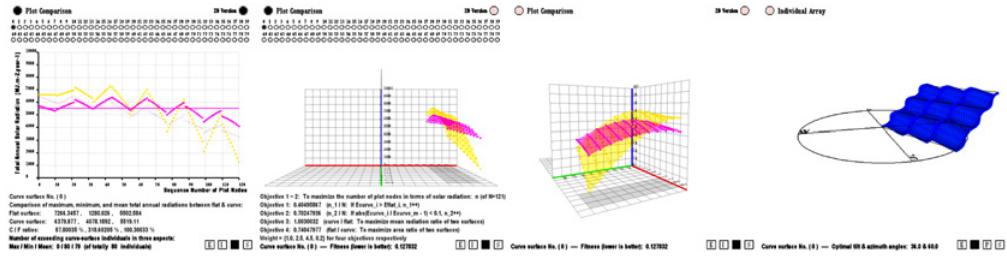


Figure III.3.11 Hy-3 – Phase 4 (Generation No.801; Individual No. 0 – final optimal curved surface)

III.4 Angle-settings of H4 (L= 51.3°N)

Angle-setting of H4-1: $\beta = 0^\circ \sim 45^\circ$, $\gamma = 0^\circ \sim 45^\circ$

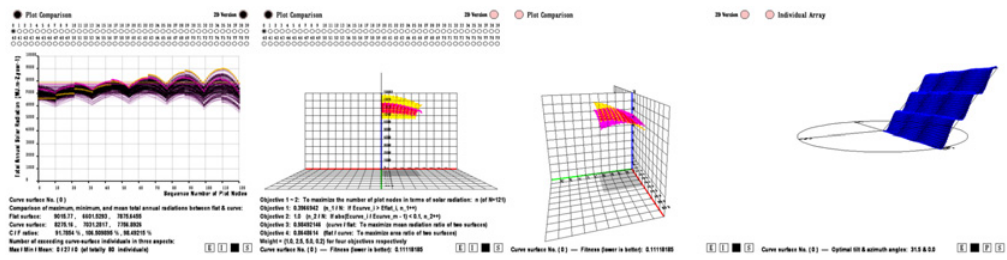


Figure III.4.1 H4-1 – Phase 1 (Generation No. 0; Individual No. 0)

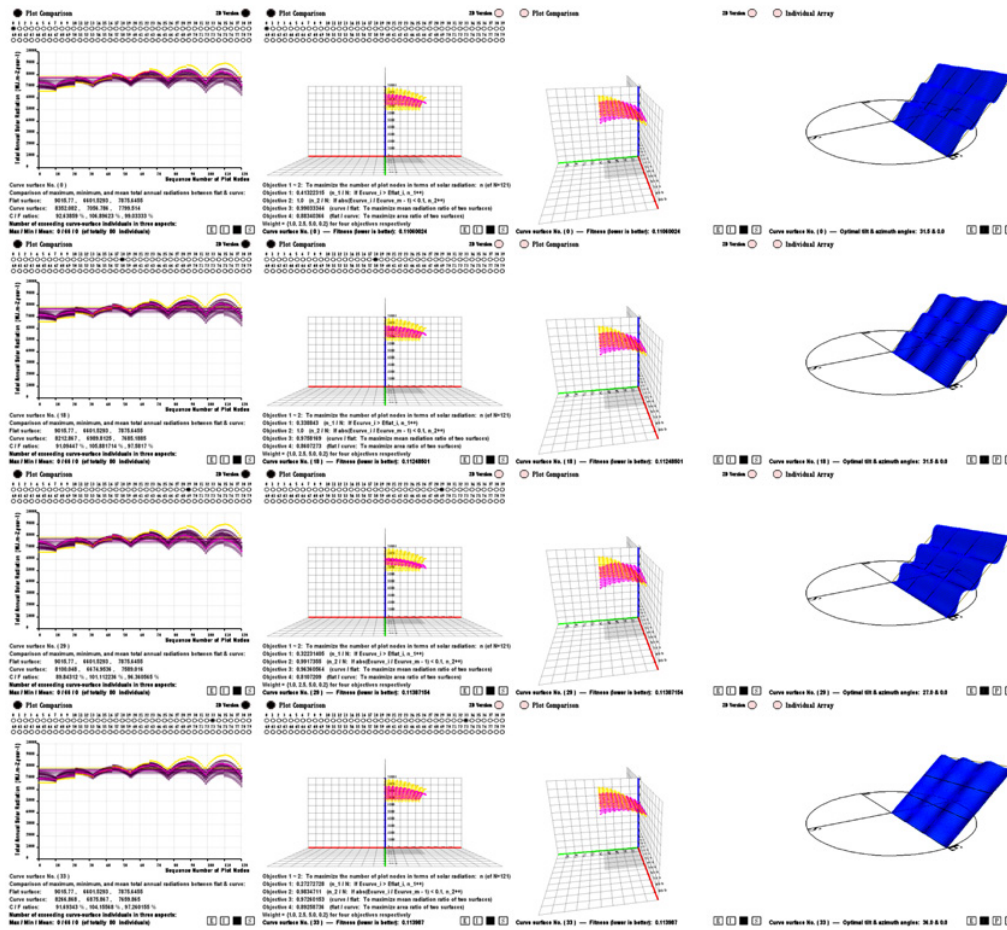


Figure III.4.2 H4-1 – Phase 2 (Generation No.100; Individual No. from top to bottom: 0; 18; 29; 33)

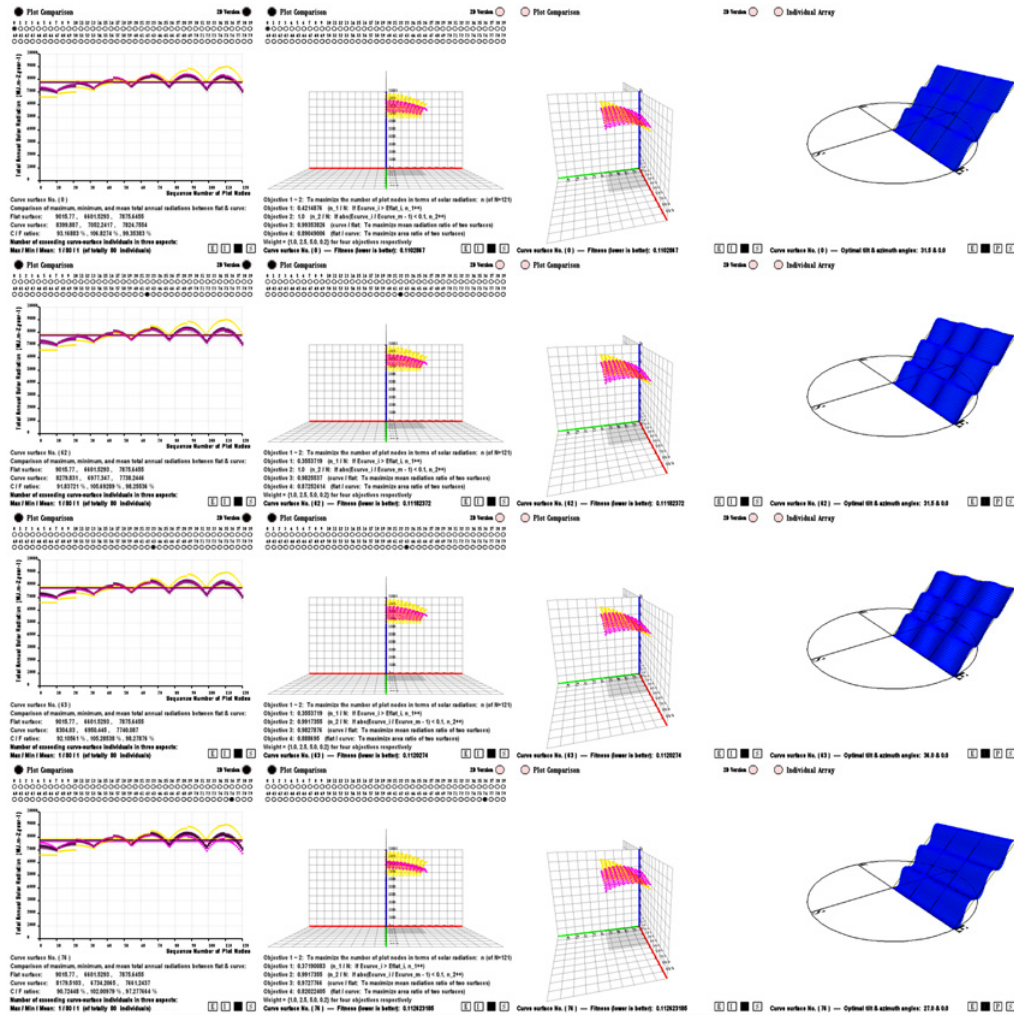


Figure III.4.3 H4-1 – Phase 3 (Generation No.200; Individual No. from top to bottom: 0; 62; 63; 76)

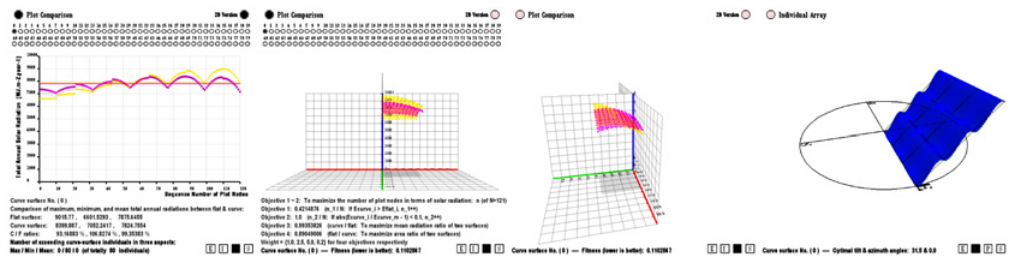


Figure III.4.4 H4-1 – Phase 4 (Generation No.328; Individual No. 0 – final optimal curved surface)

Angle-setting of H4-2: $\beta = 0^\circ \sim 45^\circ$, $\gamma = 45^\circ \sim 90^\circ$

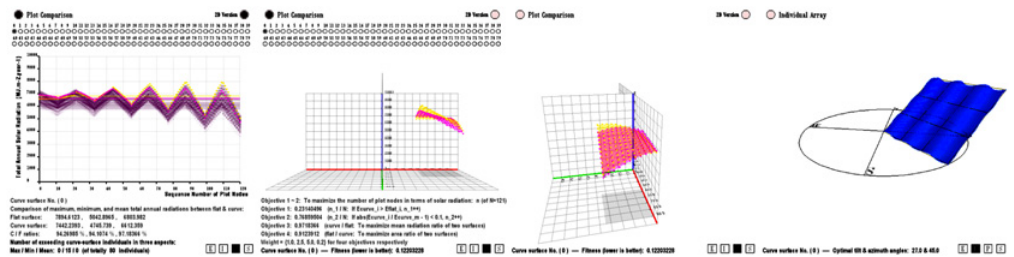


Figure III.4.5 H4-2 – Phase 1 (Generation No. 0; Individual No. 0)

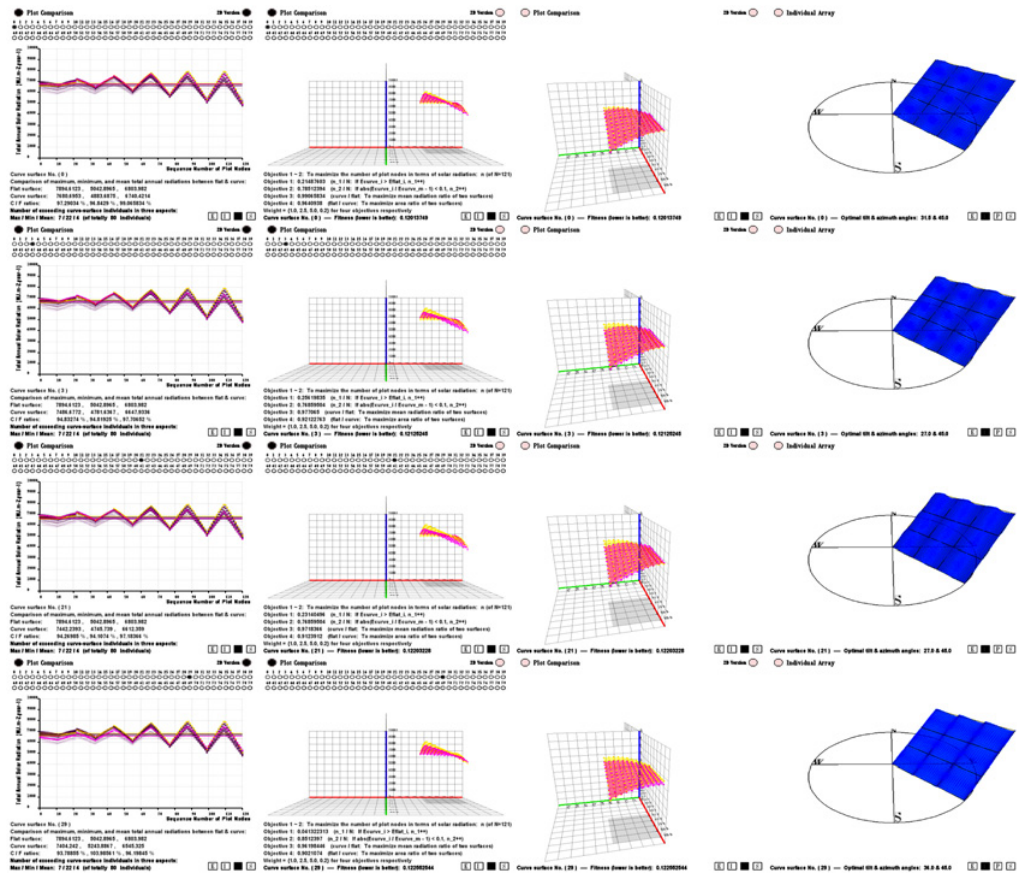


Figure III.4.6 H4-2 – Phase 2 (Generation No.100; Individual No. from top to bottom: 0; 3; 21; 29)

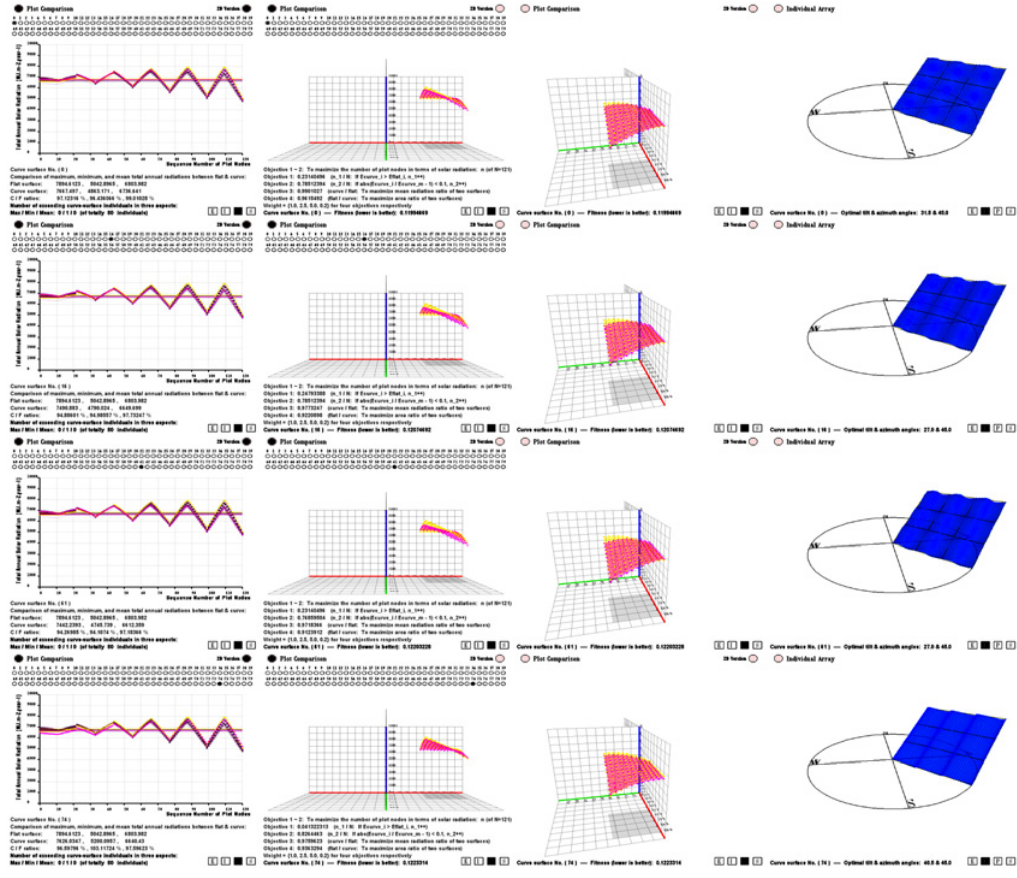


Figure III.4.7 H4-2 – Phase 3 (Generation No.205; Individual No. from top to bottom: 0; 16; 61; 74)

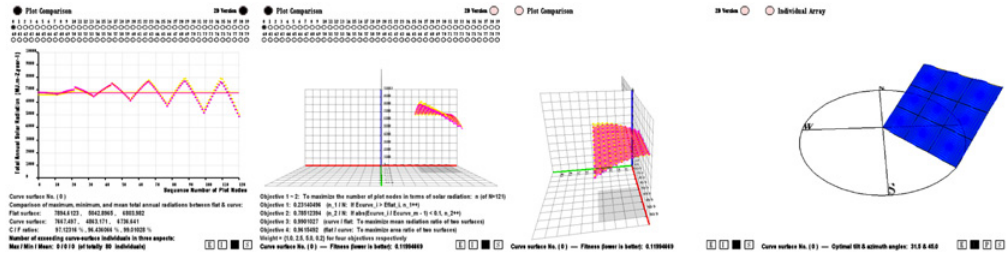


Figure III.4.8 H4-2 – Phase 4 (Generation No.358; Individual No. 0 – final optimal curved surface)

Angle-setting of H4-3: $\beta = 45^\circ \sim 90^\circ$, $\gamma = 0^\circ \sim 45^\circ$

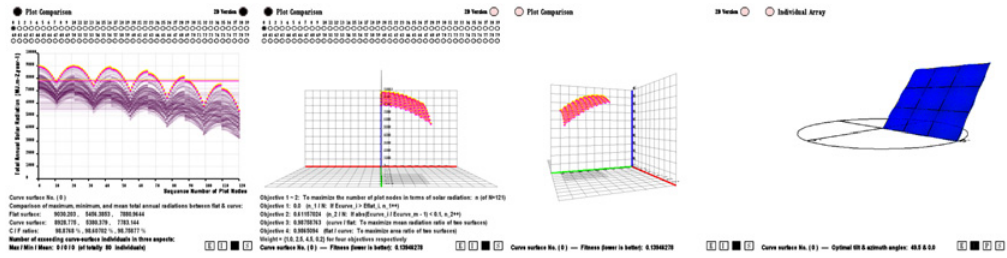


Figure III.4.9 H4-3 – Phase 1 (Generation No. 0; Individual No. 0)

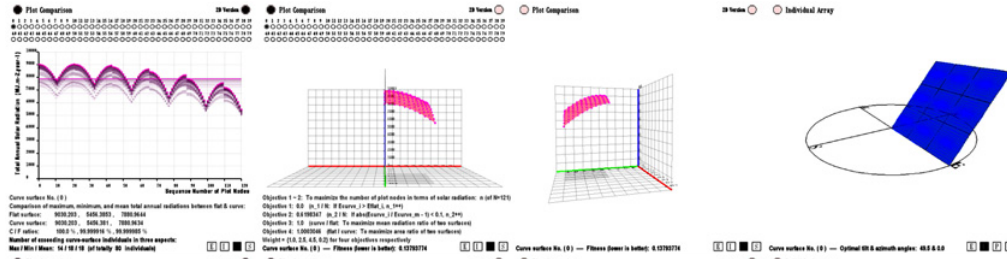


Figure III.4.10 H4-3 – Phase 2 (Generation No.100; Individual No. from top to bottom: 0; 36; 51; 61)

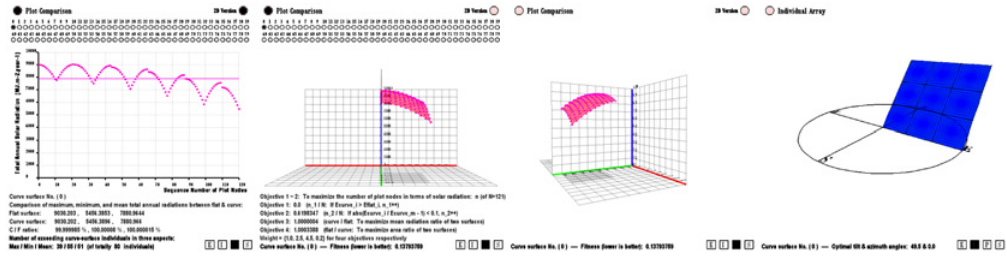


Figure III.4.11 H4-3 – Phase 3 (Generation No.208; Individual No. 0 – final optimal curved surface)

Angle-setting of H4-4: $\beta = 45^\circ \sim 90^\circ$, $\gamma = 45^\circ \sim 90^\circ$

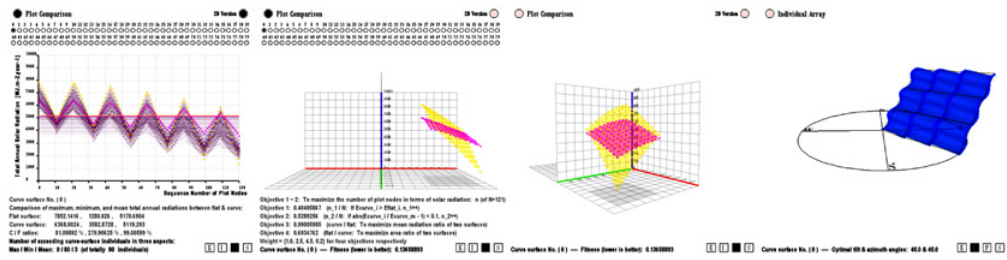


Figure III.4.12 H4-4 – Phase 1 (Generation No. 0; Individual No. 0)

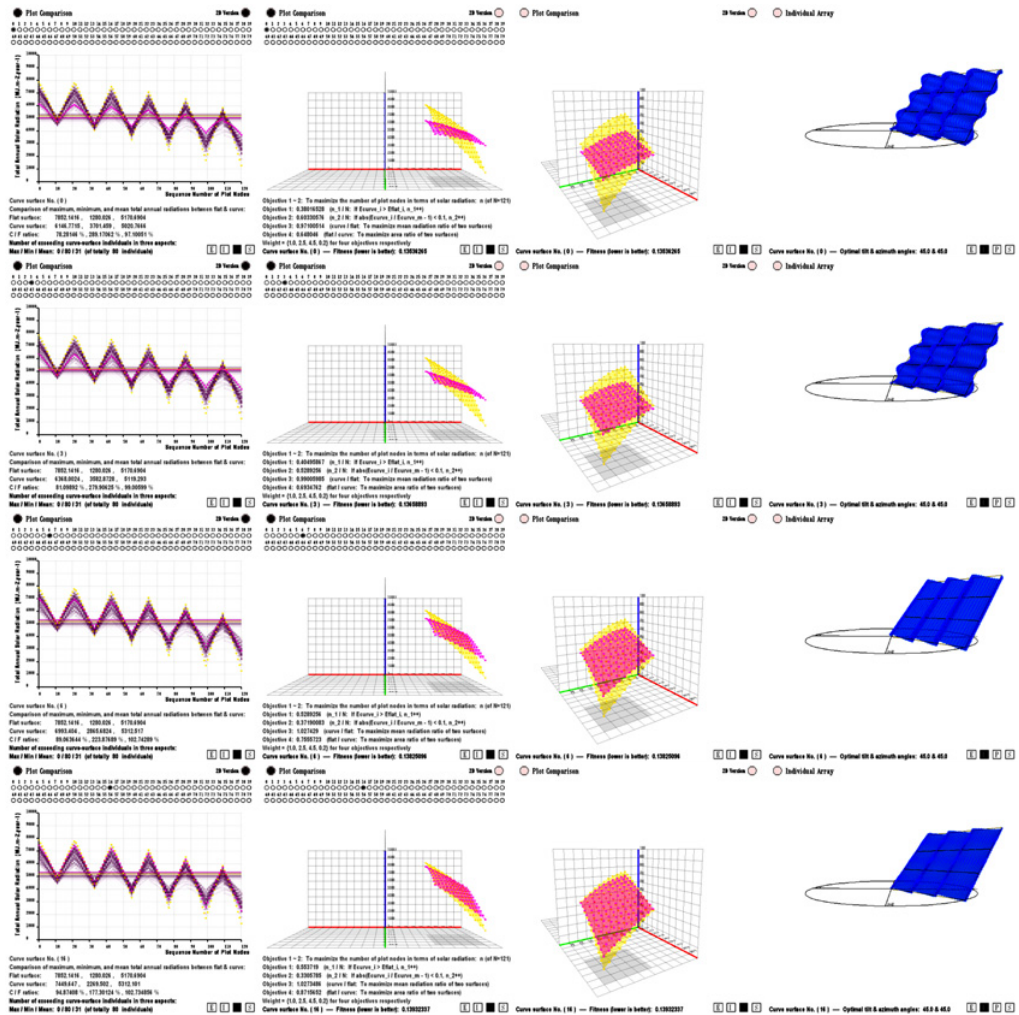


Figure III.4.13 H4-4 – Phase 2 (Generation No.100; Individual No. from top to bottom: 0; 3; 6; 16)

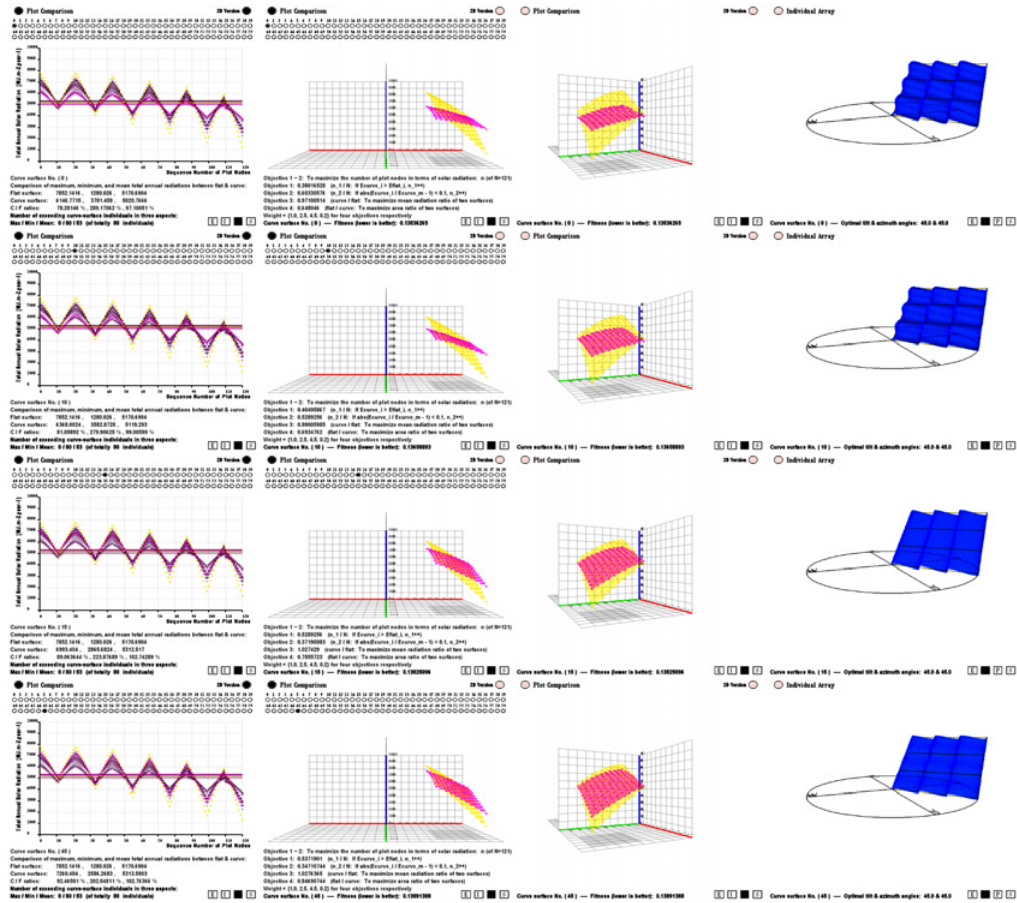


Figure III.4.14 H4-4 – Phase 3 (Generation No.200; Individual No. from top to bottom: 0; 10; 15; 45)

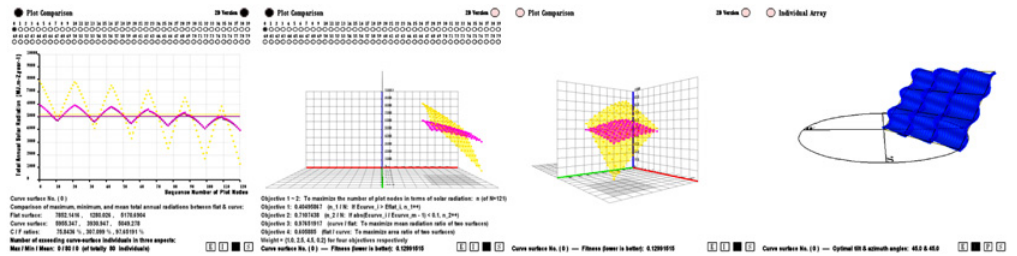


Figure III.4.15 H4-4 – Phase 4 (Generation No.801; Individual No. 0 – final optimal curved surface)

III.5 Angle-settings of H9 (L= 51.3°N)

Angle-setting of **H9-1**: $\beta = 0^\circ \sim 30^\circ$, $\gamma = 0^\circ \sim 30^\circ$ (refer to Appendix II.4 Latitude 51.3°N)

Angle-setting of **H9-2**: $\beta = 0^\circ \sim 30^\circ$, $\gamma = 30^\circ \sim 60^\circ$

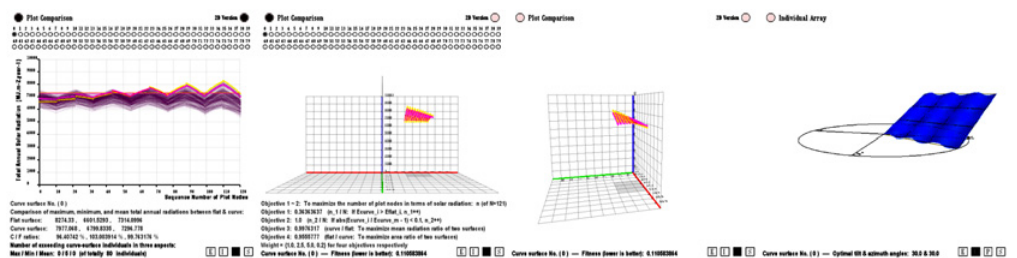


Figure III.5.1 H9-2 – Phase 1 (Generation No. 0; Individual No. 0)

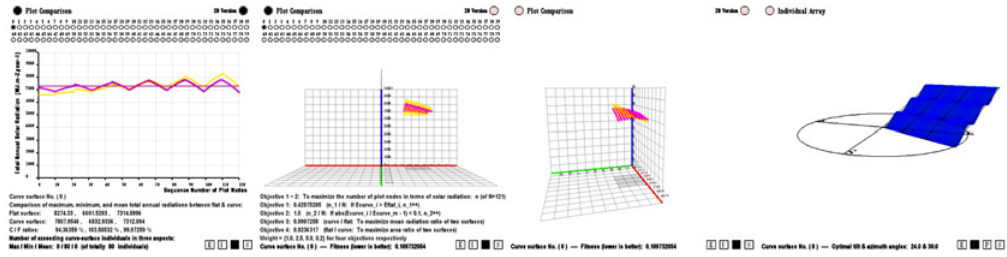


Figure III.5.4 H9-2 – Phase 4 (Generation No.346; Individual No. 0 – final optimal curved surface)

Angle-setting of H9-3: $\beta = 0^\circ \sim 30^\circ$, $\gamma = 60^\circ \sim 90^\circ$

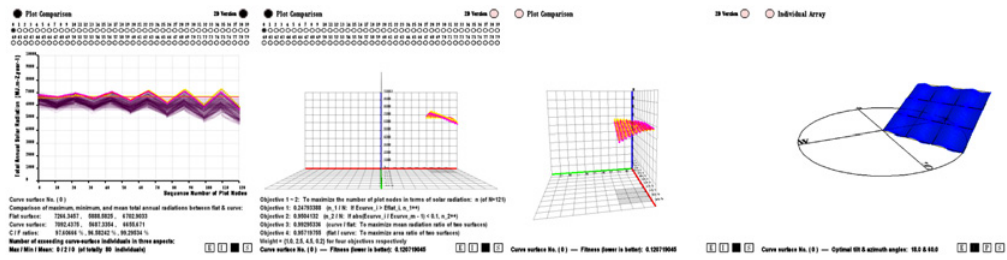


Figure III.5.5 H9-3 – Phase 1 (Generation No. 0; Individual No. 0)

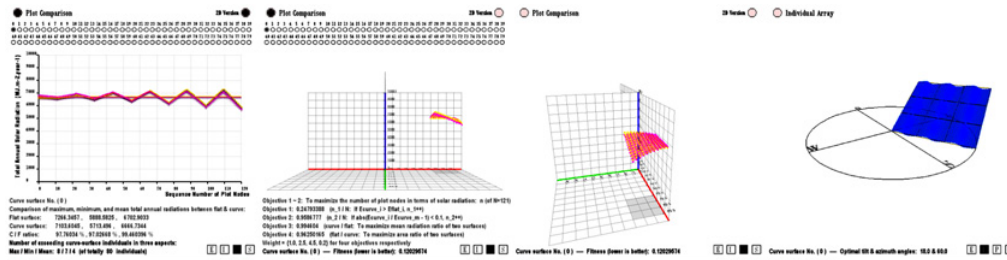


Figure III.5.6 H9-3 – Phase 2 (Generation No.101; Individual No. from top to bottom: 0; 8; 33; 68)

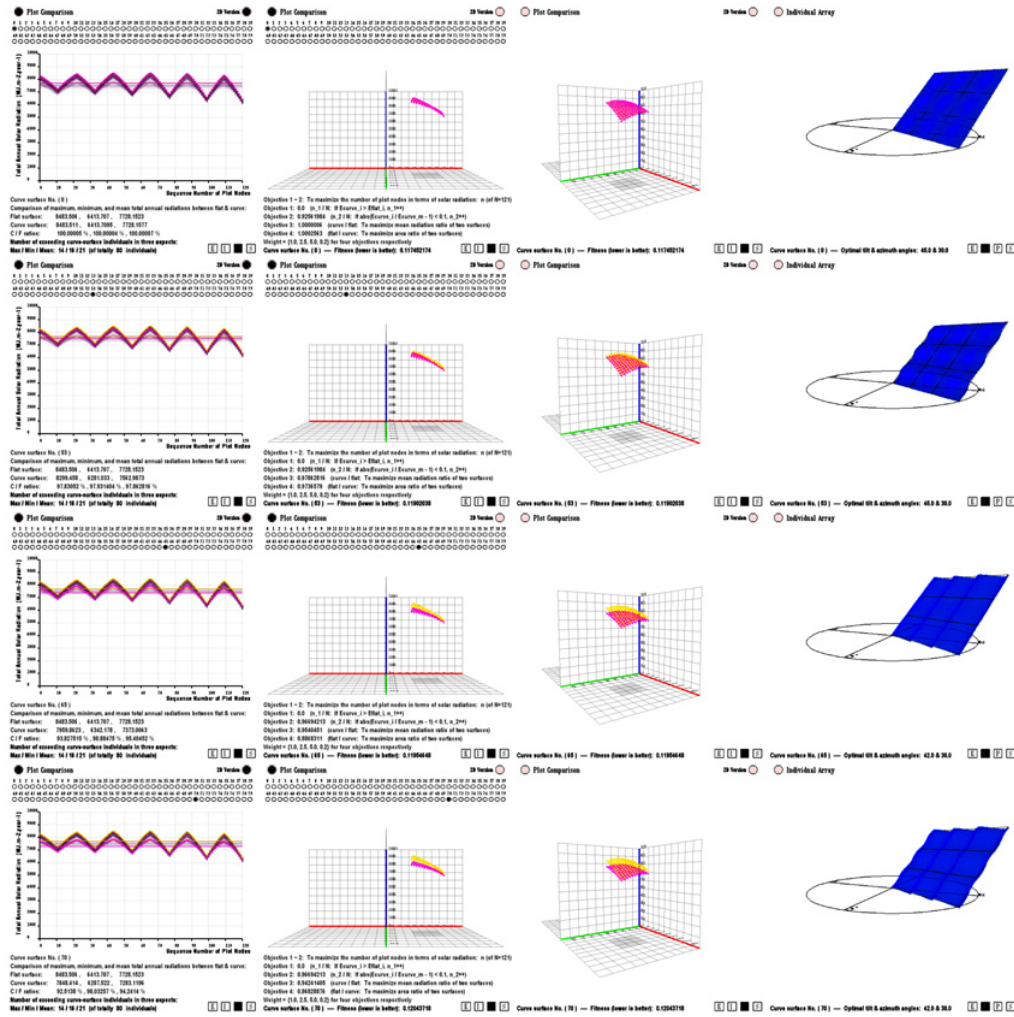


Figure III.5.13 H9-5 – Phase 2 (Generation No.100; Individual No. from top to bottom: 0; 53; 65; 70)

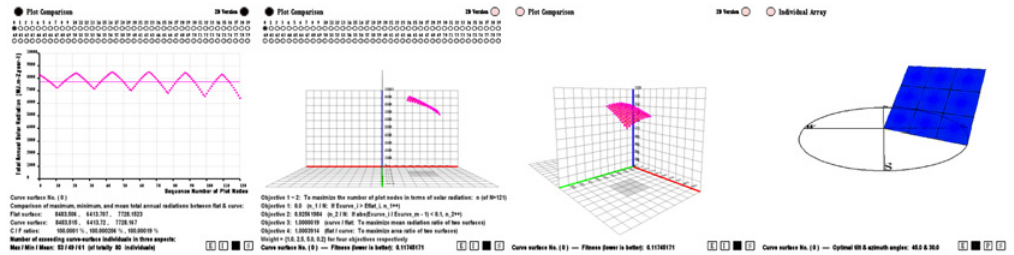


Figure III.5.14 H9-5 – Phase 3 (Generation No.200; Individual No. 0 – final optimal curved surface)

Angle-setting of H9-6: $\beta = 30^\circ \sim 60^\circ$, $\gamma = 60^\circ \sim 90^\circ$

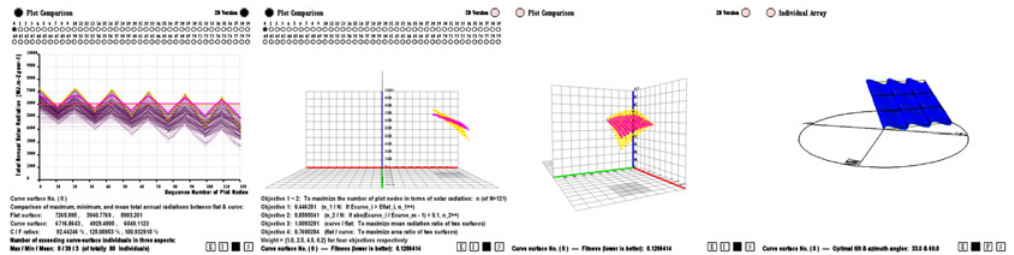


Figure III.5.15 H9-6 – Phase 1 (Generation No. 0; Individual No. 0)

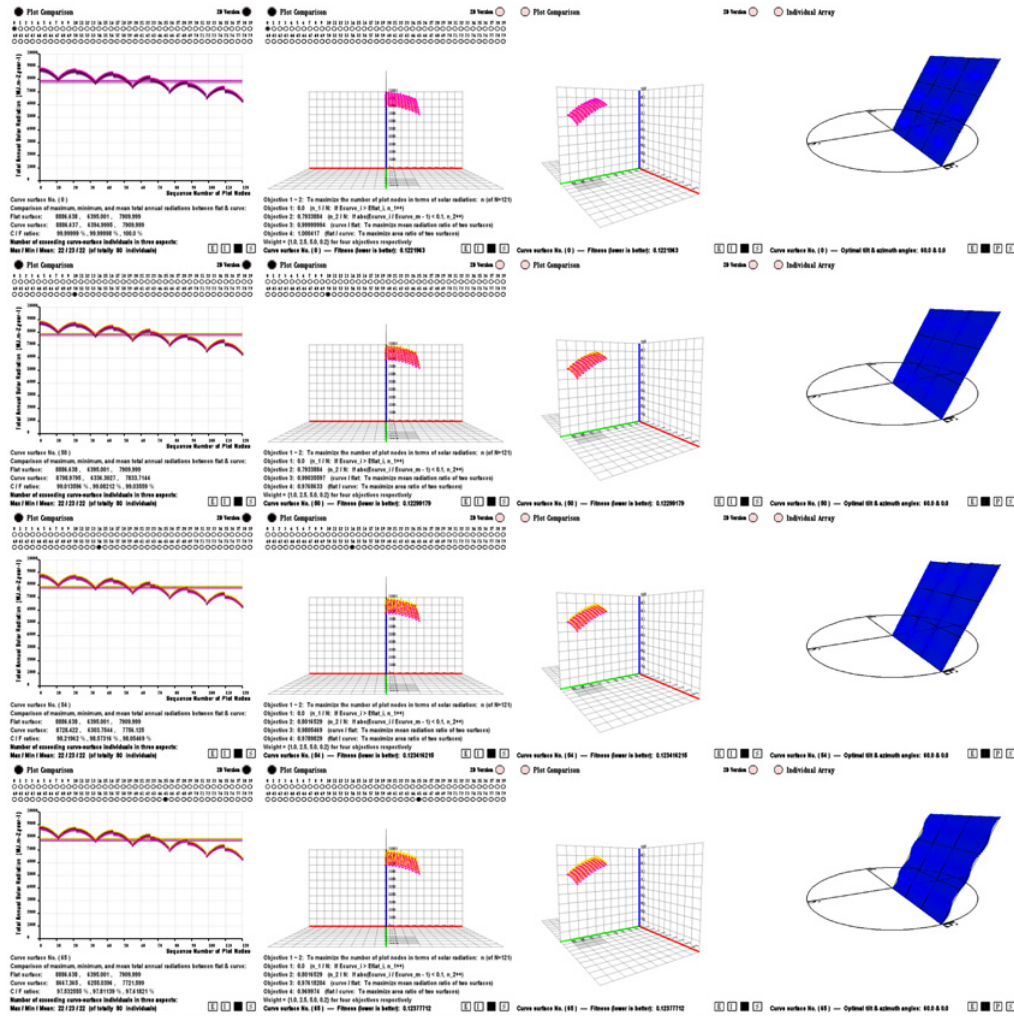


Figure III.5.19 H9-7 – Phase 2 (Generation No.101; Individual No. from top to bottom: 0; 50; 54; 65)

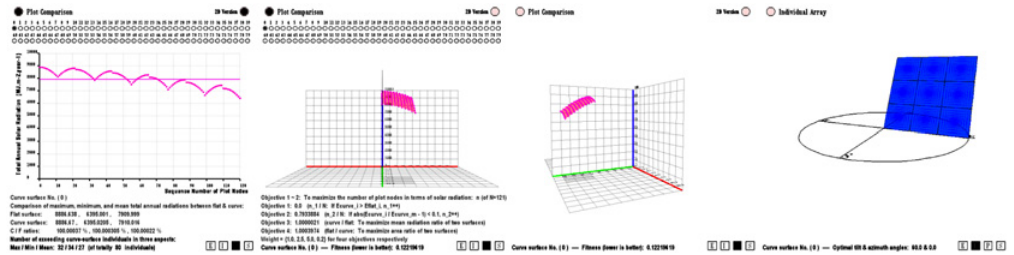


Figure III.5.20 H9-7 – Phase 3 (Generation No.201; Individual No. 0 – final optimal curved surface)

Angle-setting of H9-8: $\beta = 60^\circ \sim 90^\circ$, $\gamma = 30^\circ \sim 60^\circ$

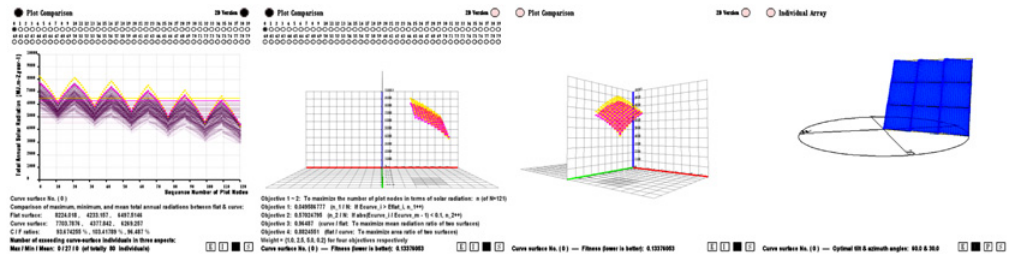


Figure III.5.21 H9-8 – Phase 1 (Generation No. 0; Individual No. 0)

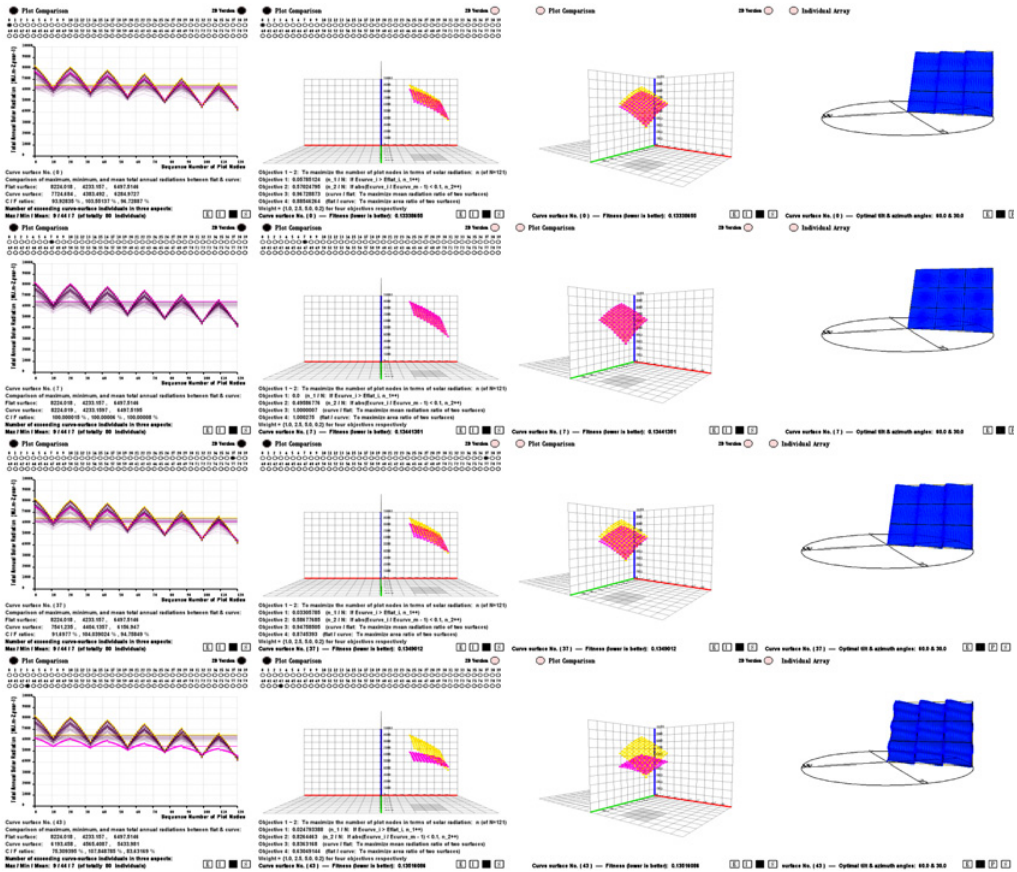


Figure III.5.22 H9-8 – Phase 2 (Generation No.101; Individual No. from top to bottom: 0; 7; 37; 43)

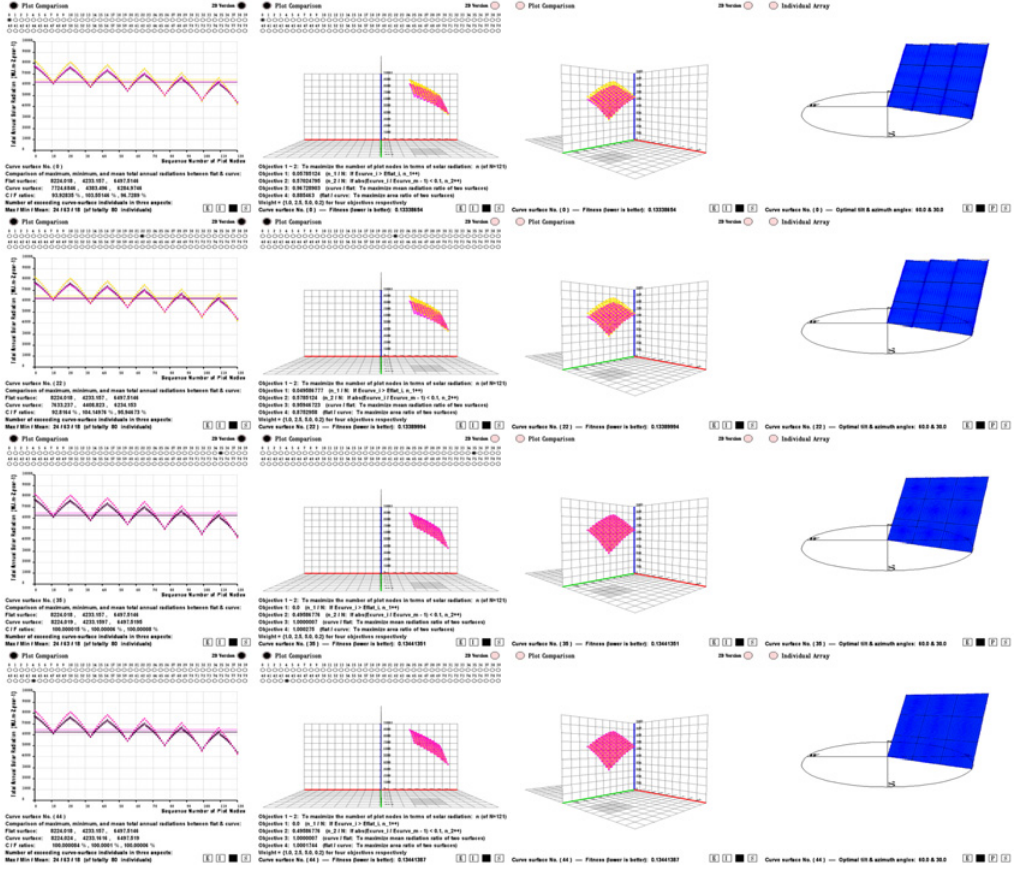


Figure III.5.23 H9-8 – Phase 3 (Generation No.201; Individual No. from top to bottom: 0; 22; 35; 44)

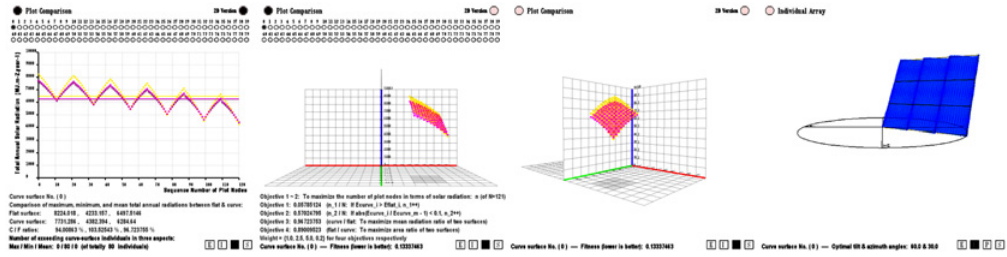


Figure III.5.24 H9-8 – Phase 4 (Generation No.304; Individual No. 0 – final optimal curved surface)

Angle-setting of H9-9: $\beta = 60^\circ \sim 90^\circ$, $\gamma = 60^\circ \sim 90^\circ$

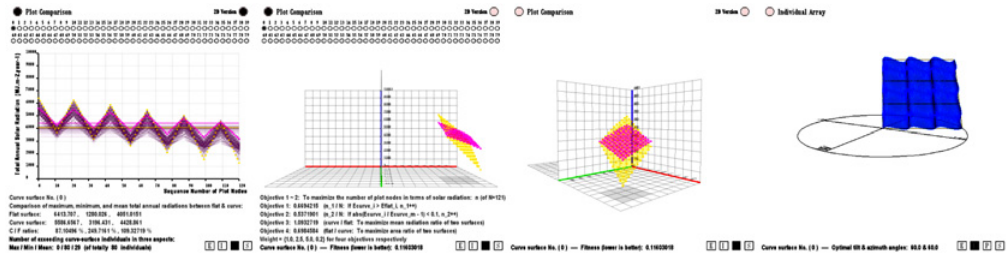


Figure III.5.25 H9-9 – Phase 1 (Generation No. 0; Individual No. 0)

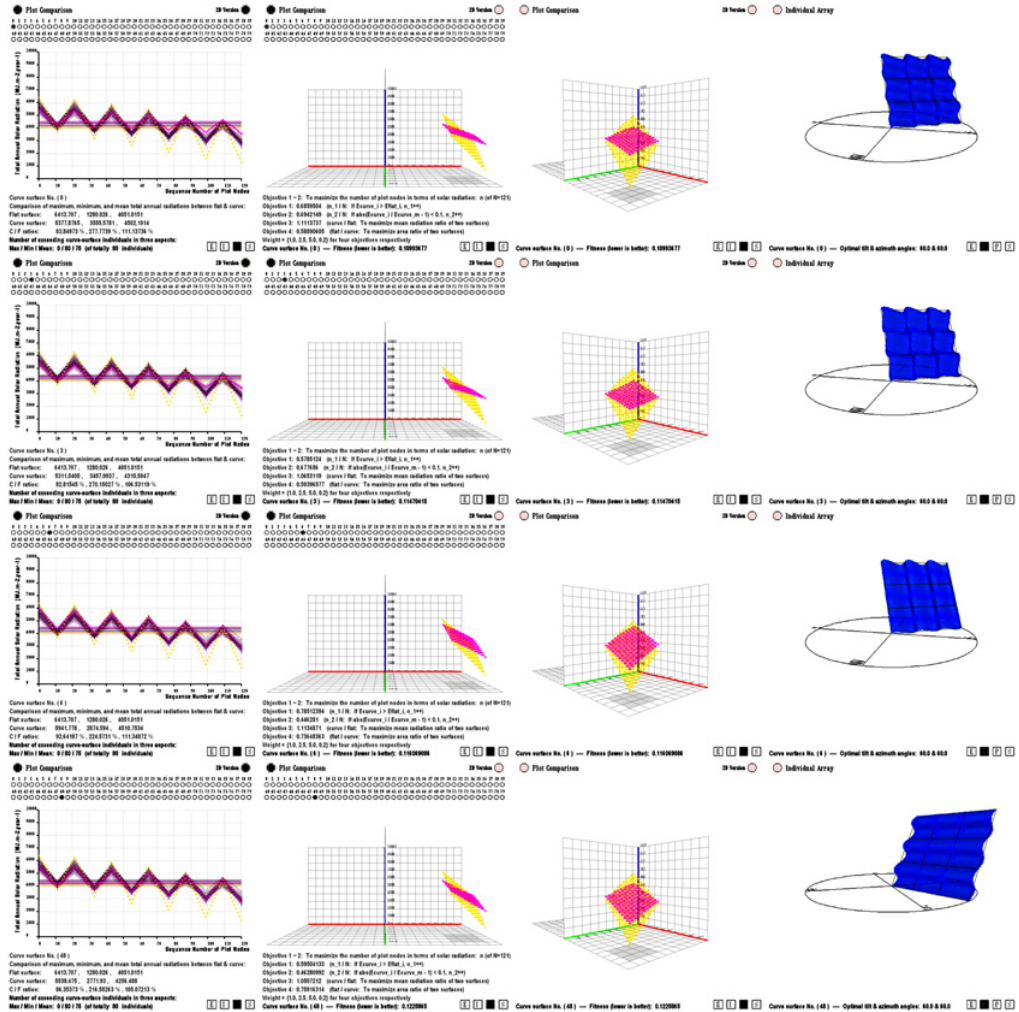


Figure III.5.26 H9-9 – Phase 2 (Generation No.100; Individual No. from top to bottom: 0; 3; 6; 48)

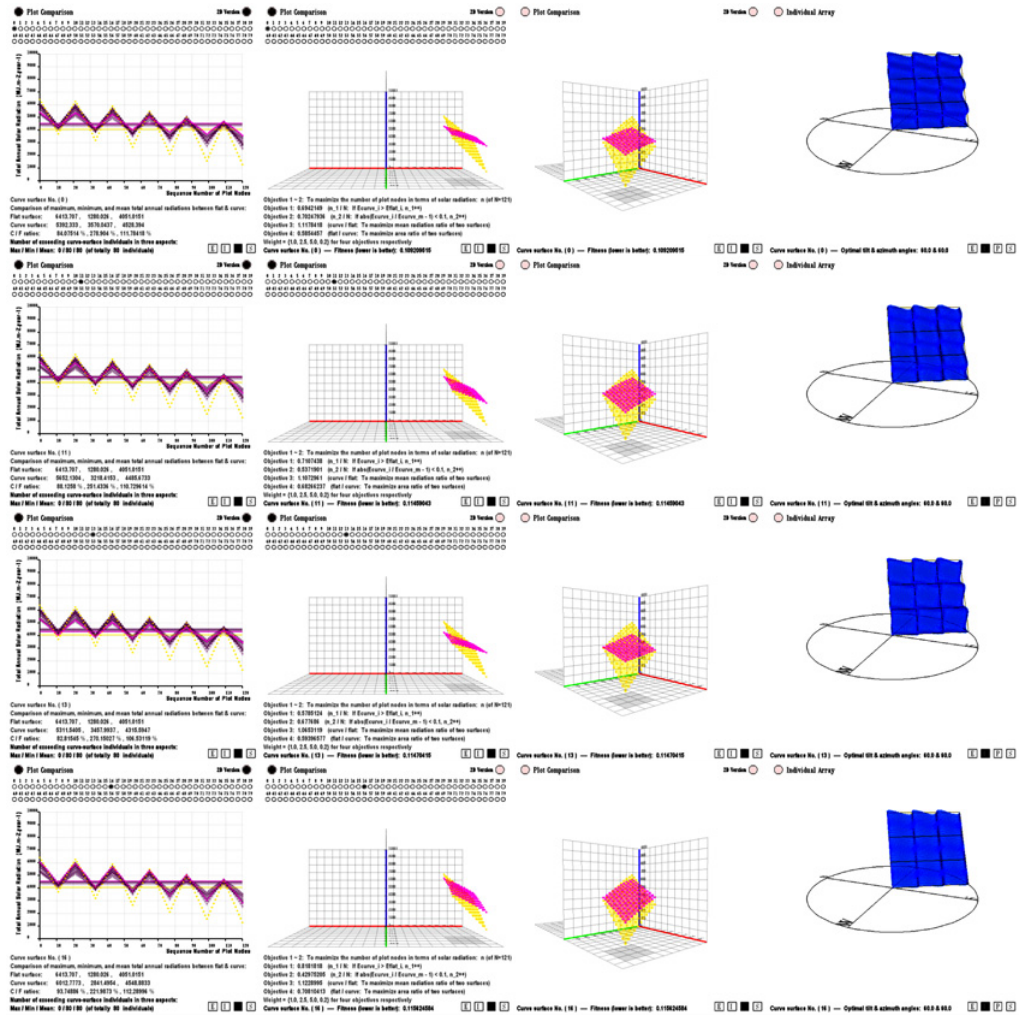


Figure III.5.27 H9-9 – Phase 3 (Generation No.200; Individual No. from top to bottom: 0; 11; 13; 16)

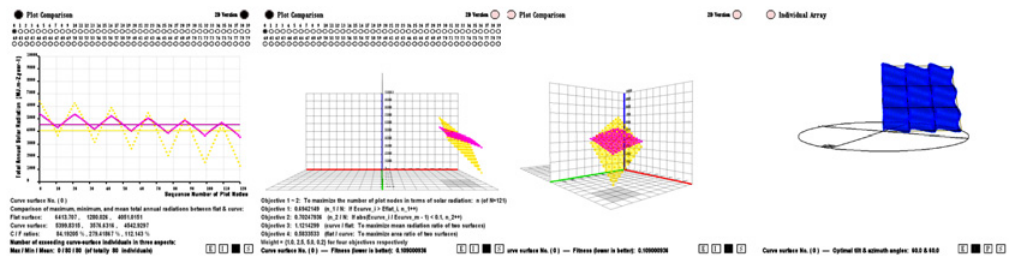


Figure III.5.28 H9-9 – Phase 4 (Generation No.801; Individual No. 0 – final optimal curved surface)

Appendix IV

Code snippet [1] – GA functions

```
// GA Genotype
class Genotype
{
    float u_side = side_u; //size of the PV tile or PV module
    float v_side = side_v;
    float [] m_genes = new float[4];
    int Nctrl = 5;
    float u_range = 1.5 * u_side / (Nctrl-1);
    float v_range = 1.5 * v_side / (Nctrl-1);
    float u_h;
    float v_h;

    Genotype() {}
    Genotype(float uh, float vh)
    {
        u_h = uh;
        v_h = vh;
        m_genes[0] = random(-u_range, u_range);
        m_genes[1] = random(u_h);
        m_genes[2] = random(-v_range, v_range);
        m_genes[3] = random(v_h);
    }

    // GA mutate function
    void mutate()
    {
        if (random(1) < 0.2) m_genes[0] = random(-u_range, u_range);
        if (random(1) < 0.2) m_genes[1] = random(u_h);
        if (random(1) < 0.2) m_genes[2] = random(-v_range, v_range);
        if (random(1) < 0.2) m_genes[3] = random(v_h);
    }
}

// GA crossover function
Genotype crossover(Genotype a, Genotype b) //crossover = recombination
{
    Genotype c = new Genotype();
    for (int i = 0; i < 4; i++) {
        if (random(1) < 0.5) c.m_genes[i] = a.m_genes[i];
        else c.m_genes[i] = b.m_genes[i];
    }
    return c;
}
```

```

// GA phenotype
class Phenotype
{
    PVector2 [][] ctrl_pts;
    float [] u_knots = {0.0, 0.001, 0.002, 0.003, 0.004, 0.996, 0.997, 0.998, 0.999, 1.0}; //10 knots
    float [] v_knots = {0.0, 0.001, 0.002, 0.003, 0.004, 0.996, 0.997, 0.998, 0.999, 1.0}; // k = 2N
    ... //definition of variables
    Phenotype(Genotype g)
    {
        N = g.Nctrl;
        u_D = u_knots.length - N - 1; //degree = 4
        v_D = v_knots.length - N - 1;
        ctrl_pts = new PVector2[N][N];
        u_bar = g.u_side/(N-1);
        v_bar = g.v_side/(N-1);
        u_move = g.m_genes[0];
        u_high = g.m_genes[1];
        v_move = g.m_genes[2];
        v_high = g.m_genes[3];
        PMatrix3D mat = new PMatrix3D(); //rotate the slope by Bopt and Ropt, as the starting position
        mat.rotate(radians(-Ropt), 0, 1, 0);
        pushMatrix();
        rotateY(radians(-Ropt));
        mat.rotate(radians(-Bopt), 1, 0, 0); //remember the south is Z+
        popMatrix();
        PVector2 last_node = new PVector2(g.u_side, 0, -g.v_side); //last node at the corner
        last_node.apply(mat);
        // initiate ctrl points
        for (int i=0; i<N; i++) {
            for (int j=0; j<N; j++) {
                float offset = -sin(i*TWO_PI/(N-1)) * u_high; //where to start period shape is all same
                offset += sin(j*TWO_PI/(N-1)) * v_high;
                ctrl_pts[i][j] = new PVector2(i*u_bar, offset, -j*v_bar); // control points have same interval
                if( i == 1) ctrl_pts[i][j].x += u_move;
                if( i == 3) ctrl_pts[i][j].x -= u_move;
                if( j == 1) ctrl_pts[i][j].z -= v_move;
                if( j == 3) ctrl_pts[i][j].z += v_move;
                ctrl_pts[i][j].apply(mat);
            }
        }
        // PV surfaces 2D and 1D for the use of calculation and display respectively
        PV_surface2d = new PVector[0][0];
        for (float u = u_knots[u_D]; u <= u_knots[u_knots.length-1-u_D]; u += 0.0496) {
            PVector [] temp_u = new PVector[0];
            for (float v = v_knots[v_D]; v <= v_knots[v_knots.length-1-v_D]; v += 0.0496) {
                PVector temp_node = PV_node(u, v, ctrl_pts);
                temp_u = (PVector[])append(temp_u, temp_node);
            }
        }
    }
}

```

```

}
// take into account the last row of v nodes, by using the FIRST row of v nodes of ctr_pts2
PVector [] last_u = new PVector[0];
for (float v = v_knots[v_D]; v <= v_knots[v_knots.length-1-v_D]; v += 0.0496) {
    PVector temp_node = PV_node(u_knots[u_D], v, ctrl_pts2);
    last_u = (PVector[])append(last_u, temp_node);
}
last_u = (PVector[])append(last_u, last_node);
PV_surface2d = (PVector[][])append(PV_surface2d, last_u); //add the last row
// convert to 1d surface
PV_surface1d = new Surface(PV_surface2d);
m_plots = combine_plots(PV_surface1d, Bopt, Ropt); //important
m_plots2d = new PVector[base_plots.length][base_plots[0].length];
for (int i = 0; i < m_plots.length; i++) {
    for (int j = 0; j < m_plots[0].length; j++) {
        m_plots2d[i][j] = new PVector();
        m_plots2d[i][j].x = base_plots[i][j].x;
        m_plots2d[i][j].y = m_plots[i][j];
        m_plots2d[i][j].z = base_plots[i][j].z;
    }
}
}

//GA evaluate function
float [] evaluate()
{
    float [] f_datas = new float[5]; //data set of fitness
    float fitness = 0.0;
    //Objective 1 ~ 2: By maximize the number of nodes in the plot in terms of solar radiation (Energy):
    int good_p = 0; //if E_curve_i > E_flat_i, in order to achieve partial improvements from flat surface
    float ratio_p = 0.0;
    int good_d = 0; //if abs(E_curve_i / E_curve_mean - 1) < 0.1, in order to reduce sensibility to the change
of settings of tilt and azimuth angles
    float ratio_d = 0.0;
    //objective 3: By maximize the ratio of mean total annual radiation of the two surfaces
    float ratio_m = 0.0; // E_curve_mean / E_flat_mean, bigger is better, in order to achieve an average
improvement from flat surface as a whole
    //Objective 4: By maximize the area ratio of the two surfaces
    float ratio_a = 0.0; // A_flat / A_curve, bigger is better, in order to take into account the factor of cost and
complexity of PV manufacture
    float Es = 0.0;
    for (int i = 0; i < m_plots.length; i++) {
        for (int j = 0; j < m_plots[0].length; j++) {
            Es += m_plots[i][j];
        }
    }
    float E_mean = Es / (m_plots.length * m_plots[0].length);
    for (int i = 0; i < m_plots.length; i++) {

```

```

    for (int j = 0; j < m_plots[0].length; j++) {
        float p = m_plots[i][j] / base_plots[i][j].y;
        if (p > 1.01)    good_p++; //1.01 is for safety of processing calculation
        float d = abs(m_plots[i][j] / E_mean - 1);
        if (d < 0.10)    good_d++;
    }
}
int N = m_plots.length * m_plots[0].length;
ratio_p = good_p / (float)N;
ratio_d = good_d / (float)N;
ratio_m = E_mean / Bs[2];
float sumA = 0.0;
for (int i=0; i<PV_surface1d.length-2; i+=3) {
    float p_area = cal_Area(PV_surface1d[i], PV_surface1d[i+1], PV_surface1d[i+2]);
    sumA += p_area;
}
ratio_a = (side_u * side_v) / sumA;
float [] weights = {1.0, 2.5, 5.0, 0.2}; //give different weights to objectives
fitness = 1.0 / (1.0 + ratio_p*weights[0] + ratio_d*weights[1] + ratio_m*weights[2] + ratio_a * weights[3]);
//lower fitness is better
println("Objectives : " + good_p + "/121 , " + good_d + "/121 , " + ratio_m + " , " + ratio_a);
println("Fitness : " + fitness);
f_datas[0] = fitness;
f_datas[1] = ratio_p;
f_datas[2] = ratio_d;
f_datas[3] = ratio_m;
f_datas[4] = ratio_a;
return f_datas;
}

// display function
void draw()
{
    pushMatrix();
    noFill();
    stroke(15, 100, 100-bgColor/2);
    rotateX(radians(-90.0));
    rotateZ(radians(-Ropt));
    rotateX(radians(-Bopt));
    rect(0, 0, u_bar*(N-1), v_bar*(N-1));
    popMatrix();
    if (!fabricatePV) {
        draw_ctrl();
    }
    draw_PV(PV_surface1d);
    draw_node();
}
void draw_PV(PVector [] PVs)

```

```

{
  noStroke();
  fill(60, 100, 100, 70); //thin film
  for (int i=0; i<PVs.length-2; i+=3) {
    beginShape(TRIANGLES);
    vertex(PVs[i].x, PVs[i].y, PVs[i].z);
    vertex(PVs[i+1].x, PVs[i+1].y, PVs[i+1].z);
    vertex(PVs[i+2].x, PVs[i+2].y, PVs[i+2].z);
    endShape();
  }
}

void draw_ctrl()
  ... ..
void draw_node()
  ... ..

PVector PV_node(float u, float v, PVector2 [][] c_pts)
{
  PVector pt = new PVector();
  for (int i=0; i<c_pts.length; i++) {
    for (int j=0; j<c_pts[i].length; j++) {
      PVector pt_k = new PVector(c_pts[i][j].x, c_pts[i][j].y, c_pts[i][j].z);
      pt_k.mult(basis(u, i, u_D, u_knots) * basis(v, j, v_D, v_knots));
      pt.add(pt_k);
    }
  }
  return pt;
}

// curve functions
float basis(float u, int k, int d, float [] knots) // d is the depth
{
  if (d == 0) {
    return basis0(u, k, knots);
  }
  float b1 = basis(u, k, d-1, knots) * (u - knots[k]) / (knots[k+d] - knots[k]);
  float b2 = basis(u, k+1, d-1, knots) * (knots[k+d+1] - u) / (knots[k+d+1] - knots[k+1]);
  return b1 + b2;
}
float basis0(float u, int k, float [] knots)
{
  if (u >= knots[k] && u < knots[k+1]) return 1;
  else return 0;
}
}

```

Code snippet [2] – solar radiation functions

```
// this solar radiation model is based on Hay's anisotropic model (1979)

// calculation total solar radiation annually based on tilt, azimuth angle of slope and latitude angle, degrees
float radiation_annually(float angle_s, float angle_b, float angle_f)
{
    float Kyear = 0.0;
    for (int mon=0; mon<12; mon++)
    {
        float Kmon = meanRadiation_monthly(mon, angle_s, angle_b, angle_f) * 30.417;
        Kyear += Kmon;
    }
    return Kyear;
}

// calculation mean solar radiation monthly based on tilt, azimuth angle of slope and latitude angle, degrees
float meanRadiation_monthly(int mon, float angle_s, float angle_b, float angle_f) //mon is from 0 to 11
{
    float Rangle_s = radians(angle_s); //angle of slope, radians
    float Rangle_b = radians(angle_b); //azimuth of slope, radians, south = 0.0 north = 180.0
    float Rangle_f = radians(angle_f); //latitude, radians
    float [] angle_d = {
        -20.9, -12.9, -2.0, 9.6, 18.7, 23.0, 21.2, 13.8, 2.9, -8.7, -18.4, -23.0
    }; //declination of the sun, degrees, from January to December
    float Rangle_d = radians(angle_d[mon]);
    float a = 0.2; //albedo (reflectivity) of the surface or ground, dimensionless
    float N1; //day length for angle_z <= 85, hr
    float cosN1 = (cos(radians(85)) - sin(Rangle_f)*sin(Rangle_d)) / (cos(Rangle_f)*cos(Rangle_d));
    if (cosN1 > 1) cosN1 = 1.0;
    else if (cosN1 < -1) cosN1 = -1.0;
    N1 = degrees(acos(cosN1)) / 7.5; //formula(2)
    float n; //bright sunshine duration, hr, through observation data
    float [] ns = {
        2.39, 3.66, 4.62, 6.69, 7.85, 7.55, 7.18, 6.77, 5.34, 4.01, 2.3, 1.96
    }; //bright sunshine duration ratio of Petten&De Kooy Observation, 1998-2007 average
    float nN1 = 1.0; // (n/nN1), here ideally, not take into account the effect of cloud, n = N1 for clear-sky mode
    nN1 = ns[mon] / N1;
    float dd = 1.0; //(dm/di) assume circular orbit
    float H; //half day length for a horizontal surface, degrees; radians for first term in (3)
    float cosH = -tan(Rangle_f) * tan(Rangle_d);
    if (cosH > 1) cosH = 1.0;
    else if (cosH < -1) cosH = -1.0;
    H = acos(cosH); //formula(4)
    float K0; //whole day total solar radiation incident on a horizontal surface at the top of the atmosphere for
    half day length H
    K0 = 37.210* sq(dd) * (H*sin(Rangle_f)*sin(Rangle_d) + cos(Rangle_f)*cos(Rangle_d)*sin(H)); //formula(3)
    float K1; //total solar radiation incident on a horizontal surface
```

```

K1 = K0 * (0.1572 + 0.5566*nN1) / (1 - a*(0.25*nN1 + 0.60*(1-nN1))); //formula(5)
float K1b; //total solar radiation incident on a horizontal before multiple reflection
K1b = K1 * (1 - a*(0.25*nN1 + 0.60*(1-nN1))); //formula(1)
float KK = K1b/K0; //KK = 0.1572 + 0.5566*nN1;
if (K0 == 0) KK = 0;
float D1b; //diffuse solar radiation incident on a horizontal surface before multiple reflection
D1b = K1b * (0.9702 + 1.6688*KK - 21.303*pow(KK, 2) + 51.288*pow(KK, 3) - 50.081*pow(KK, 4) +
17.551*pow(KK, 5)); //formula(7)
float D1; //diffuse solar radiation incident on a horizontal surface
D1 = D1b + K1*a*(0.25*nN1 + 0.60*(1-nN1)); //formula(6)

float Hs; //half day length for an inclined south-facing surface,radians
float cosz1; //solar zenith angle z' at the time of sunset for the south-facing slope
cosz1 = sin(Rangle_s) * sin(Rangle_d) / (cos(Rangle_f) * (cos(Rangle_s) + sin(Rangle_s) * sin(Rangle_f) /
cos(Rangle_f))); //formula(11)
float cosHs;
if (cosz1 <= 0) Hs = H; //formula(12)
else
{
if (cosz1 > 1.0) cosz1 = 1.0;
cosHs = (cosz1-sin(Rangle_f)*sin(Rangle_d)) / (cos(Rangle_f)*cos(Rangle_d)); //formula(13)
if (cosHs > 1) cosHs = 1.0;
Hs = acos(cosHs);
}
float Ks; //whole day total solar radiation incident on a horizontal surface at the top of the atmosphere for
half day length Hs
Ks = 37.210* sq(dd) * (Hs*sin(Rangle_f)*sin(Rangle_d) + cos(Rangle_f)*cos(Rangle_d)*sin(Hs));
//formula(3)
float Is; //whole day normal incidence direct radiation at the top of the atmosphere for half day length Hs
Is = 4.87 * degrees(Hs) / 7.5; //formula(15)
float Rangle_Z; //mean solar zenith angle for half day length Hs, radians, for a given month, from 0 to 2PI
if (Hs != 0) Rangle_Z = acos(Ks/Is); //formula(14)
else Rangle_Z = 0.0;

float Rangle_z = Rangle_Z; //replace z with Z
float Rangle_a; //azimuth of sun, radians, from -PI to PI
float cosa = (sin(Rangle_f)*cos(Rangle_z)-sin(Rangle_d)) / (cos(Rangle_f)*sin(Rangle_z));
if (cosa > 1.0) cosa = 1.0;
if (Rangle_Z != 0) Rangle_a = acos( cosa ); //formula(10)
else Rangle_a = PI/2;
float cosi; //cos of angle of incidence of sun's rays on slope, degrees
cosi = cos(Rangle_s)*cos(Rangle_z) + sin(Rangle_s)*sin(Rangle_z)*(cos(Rangle_a - Rangle_b) +
cos(-Rangle_a - Rangle_b))/2.0; //formula(9)
if (cosi < 0) cosi = 0; //when the incidence angle over 90 degrees, no direct radiation
else if (cosi > 1.0) cosi = 1.0;
float S1; //direct solar radiation incident on a horizontal surface (MJ/m2.d)
S1 = K1 - D1; //total - diffuse = direct
float S1s; //direct solar radiation incident on an inclined surface

```

```

float Rb = cosi / cos(Rangle_z); // ratio of incline to horizontal
S1s = S1 * Rb; //formula(8)

float angle_z = degrees(Rangle_z); //solar zenith angle, degrees
float I; //whole day normal incidence direct radiation at the top of the atmosphere
I = 4.87 * degrees(H) / 7.5; //formula(19)
float D1s; //diffuse solar radiation from the sky hemisphere incident on an inclined surface
D1s = D1 * ( S1s/I + 0.5*(1-S1/I)*(1+cos(Rangle_s)) );
if (I == 0) D1s = 0.0;

float R1s; //solar radiation reflected by adjacent surfaces onto an inclined surface
R1s = 0.5 * K1 * a * (1-cos(Rangle_s)); //formula(20)

float K1s; //total solar radiation incident on an inclined surface (MJ/m2.d)
K1s = S1s + D1s + R1s; //formula(21)
return K1s;
}

//output the solar radiation plots based on inputs of angles
PVector [][] solar_plots(float angle_B0, float angle_B1, float angle_R0, float angle_R1, float angle_L)
{
PVector [][] plots;
plots = new PVector[0][0];
float bB = (angle_B1-angle_B0)/10.0;
float rR = (angle_R1-angle_R0)/10.0;
int I = 10;
int J = 10;
if (bB == 0) I = 0;
if (rR == 0) J = 0;
for (int i = 0; i <= I; i++) {
float angle_B = angle_B0 + i*bB;
PVector [] temp_B = new PVector[0];
for (int j = 0; j <= J; j++) {
float angle_R = angle_R0 + j*rR;
float Eyear;
Eyear = radiation_annually(angle_B, angle_R, angle_L);
PVector temp_r = new PVector();
temp_r.x = angle_R;
temp_r.y = Eyear;
temp_r.z = angle_B;
temp_B = (PVector[])append(temp_B, temp_r);
}
plots = (PVector[][]).append(plots, temp_B);
}
return plots;
}

```

Code snippet [3] – supportive functions

```
// calculate the mean energy gains on a curved PV surface in terms of B range and R range
float [][] combine_plots(PVector [] PVs, float baseB, float baseR)
{
    float [][] c_plots = new float[0][0];
    PVector [][][] pieces_plots = new PVector[0][0][0];
    float [] pieces_areas = new float[0];
    for (int i=0; i<PVs.length-2; i+=3) {
        PVector v13 = PVector.sub(PVs[i], PVs[i+2]);
        PVector v23 = PVector.sub(PVs[i+1], PVs[i+2]);
        PVector vN = v23.cross(v13);
        vN.normalize();
        float pieceB = PVector.angleBetween(vN, new PVector(0,-1,0)); //compare with Y+ Axis
        PVector xz = new PVector(vN.x, 0, vN.z);
        float pieceR1 = PVector.angleBetween(xz, new PVector(1,0,0)); //compare with X+ Axis, to check position
        float pieceR = PVector.angleBetween(xz, new PVector(0,0,1)); //compare with Z+ Axis
        if (pieceR1 < PI/2) pieceR = -pieceR;
        float dB = degrees(pieceB) - baseB; //angle difference in B range
        float dR = degrees(pieceR) - baseR; //angle difference in R range
        pieces_plots = (PVector[][][])append(pieces_plots, solar_plots(B0+dB, B1+dB, R0+dR, R1+dR, L));
        float temp_area = cal_Area(PVs[i], PVs[i+1], PVs[i+2]);
        pieces_areas =append(pieces_areas, temp_area);
    }
    float Asum = 0.0; //sum area of the PV surface
    for (int i = 0; i < pieces_areas.length; i++) {
        Asum += pieces_areas[i];
    }
    for (int i = 0; i < pieces_plots[0].length; i++) {
        float [] temp_plots = new float[0];
        for (int j = 0; j < pieces_plots[0][0].length; j++) { //find all pieces in the same B and R angles
            float Esum = 0.0; //sum energy of all pieces at one position of B and R angles
            for (int k = 0; k < pieces_plots.length; k++){
                float Epiece = pieces_plots[k][i][j].y * pieces_areas[k];
                Esum += Epiece;
            }
            float Emean = Esum / Asum; //mean energy of the PV surface
            temp_plots = append(temp_plots, Emean);
        }
        c_plots = (float[][])append(c_plots, temp_plots);
    }
    return c_plots;
}

//function to convert 2D array to 1D array for ease of use later
PVector [] new_Surface(PVector [][] surface)
{
    PVector [] surface2 = new PVector[0];
}
```

```

for (int j=0; j<surface[0].length-1; j++) {
  for (int i=0; i<surface.length; i++) {
    if (i > 0) {
      surface2 = (PVector[])append(surface2, surface[i][j+1]);
      surface2 = (PVector[])append(surface2, surface[i-1][j+1]);
      surface2 = (PVector[])append(surface2, surface[i][j]);
    }
    if (i < surface.length-1) {
      surface2 = (PVector[])append(surface2, surface[i][j]);
      surface2 = (PVector[])append(surface2, surface[i+1][j]);
      surface2 = (PVector[])append(surface2, surface[i][j+1]);
    }
  }
}
return surface2;
}

// display solar radiation plots drawing on the screen
void display_plots(PVector [][] plots_2D)
{
  float xsc = width/100.0;
  float ysc = -height/10000.0;
  float zsc = height/100.0;
  PVector [] plots_1D = new_Surface(plots_2D);
  for (int i=0; i<plots_2D.length; i++) {
    for (int j=0; j<plots_2D[0].length; j++) {
      pushMatrix();
      translate(plots_2D[i][j].x * xsc, plots_2D[i][j].y * ysc, plots_2D[i][j].z * zsc);
      box(5);
      popMatrix();
    }
  }
  noStroke();
  for (int i=0; i<plots_1D.length-2; i+=3) {
    beginShape(TRIANGLES);
    vertex(plots_1D[i].x * xsc, plots_1D[i].y * ysc, plots_1D[i].z * zsc);
    vertex(plots_1D[i+1].x * xsc, plots_1D[i+1].y * ysc, plots_1D[i+1].z * zsc);
    vertex(plots_1D[i+2].x * xsc, plots_1D[i+2].y * ysc, plots_1D[i+2].z * zsc);
    endShape();
  }
  beginShape();
  vertex(plots_2D[0][0].x * xsc, 0, plots_2D[0][0].z * zsc);
  vertex(plots_2D[0][plots_2D[0].length-1].x * xsc, 0, plots_2D[0][plots_2D[0].length-1].z * zsc);
  vertex(plots_2D[plots_2D.length-1][plots_2D[0].length-1].x * xsc, 0,
plots_2D[plots_2D.length-1][plots_2D[0].length-1].z * zsc);
  vertex(plots_2D[plots_2D.length-1][0].x * xsc, 0, plots_2D[plots_2D.length-1][0].z * zsc);
  endShape(CLOSE);
}

```

References

- Athienitis A.K. and Santamouris M.** (2002) *Thermal Analysis and Design of Passive Solar Buildings*. James & James (Science Publishers) Ltd, London, The Cromwell Press.
- Bottger W.O.J. and Schoen A.J.N.** (1995) *Building with Photovoltaics*, (1st ed.). The Hague, Ten Hagen & Stam.
- Chen W. and Shen H. and Liu Y.** (2007) *Performance Evaluation of PV Arrays at Different Tilt Angles and Orientations in BIPV*. ACTA ENERGIAE SOLAR SINICA (2009), Vol.30, No.2.
- Cheng S.** (2009) *Surface Optimization under Solar Energy Simulation*. MSc AAC course paper of BENVGAC3 Computing for Emergent Architecture (2), Unpublished.
- Eiffert P. and Kiss G.J.** (2000) *Building-Integrated Photovoltaic Designs for Commercial and Institutional Structures - A Sourcebook for Architects and Engineers*. U.S. Department of Energy's (DOE's) Office of Power Technologies, Photovoltaics Division (Available electronically at <http://www.doe.gov/bridge>).
- Hanna S. and Mahdavi S.H.** (2003) *An Evolutionary Approach to Microstructure Optimisation of Stereolithographic Models*. Proceedings of CEC2003, The Congress on Evolutionary Computation, Institute of Electrical and Electronics Engineers: 723-730.
- Hay J.E.** (1979) *Calculation of Monthly Mean Solar Radiation for Horizontal and Inclined Surfaces*. Solar Energy (1979), Vol.23: 301-307.
- Kaan H.F. and Reijnga T.** (1998) *PV-integration in Solar Shading: A Retrofit Casestudy (NL)*. THERMIE SE 100/97 NL/DK. < <http://www.bear.nl/content/bearrebuildconf.html>>
- Kaan H.F.** (2009) *Architects Just Want to Develop Attractive Buildings*. ECN, Solar energy + architecture. < <http://www.ecn.nl/nieuws/newsletter/june-2009/solar-energy-architecture/>>
- Li H.W. and Lam N.T.** (2007) *Determining the Optimum Tilt Angle and Orientation for Solar Energy Collection Based on Measured Solar Radiance Data*. International Journal of Photoenergy (2007), Volume 2007, Article ID 85402: 9.
- MA C.C.Y. and IQBAL M.** (1982) *Statistical Comparison of Models for Estimating Solar Radiation on Inclined Surfaces*. Solar Energy (1983), Vol.31: 313-317.
- Messenger R. and Ventre J.** (2000) *Photovoltaic Systems Engineering*. Boca Raton, London, New York, Washington, D.C., CRC Press.
- Naps Systems Oy.** (2001) *Photovoltaics in Buildings - A Brief Introduction*. Printed at Vantaa.
- Nijmeh S. and Mamlook R.** (1999) *Testing of Two Models for Computing Global Solar Radiation on Tilted Surfaces*. Renewable Energy 20 (2000): 75-81.
- Sick F. and Erge T.** (eds) (1996) *Photovoltaics in Buildings - A Design Handbook for Architects and Engineers*. International Energy Agency, Paris, XYZ Publishing Company.
- Yang J.Y. and Mao J.J. and Chen Z.H.** (2001) *Calculation of Solar Radiation on Variously Oriented Tilted Surface and Optimum Tilt Angle*. Journal of Shanghai Jiaotong University (2002), Vol.36, No.7.

Web documents (last accessed: September 2009)

- ArchiExpo, <http://www.archiexpo.com/prod/colt/photovoltaic-glass-solar-shading-52229-127570.html> at

- Axel Meierhoefer (2009) *Are we Leading the Green Economy or do we follow others?*, Eco-Conscious Pioneers, at <<http://www.ecoconsciouspioneers.com/page/2/>>
- BEAR ARCHTECTEN (1998) *Retrofit with Photo-voltaic Shading System ECN - building Petten (NL)*. THERMIE project SE 100/97/NL/DK. <<http://www.bear.nl/>>
- Benjamin Franklin (2007) *Transparent solar cells and modules*, Denis Lenardic, at <<http://www.pvresources.com/en/transparent.php>>
- Buro Happold, at <http://www.burohappold.com/BH/PRJ_BLD_eden_project_phase_iv.aspx>
- Foster + Partners (2009) *BAA reveal Heathrow's new terminal*, World Architecture News, at <http://www.worldarchitecturenews.com/index.php?fuseaction=wanappln.projectview&upload_id=12133>
- Genetic algorithm, at <http://en.wikipedia.org/wiki/Genetic_algorithm>
- gmp von Gerkan, Marg and Partner, at <<http://gmp-architekten.de/index.php?id=4&L=1>>
- Greentech Media (2009) *For Solar Cars, It's All About Curves*, at <<http://www.greentechmedia.com/articles/read/for-solar-car-roof-its-all-about-curves/>>
- ISAAC-DACD-SUPSI BiPV competence centre Via Trevano CH-6952 Canobbio, at <http://www.bipv.ch/materiale_fotovoltaiico_e.asp>
- KYOCERA, Corporation at <<http://global.kyocera.com/>>
- Martin LaMonica (2008) *With transparent HP tech, pretty solar buildings?*, Green Tech, at <http://news.cnet.com/8300-11128_3-54-3.html?keyword=solar+power>
- PNNL (2009) *Top Story - Transforming Roofs from Wasted Space to Energy Source*, Pacific Northwest National Laboratory, at <<http://www.greentechmedia.com/articles/read/for-solar-car-roof-its-all-about-curves/>>
- “Processing” programming language website, at <<http://processing.org>> (Processing was initiated by Ben Fry and Casey Reas)
- PV SUNRISE, at <<http://www.pvsunrise.eu/pv-diffusion-in-the-building-sector-bipv/picture-gallery.html>>
- Sine wave, at <http://en.wikipedia.org/wiki/Sine_wave>
- Solar Building, at <<http://www.max4object.com/wp/?p=810>>
- Solar Glazing Magazine, at <http://www.solarglazingmag.com/?attachment_id=302>
- SUNTECH, at <<http://www.suntech-power.com/productsen/BIPV/BIPVcasestudies/LIGHTTHRU/casestudies/suntech.htm>>
- The A to Z of Building (2009) *Bus Stop Lit By Solar Power*, at <<http://www.azobuild.com/news.asp?newsID=6692>>
- World Radiation Data Center, at <<http://wrdc.mgo.rssi.ru/>>
- Xie Xiao Lin (2008) *BIPV Grid-connected Photovoltaic System of Qingdao Railway Station*, NengYuan.Net, at <<http://solar.nengyuan.net/2008/0723/1706.html>>

CD ROM